Università degli Studi di Padova

Università degli Studi di Padova

Dipartimento di Ingegneria dell'Informazione

Corso di Laurea Magistrale in Bioingegneria

# Methods for estimating metabolic brain connectivity at the region and voxel level using dynamic [$^{18}$F]FDG Positron Emission Tomography


*Relatore:*

Chiar.ma Prof.ssa Alessandra Bertoldo

*Correlatore:*

Dott. Tommaso Volpi

*Laureanda:*

Giulia Vallini

Matricola 1233468



Anno Accademico 2021/2022

**Abstract**

Over the last two decades, brain connectivity has become a dominant concept in neuroscience, and functional magnetic resonance imaging (fMRI) has significantly contributed to the understanding of the functional connectome of the human brain. However, fMRI only indirectly reflects neuronal activity through haemodynamic changes, whereas positron emission tomography (PET) captures relevant biological processes more directly, e.g., glucose metabolism.

*"Regions of the brain whose rCMRglc [cerebral glucose metabolic rates] values are significantly correlated are functionally associated, and the strength of the association is proportional to the magnitude of the correlation coefficient".* This statement from a pioneering study by Horwitz et al. (1984) is the starting point for research on the so-called *metabolic connectivity* (MC), i.e., the set of relationships between the metabolic rates of different regions of the brain.

MC is calculated on PET scans acquired with the glucose analogue [$^{18}$F]fluorodeoxyglucose (FDG). However, instead of exploiting the temporal information of dynamic PET, most studies have used static measures to derive MC at the group level such as the covariation of metabolic information between subjects (*subject-series* approach), usually with the standardized uptake value (SUV). This is in contrast with fMRI, where functional connectivity matrices are derived at the individual subject level from temporal correlations of brain region signals (*time-series* approach).

Therefore, a gold standard method to derive MC networks from dynamic [$^{18}$F]FDG PET data at the single-subject level is missing in literature, and in this context the following thesis project is proposed. First, different approaches capable of retrieving MC matrices using dynamic [$^{18}$F]FDG PET data were tested on a dataset of 71 healthy individuals provided by Washington University in Saint Louis, MO, USA.

After pre-processing of the data (motion correction, coregistration to T1w image, parcellation with the Hammers anatomical atlas, filtering of the noisy initial frames, normalization with 5 different approaches to address the positive trend in the signal), different metrics were tested to calculate *time-series* MC: Euclidean similarity, Pearson cor-

relation, Cosine similarity and Gaussian kernel. These were applied to both the non-normalized and normalized data. The same analyses were then performed on the concentration curve of the free tracer in the tissue and on the concentration curve of the tracer phosphorylated by the hexokinase enzyme, obtained following quantification using an image-derived input function and Sokoloff's two-tissue compartment model. The obtained MC matrices were compared in terms of network structure and between-subject reproducibility.
Subsequently, the time-series matrices were compared with subject-series matrices calculated as across-subject correlation of [$^{18}$F]FDG parameters (i.e., SUVR, $K_i$, $K_1$, $k_3$) to assess the similarities between the results obtained through the proposed method and those derived from the standard across-subject approach.
The next step was to repeat the analyses using functional atlas i.e. the Schaefer parcellation. The ultimate goal is to introduce "time series" metabolic connectivity into connectomics studies, which already incorporate functional connectivity, structural connectivity and effective connectivity, but lack metabolic and receptor information. Therefore, testing MC on functional atlas, frequently employed in connectomics, was a necessary step.
Further studies on the structure of the MC networks via graph theory and enrichment analysis with brain receptor maps were performed to better characterize the physiological underpinnings of the obtained MC networks.
Finally, voxel-level MC analysis was tested using independent component analysis on [$^{18}$F]FDG dynamic data (GIFT toolbox).

The results, using the Hammers parcellation, demonstrated that, by applying Euclidean similarity as a metric, normalisation of the TAC is not a necessary step. Indeed, homotopic interhemispheric connections, already confirmed in a number of brain studies, are evident through the application of this metric.
Furthermore, additional studies reveal that the MC matrices from both the full TAC and last 20 minutes are strongly correlated with those of compartment 2, whereas compartment 1 is weakly correlated with the other portions of the TAC, so the application of compart-

mental modelling cannot be avoided. Another important result is the total absence of correlation between the time-series matrices and the SUVR subject-series matrix, which is generally referred to in the literature when dealing with metabolic connectivity. This result is somewhat analogous to Simpson's paradox, according to which a relationship observed at the level of a population is reversed at the level of the individuals that constitute it. Moreover, the graph metrics of the time-series matrices correlate positively with receptor/protein density information and mean SUVR maps, whereas the metrics of the subject-series correlate negatively or are unrelated to those indices, which cast doubt on their physiological interpretation.

The Schaefer parcellation partly confirmed what emerged with the Hammers case, but the lower correlation values that tend to be obtained are probably related to the very fine parcellation that is introduced in this case (100 or 200 parcels), which leads to an increase in noise in an already very noisy dataset and is therefore not suitable for this PET data.

Finally, the analysis at voxel level did not give satisfactory results, confirming what had already emerged in the study by Ionescu et al. (2021), according to which this approach is not suitable for conventional PET studies given the low signal-to-noise ratio at voxel level.

# Contents

# List of Figures

# List of Tables

# Chapter 1

# Introduction

## 1.1 Positron Emission Thomography

Positron Emission Tomography (PET) is a type of nuclear medicine procedure, involving chemical analysis, that is widely used clinically in oncology, neurology, cardiology and in neuroscience research. PET helps to detect biochemical changes in the body, thus making it possible to identify deviations in the normal metabolism of an organ or tissue and to assess the processes responsible for diseases [1]. As a nuclear medicine technique, it involves the use of a small amount of a radioactive substance, called a radiopharmaceutical, obtained by labelling metabolically active molecules, i.e. substances that are naturally used by the particular organ or tissue during its metabolic process, with positron-emitting radionuclides.

The first studies began in the 1930s, when the first cyclotron was developed for the artificial production of radionuclides. The procedure initially involves the intravenous injection of the radiopharmaceutical into the patient, usually followed (in static acquisitions) by a waiting period to allow a certain concentration of the metabolically active molecule to be reached in the tissue of interest. The patient is then placed in the PET scanner.The isotope, which has a short half-life, decays, resulting in the emission of a positron, which annihilates with an electron. This process gives rise to a pair of gamma photons, both of energy 511 keV, which are emitted in opposite directions and are therefore called back-to-back photons. These photons are detectable when they reach a scintillator, the main component of a PET tomograph, which is the detection system surrounding the table on which the patient is placed. Once the photons hit the scintillator, a bright field

is created that can be detected by the photomultiplier tubes. The idea is to be able to reconstruct from the point at which the photons reach the scintillator, the position in the body from where they are emitted. A computer then uses this information to create an image map of the organ or tissue being studied. The amount of radionuclide collected in the tissue affects the brightness of that area in the image (which usiually can be expressed quantitatively as count/sec or Bq/ml, in absolute units unlike those employed in MRI), thus providing metabolic information.

#### Static and dynamic PET images

PET data are generally stored in a large matrix, in which the value of radioactivity concentration is assigned to each voxel.There are two types of PET images: static and dynamic (figure 1.1). In static, i.e., single-frame acquisition, each voxel contains the sum of the image acquisition period information. This approach, given the extremely reasonable costs and easy management of the patient, is widely used for clinical applications, particularly in oncology and cardiac studies.
On the other hand, with regard to dynamic PET, i.e., multi-frame acquisition, there are a number of reconstructed images and each can be associated to a time frame of different duration (usually frames have increasing duration to match the scanner's count statistics).Thus, the distribution of tracer concentration as a function of time can be measured. This approache sees main application in neuroscience research, particularly to study tissue metabolism and receptor density [2].

### 1.1.1 [$^{18}$F] FDG-PET

Currently, the most widely used radiopharmaceutical is [$^{18}$F]fluoro-D-glucose (FDG), which, being a glucose analogue, is widely utilized as a biomarker of glucose metabolism in the brain. When injected intravenously, it is transported from the blood into the cells mainly by the glucose transporter GLUT1, then phosphorylated by hexokinases (HXKs) to form FDG-6-phosphate and stored in the cells.
This is in fact the main advantage of FDG, as [$^{18}$F]FDG-6-P is trapped in the tissue and released very slowly, so it cannot be metabolised further. By contrast, glucose-6-P is metabolised along the pathways of glycolysis and glycogen synthesis.
However, it should be noted that, as [$^{18}$F]FDG is a glucose analogue, there is

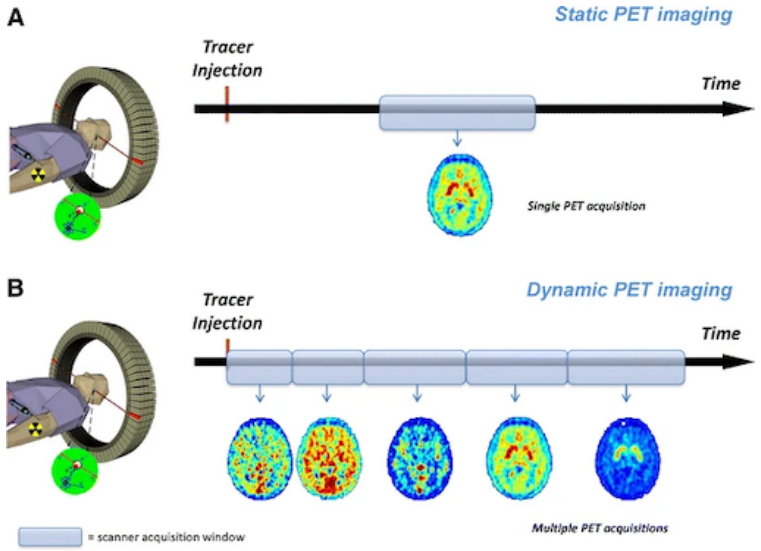


**Figure 1.1:** Static and dynamic PET image. For static scans, tracer activity is measured over a single fixed time period. While in dynamic PET imaging the tracer activity is measured for multiple instants, resulting in 4D matrices [2].

a need to correct for differences in transport and phosphorylation with respect to glucose itself. For this reason a factor, called the *Lumped Constant* (LC), is introduced to convert the fractional uptake of [$^{18}$F]FDG to that of glucose. The LC value depends on several factors, including the type of tissue being tested or the study conditions (insulin level or oxygen availability for example) [3].
Glucose is the primary source of energy in the brain, particularly in the cortex and deep structures of the grey matter. Reductions in glucose metabolism can be seen in a variety of neurodegenerative conditions. Indeed, in studies of patients with Alzheimer's disease and Parkinson's disease, it was noted that changes in regional metabolic ratios occurred compared to healthy subjects [4].
Thus, an understanding of regional metabolic ratios in the brains of healthy individuals is important for understanding the alteration of brain function in disease states. FDG-PET neuroimaging provides a wide range of useful metabolic information, which can elucidate mechanisms of neurological diseases and guide therapeutic approaches. This is the reason why it would be useful to integrate PET connectivity into connectomics studies, which incorporate structural and functional connectivity, but lack metabolic information.

### 1.1.2 Quantification of PET images

PET images can be analysed, depending on the purpose, both qualitatively and quantitatively.

Visual interpretation may be useful in some studies to answer the biological question, for example, when localisation of metabolic defects is the main aim of the study. However, quantitative information is often required and to relate the concentration of the PET tracer with underlying physiological or biochemical processes, a mathematical model must be applied to describe the tracer kinetics in a particular region of interest [2] [3].
Depending on the purpose, different quantification techniques are employed and can be represented by a pyramid structure, as in figure 1.2, in which each level, corresponding to a method, represents the balance between the conditions necessary for its application and the parameters returned as output.

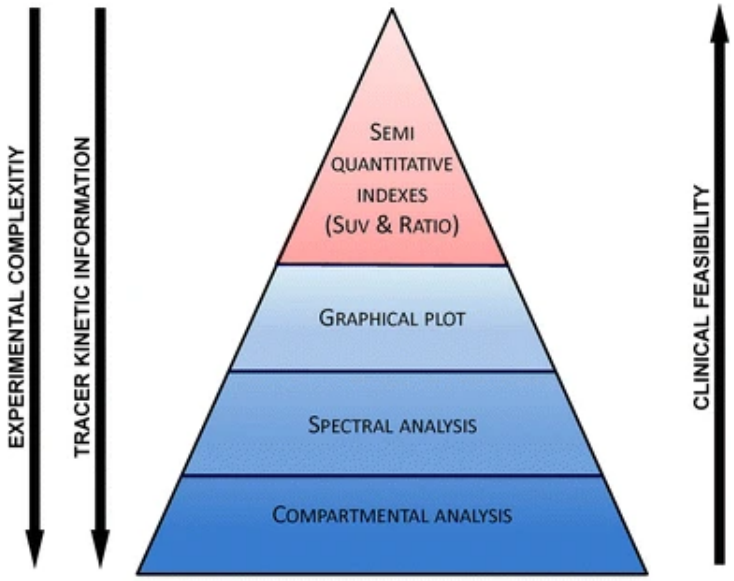


**Figure 1.2:** Hierarchical representation of the different methods used for quantitative or semi-quantitative PET image analysis [2].

All PET quantification methods consist in relating the radioactivity measurements detected by the scanner to the metabolic processes in which the injected tracer is involved, taking into account the specific biological characteristics of the system under investigation. The key assumption assumption is that the tracer does not alter or disrupt the system under study and therefore its functioning in vivo can be deduced directly.
Considering static PET acquisitions first, quantification is based on the semi-quantitative SUV index, the standard uptake value. The study of SUV has been largely developed in clinical practice, as its calculation is very simple and requires only the PET measurement at a fixed sampling time and the injected dose normalised to some anthropometric characteristic of the subject (body weight or

body surface area). As an alternative to SUV, the tissue-to-plasma ratio, i.e. the tracer activity measured in the tissue as a ratio to that in the plasma pool, is often calculated within a fixed time window. The SUV provides an index to quantify the uptake of the tracer in a region of interest or in a voxel and is calculated by:

$$\mathrm{SUV} = \frac{\text{radiotracer concentration}}{\frac{\text{injected dose}}{\mathrm{NF}}} \tag{1.1}$$

where the radiotracer concentration is the concentration measured by PET over a time interval (usually from 5 to 20 minutes), 45-60 minutes after tracer injection. The injected dose, in milliCuries or MBq, is the total dose administered to the patient and NF is a normalisation factor based on anthropometric characteristics of the subject such as body weight, body surface area or lean body mass. Despite the adaptability and simplicity of the SUV, several physiological and technical factors can impact on this calculation and therefore an a priori validation is necessary: given a tracer and a certain system, it is necessary to verify the reproducibility of SUV, its consistency with the physiology and kinetics of the tracer, and its ability to discriminate between healthy and pathological tissues.
Moving on to dynamic acquisitions, which are more informative, there are three classes of models most widely used, which differ in terms of application assumptions (e.g. reversibility of tracer uptake, model structure, etc.) and these are: compartmental models, spectral analysis modelling approach and graphical methods. While spectral analysis and graphical methods are linear modelling techniques, thus usable for the quantification of physiological systems in a steady state, compartmental models can be linear or non-linear, thus allowing a non-stationary description. It follows that they provide a richer physiological explanation than the other two methods, obviously with increased modelling complexity. Thus, while compartmental modelling requires a complete mathematical description of the system's processes, it is absolutely the richest approach, allowing a complete understanding of the physiological process itself or of the pathogenesis of a disease by revealing the mechanisms underlying the system under investigation.
Compartmental models have been widely used since the pioneering contribution of Sokoloff and colleagues in 1977, who introduced the well-known two-tissue compartmental model based on the tracer 2-[$^{14}$C]deoxyglucose to quantify cerebral glucose consumption [5].
In compartmental models, a linear or non-linear structure must first be postulated

in terms of the number of compartments and their interconnections, which must have a reliable biochemical and physiological basis, thus being able to describe aspects such as diffusion, transport, metabolism and receptor-ligand binding. Each compartment, depicted by means of a circle, is understood as a quantity of well-mixed and kinematically homogeneous material, described by a time dependent system of first-order differential equations. From this time dependence comes the necessity to acquire dynamic PET images. The arrows between the compartments, instead, represent a flow of material due to transport or chemical transformation or both.

The two-tissue compartmental model proposed by Sokoloff and colleagues was subsequently used for [$^{18}$F]FDG PET studies in the brain and other tissues or organs. In the model, shown in the figure 1.3, $C_\mathrm{p}$ is the arterial plasma concentration of [$^{18}$F]FDG, $C_1$ the tissue concentration of [$^{18}$F]FDG and $C_2$ the concentration of [$^{18}$F]FDG-6-P in the tissue.

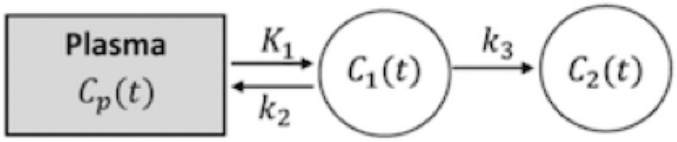


**Figure 1.3:** Two-tissue compartment model for quantifying [$^{18}$F]FDG glucose analogue as proposed by Dr. Sokoloff and colleagues in 1977 [2].

Microparameters $K_1$ and $k_2$ represent the kinetics of forward and reverse [$^{18}$F]FDG transport across the membrane respectively, and $k_3$ the rate constant of [$^{18}$F]FDG phosphorylation. The use of arterial plasma samples and dynamic PET images allows the estimation of model microparameters. Note that $K_1$ in the PET literature is reported with a capital k to indicate a different unit of measurement (ml/ cm$^3$/min or ml$_{\mathrm{plasma}}$/ml$_{\mathrm{tissue}}$/min) than the remaining parameters.

The kinetics of the tracer in the tissue is described by:

$$\begin{cases} \dot{C}_1 = K_1 C_\mathrm{p}(t) - (k_2 + k_3) C_1(t) & \mathrm{C}_1(0)=0 \\ \dot{C}_2 = k_3 C_1(t) & \mathrm{C}_2(0)=0 \end{cases} \tag{1.2}$$

After the injection of [$^{18}$F]FDG into the blood, the total concentration of radioactivity in the tissue, $C_i$, is equal to the sum of the concentrations of [$^{18}$F]FDG and [$^{18}$F]FDG-6-P at any time:

$$C_\mathrm{i}(t) = C_1(t) + C_2(t) \tag{1.3}$$

However, due to the limited spatial resolution of the PET scanner, the measurement of tracer concentration in a ROI (Region Of Interest) also includes the measurement of radioactivity in the volume of blood present within the tissue. It follows that a certain fraction, $V_{\mathrm{b}}$, of the concentration of $^{18}$F in the blood, $C_{\mathrm{b}}$, must be added to the above formula:

$$C_{\mathrm{i}}(t) = (1 - V_{\mathrm{b}})(C_1(t) + C_2(t)) + V_{\mathrm{b}}C_{\mathrm{b}}(t) \tag{1.4}$$

Where $V_{\mathrm{b}}$ in brain and skeletal muscle means the vascular volume present in the ROI tissue, while in the heart it represents the spillover effects from blood to tissue, which are negligible in brain and skeletal muscle.
The quantification of microparameters is usually performed using the weighted non-linear least squares estimator. In this approach, the weights are expressed as the inverse of the variance of the PET measurement error. For the estimation of the variance, several formulas can be used, including the most widely adopted one:

$$var(t_{\mathrm{k}}) = C(t_{\mathrm{k}})/\Delta t_{\mathrm{k}} \tag{1.5}$$

where $C(t_{\mathrm{k}})$ is the mean measured value of the tracer activity over the $k_{\mathrm{th}}$ relative scan time interval $\Delta t_{\mathrm{k}}$. However, if the data are very noisy, as in the case of voxel level, the estimator may have problems with convergence, high calculation time and sensitivity to initial estimates. In this case different estimation approaches have to be adopted.
From the microparameters it is possible to derive the macroparameter of interest, i.e. the fractional uptake of [$^{18}$F]FDG, $K_{\mathrm{i}}$:

$$K_{\mathrm{i}} = \frac{k_1 k_3}{k_2 + k_3} \tag{1.6}$$

When $K_{\mathrm{i}}$ is known, the regional metabolic rate of glucose can be derived:

$$rGl = \frac{k_1 k_3}{k_2 + k_3} \frac{C_{\text{p-g}}}{LC} \tag{1.7}$$

where $C_{\text{p-g}}$ is the arterial plasma glucose concentration and $LC$ is the factor describing the relationship between the glucose analogue and glucose itself. $LC$ is defined as:

$$LC = \frac{E^{\mathrm{FDG}}}{E^{\mathrm{GLU}}} \tag{1.8}$$

where $E^{\mathrm{FDG}}$ and $E^{\mathrm{GLU}}$ are the extraction of [$^{18}$F]FDG and glucose respectively.

### Quantification at voxel level: Variational Bayesian approach

Since pathological states may change micro-parameters it is important to obtain their parametric maps at a voxel level. Furthermore, at the level of regions of interest, there would be a loss in terms of spatial resolution, and averaging the time activity curves of voxels would ignore the variability between them, so voxel-level analyses would also be introduced. However, in this case, the weighted non-linear least-squares estimator would have three problems: lack of convergence due to the low signal-to-noise ratio, inacceptable precision of parameter estimates and non physiological estimates (e.g.., $< 0$ or $> 1$). A suitable alternative is offered by Bayesian methods, which have already been used in the literature and have the advantage of incorporating prior information on tissue kinetics. The critical point is that the computation of the posterior distribution, involving numerical integrations, is, most of the times, intractable. An option is the Variational Bayesian (VB) approach, which approximate the posterior distribution to make it numerically tractable. VB has already been implemented in PET studies for reconstruction [6,7] and segmentation and recently has been adapted for kinetic PET modelling and customised to the characteristics of its noise distribution [8]. In a VB approach, a priori information is used to help in the estimation of the parameter vector $\boldsymbol{\vartheta}$, given a model $y$ ($y = C(\vartheta, t)$) and a set of measurements $z$. The prior distribution are data-driven, using a hierarchical scheme: the estimates obtained from model fitting at ROI level with WNNLS are passed to the voxel level as prior information. The idea is to use the data z to refine the a priori information $P(\vartheta|y)$ and to obtain the posterior distribution of the vector $\boldsymbol{\vartheta}$, that is $P(\vartheta|z, y)$. The link between the posterior and the a priori distribution is express by the Bayes' rule (neglecting the dependence on $y$):

$$P(\vartheta|z) = \frac{P(z|\vartheta)P(\vartheta)}{P(z)} \tag{1.9}$$

Where $P(z|\vartheta)$ is known as likelihood, the probability density function that, given $\vartheta$ and $y$, describes the data $z$.
In VB approach:

$$\hat{\vartheta} = \arg\min_{\vartheta} P(\vartheta|z) \tag{1.10}$$

In practise the numerical integrations involved in the calculus of $P(\vartheta|z)$ make the problem intractable. In real applications, VB methods analytically approximate the posterior with the simpler function $Q(\vartheta)$ [9]. The goal is to reduce

the difference between the real and approximate posterior: this difference can be quantified via the Kullback–Leibler divergence [10]:

$$KL[Q(\vartheta)||P(\vartheta|z)] = \log P(z) - F \tag{1.11}$$

Where $F$ is the free energy term, defined as:

$$F = \int Q(\vartheta) \log \frac{P(z|\vartheta)P(\vartheta)}{Q(\vartheta)} \, d\vartheta \tag{1.12}$$

The logarithmic term in 1.11 does not depend on $\vartheta$ and can be ignored. Assured that $KL$ divergence is non-negative it can be minimized by maximising $F$.
In order to make the integrals tractable, VB specifies a mean field approximation for $Q(\vartheta)$. In practice $\vartheta$ is collected into two separate groups: one with model parameters ($\vartheta$) and another with noise-related parameters ($\varphi$). Each group has its own approximate distribution $Q_\vartheta(\vartheta|z)$ and $Q_\varphi(\varphi|z)$ which are assumed independent. Thus $Q(\vartheta) = Q_\vartheta(\vartheta|z)Q_\varphi(\varphi|z)$. $Q(\vartheta)$ nd the likelihood have the same structure simplifying the integration that became a process of updating the posterior hyper-parameters [9].

## 1.2 Brain Connectivity

The brain can be considered as a network consisting of a large number of distinct regions, each with its own task and function, but which continuously share information respectively.
In physiology, it is known that there are many mechanisms that contribute to the creation of connections within the brain: epigenetic and genetic factors, but also processes that depend on experience.
Cell plasticity, which characterises cell migration and neurogenesis in the developing brain, and synaptic plasticity are two key physiological factors in brain connectivity. The latter refers to the intensity of synaptic connections, as neurons and neural populations interact through their afferent and efferent connections in such a way as to be able to perform different sensorimotor and cognitive tasks. Therefore, given the interactions between the different neural populations, it is clear that they do not function independently. By contrast they form a complex integrative network, the brain network, in which information is continuously processed and transported between the connected regions.
Finally, the brain network can be defined as consisting of spatially distributed

but functionally connected regions. However, how functions and connections are spread in the human brain is still a field of continuous research and study. For this reason the brain connectivity has become a dominant concept in neuroscience [11].

### 1.2.1 Localizationism and Connectionism

The theory of *localizationism* and the theory of *connectionism* were the two opposite ways of interpreting brain functions throughout the $19^{th}$ century. Underlying functional localizationism is the idea that individual psychic and cognitive functions are associated with one and only one region of the brain, i.e. "one-to-one" mapping. However, studies have shown this theory to be unfounded: neural units are not isolated, but what has been found experimentally for all cognitive domains is a "one-to-many" and "many-to-one" mapping [12] [13].
Evidence to the disproof of functional localizationism is for example what is called the *disconnection syndrome*, i.e. information processing in a local and anatomically intact area is altered when input, coming from distinct and remote regions, is affected due to lesions in its white or grey matter [14].
Therefore, this principle has been replaced by the theory of *connectionism*, according to which, brain regions have specific functions, but processing is influenced by the temporal effects of different areas from which the input comes [15].
For this reason, reference should be made to the overall behaviour of the nervous system.
At the basis of the concept of connectionism are *functional specialisation* and *functional integration*. These are complementary concepts, as they refer to the fact that brain regions dedicated to a specific function may involve further specialised regions whose combination results in functional integration. Hence, the functional specialisation of a cortical structure becomes meaningful only in the context of functional integration and vice versa [16].

### 1.2.2 Functional Specialization and Functional Integration

Functional specialisation is based on the concept that specific brain regions are dedicated in processing certain information. This translates into the fact that, if a task is performed on a subject, changes in activity can be detected only in the brain regions that are interested in the given cognitive or sensorimotor input. However the single brain region is the location of a set of elemental operations, not a complex group of mental faculties that rather derive from the reciprocal

connections between the numerous brain areas. Functional integration refers to the reciprocal correlation and interaction between the different areas of the brain that underlie any cognitive or sensory-motor task [17].
A further aspect to highlight in the theory of functional integration between the different specialised brain regions is also the reciprocal proximity between these areas. If we consider, for example, the temporal lobe, functionally involved in the perception of words, this is surrounded by the auditory cortex and other cortical areas, which integrate acoustic, visual and somatic information into complex perceptions. Therefore the temporal lobe is in an optimal position to interact with the surrounding regions, which have functions closely related to the purpose of the first one. However, proximity from an anatomical point of view is not a necessary requirement, but even anatomically distant regions interact with each other for the same function [18].

### 1.2.3 Types of connectivity

In order to have a clear and complete view of the mechanisms underlying information processing in the brain, the study of the connectivity between the different cerebral regions is crucial.
Connectomics studies include: *anatomical-structural connectivity, functional connectivity* and *effective connectivity*.

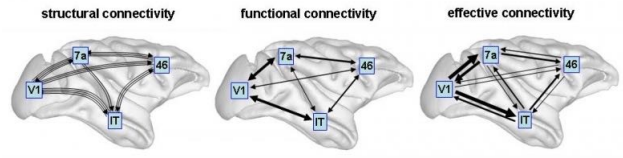


**Figure 1.4:** Schematic representation of the three different types of connectivity [19].

#### Anatomical-structural connectivity

Anatomical or structural connectivity refers to the presence of anatomical connections, i.e. axons connecting different areas. The study can be carried out by means of imaging techniques such dMRI (Diffusion Magnetic Resonance Imaging) in vivo, which allow indirect evaluation at the macroscale/mesoscale of the fibers connecting pools of neural cells.
Concerning the DTI (Diffusion Tensor Imaging) technique, it is sensitive to the diffusion of water molecules with respect to a predefined direction and since this

is constrained by the cell membrane, an estimate of fibers orientation can be obtained from the diffusive direction [20]. However, tractography algorithms, which

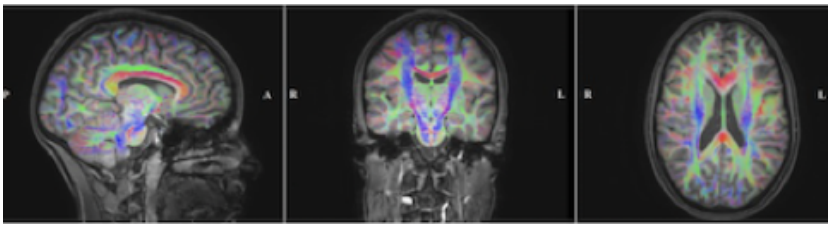

**Figure 1.5:** Diffusion directions obtained from DTI. Sagittal (left), coronal (middle) and axial (right) slice of the color coded fractional anisotropy (FA) map computed from the registered diffusion tensors and plotted on the registered T1w-MRI. The color indicates the main fiber orientation: red is left-right, green is anterior-posterior and blue is superior-inferior [21].

aim to reconstruct white matter fibre tracts from diffusion MRI data, have been demonstrated to generate a significant number of false-positive connections between brain regions. This is due to the fact that whenever two axon bundles are organised in a crossing or kissing configuration, in vivo tractography cannot distinguish their actual trajectories from diffusion data. This implies the presence of many spurious entries in the structural contectome obtained from a tractogram. Consequently, structural connectivity is biased, with some connections being more faithfully identified than others. This type of connectivity is relatively stable over time, but it is not possible to discriminate between excitatory and inhibitory connectivity.

### Functional connectivity

Functional connectivity is typically defined as the temporal correlation of neuronal activation patterns of anatomically separated brain regions [22].
Imaging techniques that provide information on functional connectivity are mainly fMRI (functional magnetic resonance imaging), EEG (electroencephalography) and MEG (magnetoencephalography), and numerous methodologies can be exploited. However, considering the time series of two distinct but functionally related brain areas, it is not possible with functional connectivity alone to define which conditions the other, whether they influence each other or if a third modulates them. For this purpose effective connectivity must be studied, which therefore considers the causality of the correlations.

### Effective connectivity

Effective connectivity provides information on the influence of one neuronal system on another, reflecting causal interactions between activated brain areas [23]. The aim is to find the simplest possible model that generates the observed temporal relationship between the recorded neurons.
The imaging methodologies most commonly used to study effective connectivity are fMRI, EEG and MEG. While several methods are used to obtain the actual connectivity maps, most generally reference is made to dynamic causal modelling, Granger causality and structural equation modelling.

## 1.3 Metabolic Connectivity

The study of brain function and thus of the connectivity of cerebral areas, through the development of new technologies and imaging methodologies, has been addressed in greater depth in recent decades. In particular, the main focus is on functional connectivity (FC), which describes the synchronous oscillations of activity in distinct areas of the brain.
The majority of studies in the literature have been conducted by means of functional magnetic resonance imaging (fMRI) that was essential to delineate the human connectome. Ogawa et al. introduced fMRI, a technique that is based on the BOLD (blood oxygenation level dependent) signal, thus on contrasts dependent on the level of oxygen present in the blood [24]. However, the complex relationships between blood oxygenation, cerebral metabolic rate of oxygen ($CMRO_2$), cerebral blood flow (CBF), and changes in cerebral blood volume (CBV) are all involved in a single fMRI signal. Thus, a complete and clear description of these relationships has not yet been provided. In addition, fMRI has some other drawbacks, including that the BOLD signal only indirectly reflects neuronal activity through hemodynamic changes and an high sensitivity to artifacts such as the motion artifact, particularly problematic in developmental or clinical populations, where movement is correlated with the independent variable of interest (age, diagnosis). However, the BOLD signal can also be influenced by a number of other sources that can be labelled as noise, e.g. physiological sources (e.g. breathing and cardiac characteristics) as well as random noise (e.g. thermal noise).
For these reasons, functional MRI is far from being considered the "gold standard" technique for studying brain connectivity.
In comparison, positron emission tomography (PET) has recently grow in pop-

ularity in the connectivity literature as it can directly reflect neuronal and glial activity. PET connectivity is an emerging research area in neuroscience to which two symposiums have been dedicated last year at OHBM 2021 and this year at Brain&BrainPET 2022, and on which the major centres working on brain PET are focusing, like: Yale (Richard Carson), Harvard (Martinos Center), MedUni Wien, Monash University,..

In the PET literature, the most widely used radiopharmaceutical (about 90%) is [$^{18}$F] Fluorodeoxyglucose (FDG), which, being a glucose analogue, is largely utilized as a biomarker of glucose metabolism in the brain. Moreover, it can be used to calculate the so-called *metabolic connectivity* (MC), which refers to the set of relationships between the metabolic rates of different regions. Importantly, if metabolic changes occur in one region, changes also occur in adjacent or distant areas, depending on their related functionality. This might prove very useful in diagnosing degenerative diseases, which cause alterations in large-scale brain networks.

Advantages that justify FDG-PET metabolic connectivity studies definitely include the better signal-to-noise ratio compared with fMRI data, has greater between-subject reproducibility and robustness from a methodological point of view. Regarding the latter aspect, it is related to the fact that while there are established methods to correct FDG-PET data for partial volume effects, there is no such compensation established for fMRI data. This is a relevant problem in the case of elderly subjects and in neurodegenerative conditions, in which brain atrophy is pronounced.

### 1.3.1 State of the Art on Metabolic Connectivity

The idea of relating regional cerebral metabolic rate for glucose (rCMRglc) from different brain regions was first introduced by Macko et al., 1982, with a visual mapping experiment [25]. However, in that study, correlations between regions were inferred by simply examining individual rCMRglc values, not by an explicit quantitative correlation algorithm. The experiment consisted of first dissecting an optic tract in four monkeys and then they were administered [$^{14}$C]2DG followed by a bright, high-contrast visual pattern. The brain was divided into regions, in each the rCMRglc was determined, then a comparison between normal and blinded side was performed. As a result, what has been observed is that the metabolic rate of the blind side was 30% of the healthy side in the visual area OCiv (layer iv of the striate cortex), 72% of the normal in the prefrontal area

FDv, but unchanged in the temporal lobe area TC. In terms of correlations, when rCMRglc in OCiv was low, it was also low in FDv, when it was high in OCiv, it was also high in FDv. Thus, these two areas showed a high correlation between their rCMRglc values. Macko concluded that regions with high reciprocal correlations participate in visual processing, whereas those with low or no correlations did not.

The idea of deriving functional associations of different brain regions by metabolic activity was later taken up by Horwitz et al. in 1984, thus pre-dating the introduction of fMRI [26]. The research group performed a correlational analysis between regional brain metabolic rates for glucose by positron emission tomography using 2-[$^{18}$F]fluoro-2-deoxy-D-glucose (FDG) as a tracer. On the basis of the relationships derived between regional metabolic rates, it was suggested that areas of the brain whose rCMRglc values are significantly correlated are functionally associated, and the strength of these relationships is proportional to the magnitude of the correlation coefficient. The study focused on determining brain metabolism in forty healthy adult men under conditions of reduced auditory and visual input by calculating partial correlation coefficients for rCMRglc between each pair of regions while holding CMRglc (whole brain glucose metabolism) constant. The partial correlation coefficients measure how two quantities covary independently of the effect on each of a third quantity, and correlations with p-values $< 0.01$ were considered statistically significant. The findings of this research demonstrated that the largest values of the partial correlation coefficients were between homologous brain regions, showing how they were significantly correlated with each other. Furthermore, the correlations between any two lobes in the right hemisphere did not differ significantly from the corresponding pattern in the left hemisphere. Therefore it follows that both hemispheres function more or less similarly with regard to the inter-lobe pairings. The results of the correlations between the regions also showed statistically significant relationships between the primary somatosensory areas with the frontal lobe regions, however, this was not shown for the primary visual and auditory areas. Further observation concerns the high number of correlations identified between frontal and parietal lobe regions, on one hand, and between temporal and occipital lobe regions, on the other, but few statistically significant correlations between these two domains.

Thus, metabolic connectivity obtained with FDG-PET seemed to provide relevant insights for the study of brain activity and cognitive function.

### MC from static PET images

Hence, in the last few years, there has emerged a strong interest of the scientific community in the study and development of methods to assess metabolic connectivity by [$^{18}$F]FDG PET. However, most studies in the literature, instead of exploiting the temporal information of dynamic PET, rely on conventional static measures to derive *group-level* MC as the covariation of metabolic information across subjects. The metabolic connectivity thus obtained will be referred as *subject-series* MC.
The review by Yakushev et al. (2017) provides an outline of the most widely used and well-established approaches in Metabolic Connectivity from static PET [27]. These are:

- Seed correlation or IRCA, which involves choosing a reference site and quantifying the correlation with FDG uptake for every other voxel in the brain, as in Lee et al., 2008 [28].
- Principal component analysis (PCA) and independent component analysis (ICA), which are multivariate decomposition techniques that impose orthogonality and statistical independence constraints on the derived components, as in Di and Biswal, 2012 [29].
- Sparse inverse covariance estimation (SICE), also called graphical lasso, which estimates the connectivity map by imposing a sparsity constraint on the precision matrix (equal to the inverse covariance), as in Huang et al., 2010 [30].
- Graph theory, which is based on the similarity matrix where the sparsity is obtained by applying a threshold to the correlation values, resulting in binary adjacency matrices, as in Yao et al., 2010 [31].

Quantification of metabolic connectivity from static [$^{18}$F]FDG PET data is routinely performed using the standard uptake value (SUV) calculated at a fixed sampling time and for each region of interest or voxel.
However, connectivity studies based on static PET are in opposition to those performed with other imaging techniques, including fMRI, where functional connectivity matrices are obtained at the *individual-subject level* via temporal correlations (i.e. dynamic data) between signal time series [32]. Very few studies are based on dynamic PET and only three of which were conducted with human participants.

### MC from dynamic PET images

In the study performed by Wehrl et al. (2013) on 8 rats, functional connectivity information obtained from BOLD-fMRI and dynamic PET with [$^{18}$F]FDG tracer was compared by means of independent component analysis using the Group ICA Toolbox (GIFT) [33]. This approach for dynamic PET data had never been used before and allowed to highlight seven networks showing similarities to those described in the fMRI literature, but with smaller area [34].The result of the study indicates that fundamental information about brain networks is encoded in dynamic PET data, which is however largely unused by conventional image analysis methods.

The study presented by Passow et al. (2015) involved eight healthy right-handed male participants (mean age $53.1 \pm 10.5$) with no history of neurological or psychiatric conditions [35]. Again, the aim is to perform a comparative analysis of fMRI and FDG-PET data to investigate the link between metabolic activity and functional connectivity within and across brain networks. To do so, each dataset was subjected to a Default Mode Network (DMN) seed-based correlation analysis. The results of the study showed spatial similarities between fluctuations in the BOLD signal and fluctuations in local glucose consumption. This leads to the hypothesis that the BOLD signal, and thus functional connectivity at rest, results from dynamic changes in brain metabolism, a direct measure of ongoing neuronal activity.

A further study carried out on 53 healthy participants is conducted by Tomasi et al. (2017) based on group independent component analysis (gICA) to assess associations between metabolic connectivity (from FDG-PET) and functional connectivity (from rfMRI) [36]. The gICA on rfMRI data identified 22 different subnetwork components integrating major networks such as visual, motor, language, default mode, cerebellar and dorsal attention. However, the gICA on FDG-PET data did not report this rich set of networks, but identified only two anticorrelated ones. The first component incorporates cerebellum, pons, medial temporal cortex regions and anterior thalamus, while the second component includes cortical regions.

The study conducted by Amend et al., 2019 is also based on dynamic PET images [37]. From this data, brain connectivity was derived by calculating the Pearson correlation coefficient between each pair of regions of interest, based on the Schiffer rat brain atlas [38]. By integrating simultaneous resting-state fMRI and dynamic [$^{18}$F]FDG-PET measurements in the rat brain, homotopic correlations

between both modalities were identified, suggesting an underlying synchrony between hemodynamic processes and glucose consumption.
A further study by Ionescu and colleagues (2021) focuses on a resting-state network (RSN) analysis from a simultaneous acquisition of PET/fMRI data performed on 30 rats [39]. The aim is to compare brain connectivity derived from fMRI and [$^{18}$F]FDG-PET during the resting-state and for this purpose independent component analysis and pairwise correlation analysis were employed. The results reported three RSNs with a high degree of similarity between PET and fMRI: default mode network, basal ganglia network and cerebellar-midbrain network. This confirmed a close link between local synaptic glucose consumption and BOLD fluctuations. However, connectivity by [$^{18}$F]FDG indicated greater integration between often distant brain areas, compared to that obtained by more segregated fMRI-derived FC. Furthermore, several networks specific to both imaging modalities were identified by ICA, underlining the complementarity of these approaches, suggesting how a hybrid study can contribute to a greater understanding of brain function and could be interesting for clinical applications. Such complementarity was explained considering that haemodynamic and [$^{18}$F]FDG tracer fluctuations occur on different time scales, thus representing two interconnected but distinct physiological readouts.
Finally, in the work of Volpi et al. (2021) similarity-based approaches (Pearson correlation, Euclidean distance and Cosine similarity) and sparse inverse covariance estimation (SICE) methods were tested to quantify metabolic connectivity from dynamic [$^{18}$F]FDG-PET at the single subject level [40]. These approaches were combined with three different TAC standardisation strategies and tested on four healthy subjects. The obtained metabolic connectivity matrices were compared in terms of graph structure, inter-subject reproducibility and similarity to a structural connectivity (SC) model. What emerged was that Pearson correlation, Euclidean distance and Cosine similarity (i.e. non-SICE methods) provided better results for between-subject reproducibility and similarity to SC. In particular, interhemispheric and homotopic connections, expected from brain connectivity studies, were highlighted. Moreover, the choice of standardisation method for TAC PET leads to non-trivial differences between networks that will be discussed later. The standardisation of time activity curves was already introduced in the studies by Amend et al. (2019) and Tomasi et al. (2017) and is necessary in order to correct for non-intrinsic correlations generated by factors such as increased absorption of the [$^{18}$F]FDG-PET tracer. In the two studies

mentioned above, a normalisation, which will later be referred to as normalisation 1 (number 3 in the study by Volpi et al.), was attempted to evaluate fluctuations around the metabolic baseline. While a correlation (or ICA) approach, like that one employed by Amed and Tomasi, necessarily requires PET signal standardization to assess covariation in its fluctuations, ideally one would prefer a method that reflects and maintains the overall physiological signal.
For what concerns the MC-SC similarity, the non-SICE methods have higher Dice values (0.3-0.4) than the SICE methods (0.2-0.3).
However, such studies comparing metabolic connectivity with functional and structural connectivity do not provide clear insight into the underlying physiology, which is why supplementation with information with stronger biological interpretability (e.g., receptor/synaptic density) would be extremely informative. The metabolic connectivity obtained from dynamic PET data allow to estimate MC matrices at single subject level and will be referred as *time-series* MC.

Furthermore, PET studies can be performed with two different protocols: bolus injection and continuous infusion. In this thesis, only PET bolus injection will be dealt with, as the available data are of this type and it is in any case the most commonly used technique. While tracer availability decreases over time using a bolus injection, a constant infusion allows the maintenance of a stable plasma supply of [$^{18}$F]FDG and this technique was named "functional PET' (fPET). This technique improved sensitivity to brain-state changes and better temporal dynamics, in comparison to bolus PET, in order to track dynamic changes of glucose uptake over time. Several studies have demonstrated that fPET can isolate task related changes in glucose uptake [41, 42]. This technique was adopted in both the study by Amend et al., (2019), and Li et al., (2020) [43]. In Amend et al., the normalisation in performed by determining a whole-brain mean value of the measured signal at each time point and the value of each ROI was then divided by its respective whole-brain mean. Instead in Li et al., the global baseline was removed by normalising the data of each volume to remove the mean in each voxel and divide the voxel wise standard derivation of each volume. These types of normalisation performed allows to remove a global baseline as well as to remove non-intrinsic correlations by applying Pearson's correlation and ICA on the fluctuations.

# Chapter 2

# Materials and Methods

In this chapter it will be described the available dataset, on which the study was performed.
A brief introduction to structural pre-processing and coregistration, which allowed to make the data suitable for the application, will then be discussed.
Finally, the methods adopted for the study and estimation of the brain metabolic connectivity, using dynamic [$^{18}$F]FDG Positron Emission Tomography, both at region and voxel level, will be described.

## 2.1 Material

The dataset under study is a part of the WASHU VG LAB dataset, from the Washington University in Saint Louis, MO, USA.
Specifically, the sub-dataset on which the present study was performed included 71 subjects, 39 females and 32 males ($56 \pm 15$ years old).

### 2.1.1 [$^{18}$F]FDG PET data

PET data were collected on the Siemens ECAT HR+ 962 PET scanner. To minimize head movement, a softened thermoplastic mask with enlarged eye holes was placed on the head and secured. PET scans were performed after slow i.v. injection of 5 mCi of FDG.
Two different reconstruction algorithms were applied: filtered back-projection (FBP) and ordered subset expectation maximization (OSEM), see fig. 2.1. For this thesis work, all analysis were performed on FBP and the chosen recon-

struction grid consisted of 24x5-second frames, 9x20-second frames, 10x1-minute frames, and 9x5-minute frames, see fig. 2.2.
However, for some subjects issues in the acquisition led to alterations in the time grid, particularly to the number of 5-second frames.

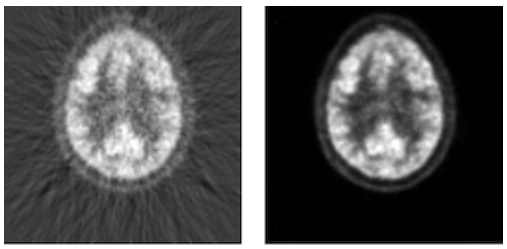

**Figure 2.1:** Axial slice from images reconstructed by the two different algorithms. Left: FBP, right: OSEM.

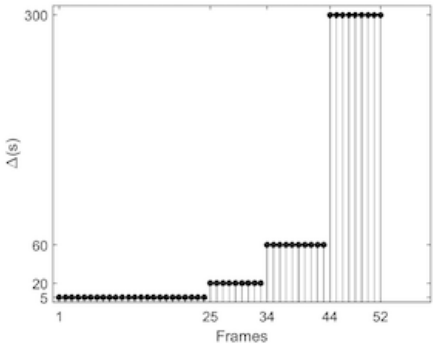


**Figure 2.2:** PET reconstruction time grid: 4x5-second frames, 9x20-second frames, 10x1-minute frames, and 9x5-minute frames.

In table A.1 is report the table with the ID that allows the identification, age, sex and the characteristics of the time grid for each of the 71 subjects.

### 2.1.2 MRI data

For the same cohort of individuals who underwent PET dynamic acquistions, MRI images were separately collected via Siemens (Siemens Medical Solutions USA, Inc) MAGNETOM Prisma MRI scanner.
For each subject, Multi-echo T1w MPRAGE was provided, (TR=2500,TI=1000 ms, TE=1.81, 3.6, 5.39, 7.18 ms, voxel size=0.8 x 0.8 x 0.8 mm).

## 2.2 Methods

### 2.2.1 Tools

Data have been inspected and processed using: MATLAB R2021b, Advanced Normalization Tools and FSL v6.0.
Some packages have been downloaded to extend MATLAB functionalities: SPM12, "Tools for NIfTI and ANALYZE image" v1.27 and Group ICA of fMRI Toolbox (GIFT) v1.3h.

### 2.2.2 Structural Image pre-processing

All subjects were pre-processed according to the procedures implemented in the pipeline of the Padova research team.
Pre-processing was performed on T1w images, which were later used to coregister and normalize PET data.

#### Bias Field Correction and Skull Stripping

T1w structural images were initially corrected for field bias using the N4 algorithm [44]. This consists of a presence of low-frequency intensity non-uniformity in the image data, also known as bias, inhomogeneity, illumination non-uniformity, or field gain. The result can be that in some areas white matter has the same intensity as gray matter, causing low reliability in classifiers. In fact, tissue segmentation is based on signal intensity, so it is crucial to correct for intensity non-uniformity in order not to affect tissue class probability assignment.
Along with Bias Field Correction, an additional preprocessing step is performed, i.e., T1w structural images are skull stripped. This is a crucial step since high-resolution MRI brain images contain some non-brain tissues such as skin, fat, muscle, neck, and eyeballs compared to functional images like PET that usually contain relatively less non-brain contrast. The presence of these tissues is considered a major obstacle for automated brain image segmentation and analysis techniques, therefore, it is essential to perform a preliminary step to isolate the brain from extracranial or non-brain tissues from MRI scans of the head [45].
These steps were accomplished through the use of ANTs (Advanced Normalization Tools), and obtain as output the image *T1w_N4.nii*.

### Segmentation

Segmentation of the T1-weighted image (*T1w_N4.nii*). The goal of segmentation is to separate tissue classes, and the information used for this purpose is the intensity of the image voxels. This means that different tissue types emit signals of different strengths, and therefore different intensities: white matter is the brightest, followed by gray matter and cerebrospinal fluid. However in T1w images, some factors can lead to a variation in voxel intensities, for example this can be due to biological variability, measurement error and in particular partial volume effects. Regarding the latter, it is an effect that occurs when a voxel extends over more than one tissue.
The probabilistic approach is based on assigning high probabilities in the case where intensities clearly reflect white matter or gray matter, while intermediate probability values reflect partial volume effects.
It follows that the output of the tissue class segmentation step assigns to each voxel the probabilities that the voxel belongs to each tissue class.
There are several tools available for brain tissue segmentation and Statistical Parametric Mapping (SPM) software was used in this study [46].
In SPM, the segmentation routine automatically segments the incoming MR image into gray matter (*c1T1w.nii*), white matter (*c2T1w.nii*), and cerebrospinal fluid (*c3T1w.nii*), but this classification, as outlined above, is probabilistic.

### Normalization

In the structural pre-processing step, brain normalization is performed. This is a procedure to map individual brain images to a standard anatomical coordinate space.
It is required to define a reference image, or Atlas, representing a standard anatomy, for this purpose MNI (Montreal Neurological Institute) models are commonly used. There are several MNI spaces available today, and even subtle changes between spaces can impact results. Such atlases can be used by automated spatial normalization software and should reflect the average neuroanatomy. The International Consortium of Brain Mapping (ICBM) has adopted these models as an international standard.
The first MNI model is MNI305, which was updated in 2009, MNI152 NLIN 2009, and is available in three versions, 2009a, 2009b and 2009c (the latter is the one chosen for our normalisation), each of which has a symmetric and an asymmetric version [47].

Normalization was performed using ANTs registration method.

#### Hammers segmentation to T1 mapping

During the structural preprocessing phase, an additional step performed is to bring the Hammers segmentation into T1 space, using ANTs.
The Hammers atlas identifies 83 cortical and subcortical regions (see table B.1) [48], including both gray and white matter. Therefore, the probabilistic gray matter map obtained via SPM was thresholded, choosing in this first part a very conservative threshold, i.e., 0.2. This allowed to obtain a binary map, so the value of the voxel is equal to one only if that particular voxel has a probability of belonging to gray matter greater than 20%, otherwise it is zero. The mask is applied to Hammers parcellation in T1 space, obtaining *Hammers_2_T1_GM.nii*, while *Hammers_2_T1.nii* in case of none mask applied.

### 2.2.3 Motion Correction

The images acquired frame by frame can be corrupted by any movement of the subject during acquisition, even slight movements of the head or body can cause obvious alterations in the recorded signals. The ever-present artifacts, moreover, are due to physiological oscillations, such as breathing, which cause minimal but noticeable shifts.
Therefore, motion correction consists in coregistering the PET volumes corresponding to the final frames (last 5 frames), on a frame chosen as a reference, i.e. the one corresponding to the first frame of 5 minutes. This step is performed because the final frames are the longest in terms of time and motion on these can have a strong impact, i.e., there can be significant misalignment between one frame and another. As for the remaining frames, they were not corrected for motion because of their low signal-to-noise ratio and also, the initial frames do not have clear anatomical structures that can be aligned.
The Motion Correction step is implemented in the pipeline by an in-house script that calls a set of Piwave tools in Matlab [49], that use wavelet filters, in order to realigne a time-series of PET images from the same subject using a least square approach and a 6-parameter (rigid body) spatial transformation. After the estimation of the 6 parameters each volume is resliced using a B-spline interpolation method.
Once the motion correction was performed on the dynamic PET (*PET_DYN_MoCo.nii*), the summed static PET image (*PET_DYN_MoCo_last.nii*) was calcu-

lated, considering also in this case the sum only on the last frames, in particular the last 4 (5 minutes frame). Generally in fact the static PET is obtained considering the last 20 minutes (from minute 40 to 60).

### 2.2.4 Coregistration

The obtained static PET image is mapped onto the T1 image of the same subject, obtaining *PET_static_MoCo_2_T1.nii*. This step is performed using ANTs. It is also obtained in output the affine transformation matrix used to perform this coregistration.
In addition, in the structural preprocessing step, segmentation with the Hammers atlas was performed in T1 space. It is possible to map this segmentation from T1 space to PET space, inverting the transformation matrix estimated in the previous step. This was also performed with ANTs, obtaining *Hammers_2_PET.nii* and *Hammers_2_PET_GM.nii*
Finally, considering SPM segmentation, this provided probability maps representing the odds of a voxel belonging to gray matter (GM), white matter (WM) and cerebrospinal fluid (CSF). These were appropriately thresholded using two different thresholds in order to obtain a mask containing voxels that have a probability of belonging to grey matter $> 0.5$ and a mask containing voxels that have a probability of not belonging to CSF $> 0.95$. These maps, however, are still in T1 space and to bring them into PET space the previously estimated transformation matrix and a Nearest Neighbor interpolation are used.

#### Schaefer to PET mapping

In this study, parcellation was also performed using the Schaefer Functional Atlas, with 100 and 200 parcels, both at 7 and 17 networks [50].
This atlas is based on the influential brain networks published by Thomas Yeo (2011) [51], and these new parcels add further refinement by sub-partitioning the global networks on the basis of a local gradient approach. The parcels are available in different versions and subdivide the cortex into up to 1000 regions based on rs-fMRI.
The Schaefer atlas (MNI FSL) is mapped to PET space using the transforms already estimated in the previous steps.

### 2.2.5 Estimation of metabolic connectivity matrices at parcel level

#### Parcellation with Hammers Anatomical Atlas

It was decided to use for the cortical regions, Cerebellum, Hippocampus and Amygdala a segmentation with the mask containing the voxels that have a probability of belonging to the GM $> 0.5$, while for the subcortical regions Caudate, Accumbens, Putamen, Thalamus and Pallidus the segmentation with the not-CSF mask $> 0.95$ was adopted. For this purpose, the Hammers anatomical atlas appropriately mapped in PET space and to which the grey mask had not previously been applied (*Hammers_2_PET.nii*) was segmented with the not-CSF mask $> 0.95$, while the Hammers anatomical atlas in PET space that was already previously masked with the grey mask (*Hammers_2_PET_GM.nii*) was segmented with the GM mask $> 0.5$.
This type of segmentation made it possible to have a sufficiently high number of voxels even in subcortical regions such as Pallidus, where a more aggressive segmentation like GM $> 0.5$ resulted in few voxels per parcel.
The voxels from the dynamic (motion-corrected) PET were then extracted from each parcel defined by the appropriately segmented Hammers atlas and the time series of each parcels was derived as the average of the time series of the voxels of that specific region:

$$X_I = \frac{1}{N_I} \sum x_i \tag{2.1}$$

where $I$ is the parcel under consideration, $N_I$ is the number of voxels in that parcel, and $x_i$ is the time series of voxel $i$.

Having a reconstruction grid consisting of 24x5-second frames, 9x20-second frames, 10x1-minute frames, and 9x5-minute frames, an interpolation with a uniform virtual grid of 0.6 s step is performed.

#### Data denoising

The initial part of the curves is particularly noisy, so several pre-processing approaches were tested, applied to the first 24 5-second frames:

- Interpolating from frame 1 (no processing);
- interpolating from frame 8 (removing initial frames);

- interpolating from frame 25 (removing all 5-second frames);
- applying to the 5-second frames (the first 24) a moving average filter with a window of 3;
- applying to the 5-second frames (the first 24) a moving average filter with a window of 5;
- averaging the first 24 frames 2 by 2 (subsampling);
- averaging the first 24 frames 3 by 3 (subsampling);
- averaging the first 24 frames 4 by 4 (subsampling);
- averaging the first 24 frames 6 by 6 (subsampling);

### Data standardization

The TAC of the different regions are characterised by a strong multicollinearity. Therefore, various normalisation methods were attempted in this study to resolve this issue. Indeed, in the presence of multicollinearity, it would not be possible to refer to segregation or integration on the connectivity matrices, even after sparsification. The carpet plot (showing times on the *x-axis* and regions on the *y-axis*) of the non-normalised TAC is shown in the fig. 2.3.

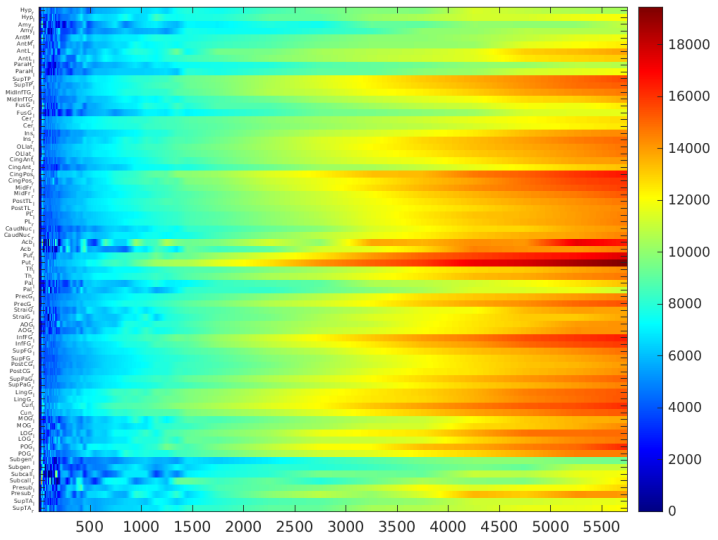


**Figure 2.3:** Carpet plot of the non-normalised TAC for an example subject. Time is shown on the x-axis (in second), and Hammers parcels are on the y-axis.

In normalisation 1 the matrix $X_{S_1}$ is obtained by dividing each row of $X$ by

the average of the rows of $X$, as in Volpi et al., 2021 [40]. The carpet plot of the TAC with normalisation 1 is shown in fig. 2.4.

$$\mu_{WB}(t) = \frac{1}{P}\sum_{i=1}^{P} X(i,t) \qquad \text{for } t = 1, ...T \tag{2.2}$$

$$X_{S_1} = \frac{X}{\mu_{WB}} \tag{2.3}$$

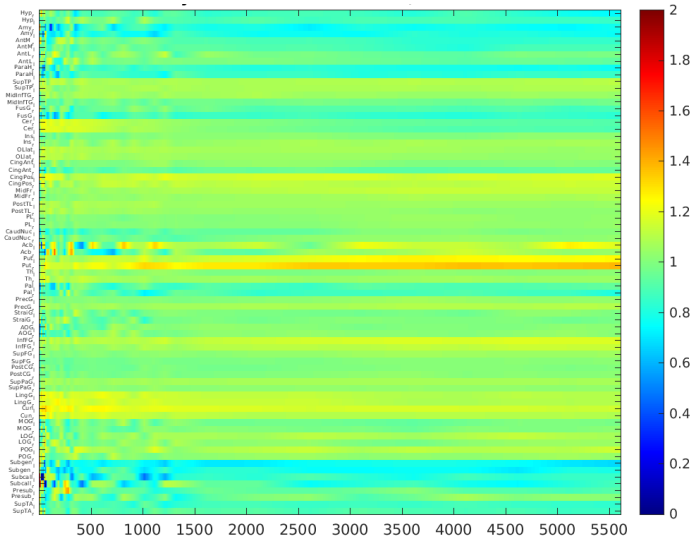


**Figure 2.4:** Carpet plot of the TAC with normalisation 1 for an example subject. Time is shown on the x-axis (in second), and Hammers parcels are on the y-axis.

In normalisation 2, a matrix $X_S$ is obtained by z-scoring $X$: each column of $X$ is centred in order to have mean 0 and scaled in order to have standard deviation 1 (i.e., subtracting the overall mean and dividing by its standard deviation). Subsequently, $X_{S_2}$ is generated by subtracting the mean from each row (i.e. removing the parcel mean), as in Volpi et al., 2021. The carpet plot of the TAC with normalisation 2 is shown in fig. 2.5.

$$\sigma_S(t) = \sqrt{(var(X(:,t)))} \tag{2.4}$$

$$X_S = \frac{X - \mu_{WB}}{\sigma_S} \tag{2.5}$$

$$\mu_{X_S}(t) = \frac{1}{T}\sum_{j=1}^{T} X_S(p,j) \tag{2.6}$$

$$X_{S_2} = X_S - \mu_{X_S} \tag{2.7}$$

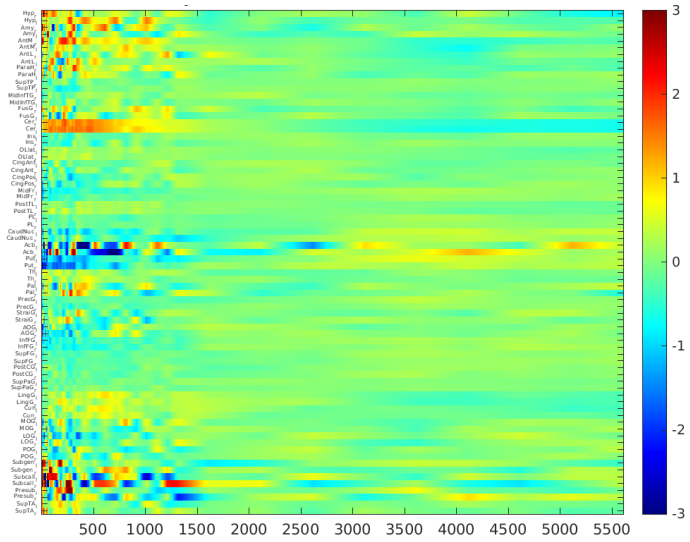


**Figure 2.5:** Carpet plot of the TAC with normalisation 2 for an example subject. Time is shown on the x-axis (in second), and Hammers parcels are on the y-axis.

In normalisation 3, the matrix $X_S$ is obtained by subtracting the mean from each column of $X$. Next, $X_{S_3}$ is generated by z-scoring $X_S$: each row of $X_S$ is centred to have mean 0 and scaled to have standard deviation 1, as in Volpi et al., 2021. The carpet plot of the TAC with normalisation 3 is shown in fig. 2.6.

$$X_S = X - \mu_{WB} \tag{2.8}$$

$$\mu_S(p) = \frac{1}{T}\sum_{j=1}^{T} X_S(p,j) \qquad \text{for } p = 1, ...P \tag{2.9}$$

$$\sigma_S(p) = \sqrt{(var(X_S(p,:)))} \tag{2.10}$$

$$X_{S_3} = \frac{X_S - \mu_S}{\sigma_S} \tag{2.11}$$

In normalisation 4, the matrix $X_{S_4}$ is obtained by dividing $X$ by the plasma concentration curve ($C_p$) of [$^{18}$F]FDG. $C_p$ should ideally be an arterial input function (AIF), but in this case is substituted by an image-derived input function (IDIF), see fig. 2.7. This was extracted from the internal carotid artery via an

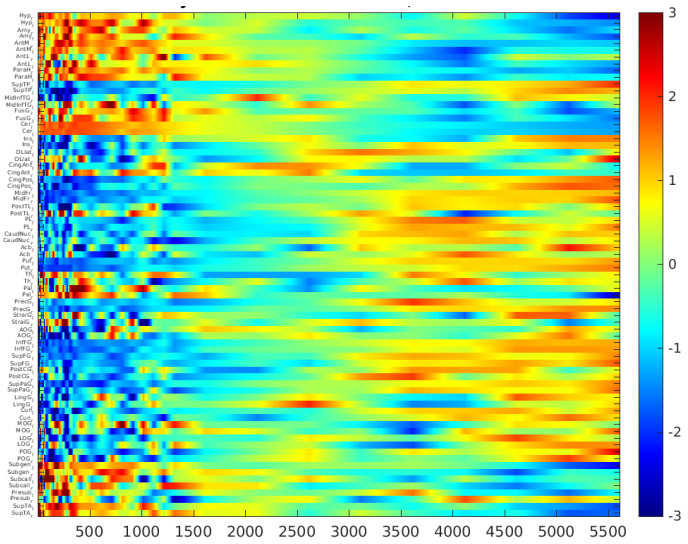


**Figure 2.6:** Carpet plot of the TAC with normalisation 3 for an example subject. Time is shown on the x-axis (in second), and Hammers parcels are on the y-axis.

automatic pipeline (vessel segmentation [52], parametric clustering [53], model fitting [54]), and corrected for spillover with Chen's approach [55].
The carpet plot of the TAC with normalisation 4 is shown in fig. 2.8.

$$X_{S_4} = \frac{X}{C_p} \tag{2.12}$$

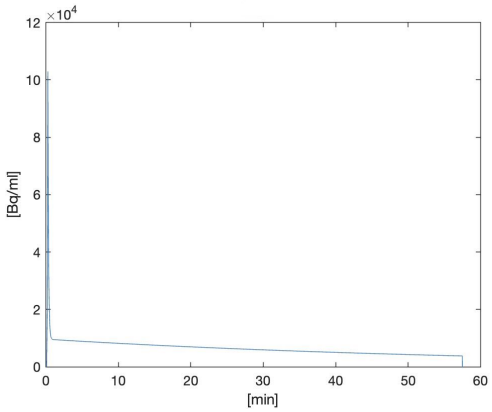


**Figure 2.7:** $C_p$ image-derived input function

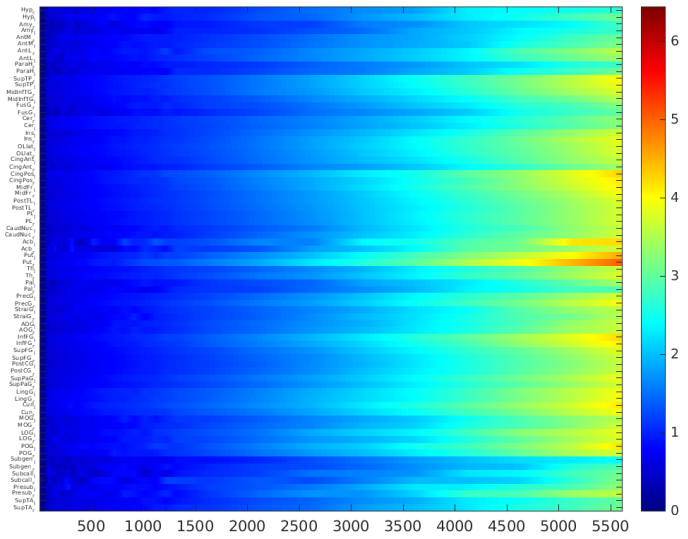


**Figure 2.8:** Carpet plot of the TAC with normalisation 4 for an example subject. Time is shown on the x-axis (in second), and Hammers parcels are on the y-axis.

In normalisation 5, a matrix $X_{S_5}$ is obtained by dividing $X$ by the integral of $C_p$. The carpet plot of the TAC with normalisation 5 is shown in fig. 2.9.

$$X_{S_5} = \frac{X}{\int C_p} \tag{2.13}$$

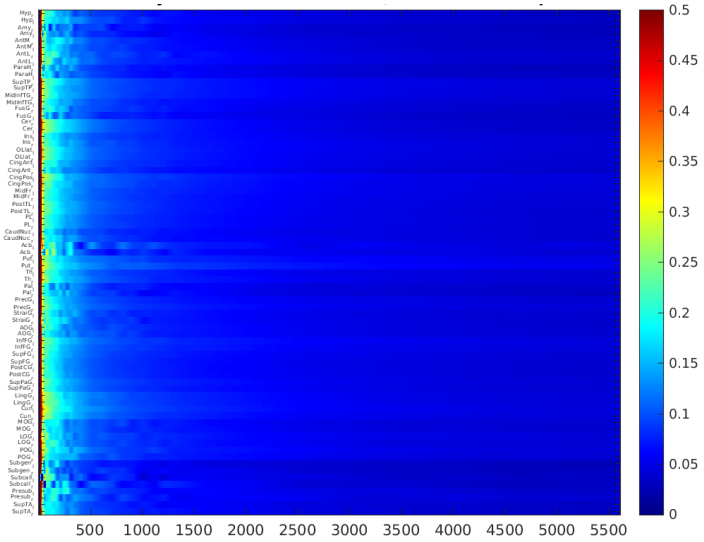


**Figure 2.9:** Carpet plot of the TAC with normalisation 5 for an example subject. Time is shown on the x-axis (in second), and Hammers parcels are on the y-axis.

These types of normalisations highlight different characteristics of the signal, in particular:

- normalisations 1 and 2 emphasise the signal fluctuations around the metabolic baseline or global signal;
- normalisation 3 emphasises the fluctuations of the signal with respect to itself;
- normalisation 4 leads to greater denoising of the initial part, thereby emphasising the tails and their separation;
- normalisation 5 performs the opposite of normalisation 4, thus emphasising mainly the initial part of the curve.

### Similarity-based approaches for Metabolic Connectivity estimation

Four pairwise similarity metrics were applied to the standardised and non-standardised matrices ($X$, $X_{S_1}$, $X_{S_2}$, $X_{S_3}$, $X_{S_4}$, $X_{S_5}$) in order to obtain the *time-series connectivity matrices*, which are:

- Pearson's Bivariate Correlation Coefficient;
- Euclidean Pairwise Similarity;
- Cosine Similarity;
- Gaussian Kernel.

**Pearson's Bivariate Correlation Coefficient**, computed between each pair of ROIs, was calculated as:

$$r = \frac{\sum_{i=1}^{n}(x_{i,1} - \bar{x_1})(x_{i,2} - \bar{x_2})}{\sqrt{\sum_{i=1}^{n}(x_{i,1} - \bar{x_1})}\sqrt{\sum_{i=1}^{n}(x_{i,2} - \bar{x_2})}} \tag{2.14}$$

where $n$ is the number of samples, $x_{i,1}$ and $x_{i,2}$ are the individual samples, and $\bar{x_1}$ and $\bar{x_2}$ are the arithmetic sample averages.

Second, the **Euclidean Pairwise Similarity** was calculated between each pair of ROIs as:

$$d(x_1, x_2) = \sqrt{\sum_{i=1}^{n}(x_{i,1} - x_{i,2})^2} \tag{2.15}$$

Next, a rescaling to the interval [0;1] is performed, then the complement to 1 was calculated to obtain a similarity metric.

Third, **Cosine Similarity** was calculated between every pair of ROIs as:

$$cosSim = \frac{x_1 x_2}{\|x_1\| \, \|x_2\|} = \frac{\sum_{i=1}^{n}(x_{i,1}x_{i,2})}{\sqrt{\sum_{i=1}^{n}(x_{i,1})^2}\sqrt{\sum_{i=1}^{n}(x_{i,2})^2}} \tag{2.16}$$

Finally, the **Gaussian Kernel** was calculated between every pair of ROIs as:

$$GaussKernel = e^{-(\gamma\|x_1 - x_2\|^2)} \tag{2.17}$$

The four different metrics are applied to the matrices $X$, $X_{S_1}$, $X_{S_2}$, $X_{S_3}$, $X_{S_4}$, and $X_{S_5} \in R^{p\times T}$, of each of the 71 subjects, obtained by considering the entire TAC of each parcel. Furthermore, the same metrics and normalisations were applied to the matrices, $\in R^{p\times T}$, obtained considering only the first 10 minutes of the TAC, the first 20 minutes of the TAC, and the last 20 minutes.

Furthermore, in order to relate the concentration of radioactivity measured by PET to underlying physiological or biochemical processes, the application of mathematical models is required. Therefore, the fitting of models for the kinetics of [$^{18}$F]FDG is essential to study regional glucose metabolism. For this reason, the Sokoloff model was applied to the TAC of the [$^{18}$F]FDG tracer, obtaining, for each parcel, the concentration curve of the free [$^{18}$F]FDG tracer in the tissue (compartment 1, see fig. 2.10) and the concentration curve of the tracer phosphorylated by the hexokinase enzyme (compartment 2, see fig. 2.11). The voxel-wise time-courses of $C_1$ and $C_2$ were calculated as:

$$C_1(t) = (1 - V_b)\frac{K_1 k_2}{k_2 + k_3}\mathrm{e}^{-(k_2+k_3)t} \otimes C_p(t) \tag{2.18}$$

$$C_2(t) = (1 - V_b)K_i \int_0^t C_p(\tau)d\tau \tag{2.19}$$

The metrics and normalisations were then applied to the matrices $\in R^{p\times T}$ obtained considering the first compartment time series and the second compartment time series of each parcels, for any of 71 subjects.
The aim was to assess any similarities between the metabolic connectivity matrices obtained considering different portions of the TAC (first 10 minutes, first 20 minutes, last 20 minutes) and the metabolic connectivity matrices obtained

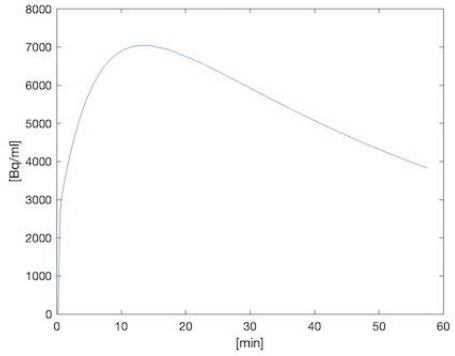


**Figure 2.10:** Concentration curve of the free [$^{18}$F]FDG tracer in the tissue, compartment 1 (left Cerebellum)

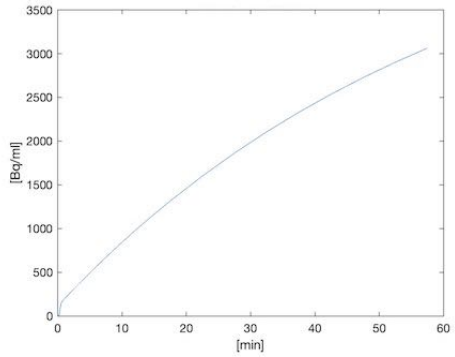


**Figure 2.11:** Concentration curve of the tracer phosphorylated by the hexokinase enzyme, compartment 2 (left Cerebellum)

considering the first compartment and the second compartment time curves.

### MC subject-series

A voxel-level quantification of the [$^{18}$F]FDG PET data, using the Sokoloff model and a Variational Bayesian inference framework [8], is performed in order to derive parametric maps of $K_1$, $k_3$, $K_i$.
Furthermore, the standardised uptake value ratio ($SUVR$) to the whole-brain average [$^{18}$F]FDG uptake was calculated from the dynamic data in the 40-60 min time window.
Subsequently, the voxel-wise maps of $K_1$, $k_3$, $K_i$, $SUVR$ were parcelled using the Hammers anatomical atlas and within-subject normalised by z-score.
Finally, Pearson's correlation matrices across subjects were computed on the $K_1$, $k_3$, $K_i$, $SUVR$, obtaining the *subject-series connectivity matrices*.

### Across-subject and across-method reproducibility

The matrices of each subject were saved both in the full version (without sparsity), but also, since, as for SC and FC, the MC matrix is expected to be sparse, a sparsity threshold was applied to retain only the most significant 20% of the edges [56].

Regarding the *time-series connectivity matrices*, the average MC matrix across subjects was calculated for each metric and for each normalisation (including non-normalised case), again reported both full and sparsity thresholded at the $80^{th}$ percentile.

In order to assess the reproducibility between the methods and thus compare the MC matrices between the different metrics and normalisations, a Pearson correlation was performed between the obtained sparse matrices. Subsequently, by binarising the sparse matrices, Dice's pairwise similarity coefficients between them were also calculated.

Instead, coefficient of variation matrices were calculated to assess inter-subject reproducibility. These were obtained as the element-by-element ratio of the between-subjects standard deviation matrix and the absolute value of the between-subjects mean matrix, multiplied by 100. This gives the percentage variability of each entry between subjects. Both the full matrices of the coefficients of variation and the matrices of the coefficients of variation corresponding to the most significant entries in the mean matrices (20% most significant) were obtained.

### MC subject-series vs MC time-series

It is also useful to examine the similarity and correlation between *subject-series connectivity matrices* and *time-series connectivity matrices*, in order to understand what the matrices normally obtained in the literature (subject-series connectivity matrices) actually reflect. Again, Pearson's correlation coefficients between all possible pairs of sparsified matrices and the Dice coefficient of pairwise similarity, applied after a subsequent binarisation of the matrices, were evaluated.

#### Parcellation with Schaefer Functional Atlas

Parcellation was then performed with the Schaefer functional atlas in the two 100- and 200-parcel versions, both at 7 and 17 Network. Since the Schaefer atlas is only cortical, it was decided to use a segmentation with a mask containing the voxels that have a probability of belonging to GM $> 0.5$. As far as the subcortical regions are concerned, these were introduced from the Hammers anatomical atlas, with the segmentations set out above.
Again, as in the Hammers case, the time series of each parcel was derived as the average of the time series of the voxels of that specific region, see equation 2.1.

For each of the 71 subjects a matrix $X \in R^{p \times T}$ is obtained, where $p$ is the number of parcels, 100 or 200, and T is the size of the time grid.
The steps of data denoising, data standardisation, similarity-based approach, calculation of MC subject-series matrices and evaluation of across-subject and across-method reproducibility were also performed for the case of parcellization with Schaefer functional atlas.

### 2.2.6 Graph theory metrics and hubs

In connectomics studies, the topology of the brain network is usually investigated using graph theory. In the present study, each of the derived metabolic connectivity matrices, sparsified with a threshold at the $80^{th}$ percentile, was translated into a network, considering each ROI as a node and each interregional association as an edge, see fig. 2.12. Then, using the Brain Connectivity Toolbox [57], degree, stenght and eigenvector centrality were derived for each parcel (node).
Degree is defined as the number of connections of a node, while the eigenvector centrality of a node is high when it is connected to many nodes with a high degree, see fig. 2.13. Finally, node strength is defined as the sum of the weighted edges of a node.

The next step was to derive hubs, i.e. regions that integrate and distribute information due to the number and position of their connections. The loss of these well-connected hubs can be particularly devastating for the functioning of the network. Given the role of hubs and their importance for the brain network, their location and functions are of clear interest to neuroscientists, so their characterisation was a crucial step.

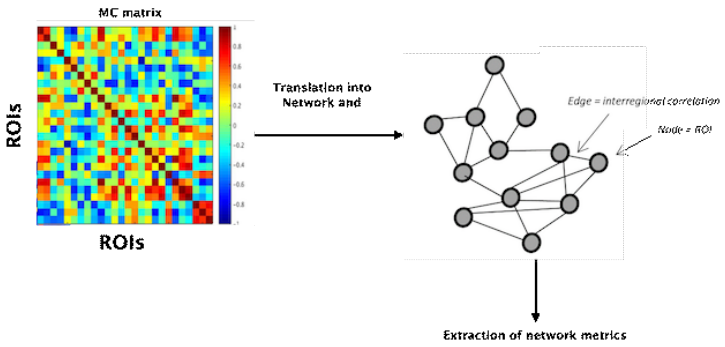


**Figure 2.12:** The PET MC matrix is translated into a network, where nodes are ROIs and interregional associations are link. Thresholding is aplied to preserve the strongest connections. before any metric is extracted as representation of the biological organisation of the PET tracer across the brain (adapted from [58]).

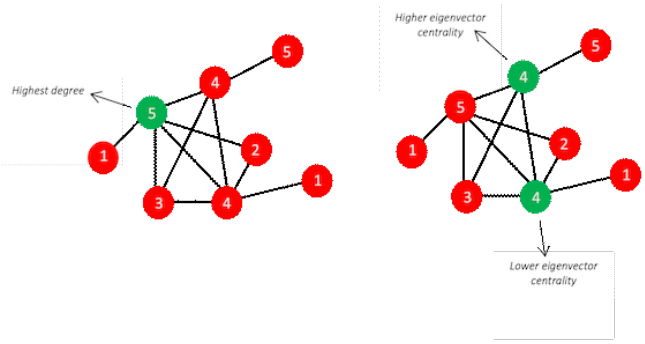


**Figure 2.13:** Degree (number inside each node) and Eigenvector centrality, for a simple network.

The definition of hubs is not unique, but in the following study it is opted to identify them as the nodes belonging to the top 20% of both degree and eigenvector centrality distributions [57].

Other studies were then carried out.
Degree, eigenvector centrality and strength were calculated on the MC time-series matrices, imposing a sparsity with a threshold at the $80^{th}$ percentile (a test without imposing sparsity was also performed for strength and eigenvector centrality). From the $region \times subject$ matrices of $K_1$, $k_3$, $K_i$ and $SUVR$, testing both without any z-scores and with z-scores, an average between subjects was performed. Each mean vector of $K_1$, $k_3$, $K_i$ and $SUVR$ was correlated with degree, strength and eigenvector centrality of the time-series connectivity matrices.
The degree, eigenvector centrality and strength on the MC subject-series matrices of $K_1$, $k_3$, $K_i$ and $SUVR$ were calculated, imposing a sparsity with threshold at the $80^{th}$ percentile. Each mean vector of $K_1$, $k_3$, $K_i$ and $SUVR$ was correlated with the degree, strength and centrality of the eigenvectors of the MC matrices.

### 2.2.7 Enrichment analysis with brain receptor maps

To perform the enrichment analysis, brain receptor maps, described in detail in Hansen et al., 2022, were used [59]. In this study, a comprehensive cortical profile of neurotransmitter receptor densities was constructed by assembling PET images of a total of 19 different neurotransmitter receptors, receptors, transporters and receptor binding sites, across 9 different neurotransmitter systems, including dopamine, norepinephrine, serotonin, acetylcholine, glutamate, GABA, histamine, cannabinoids and opioids, see fig. 2.14.

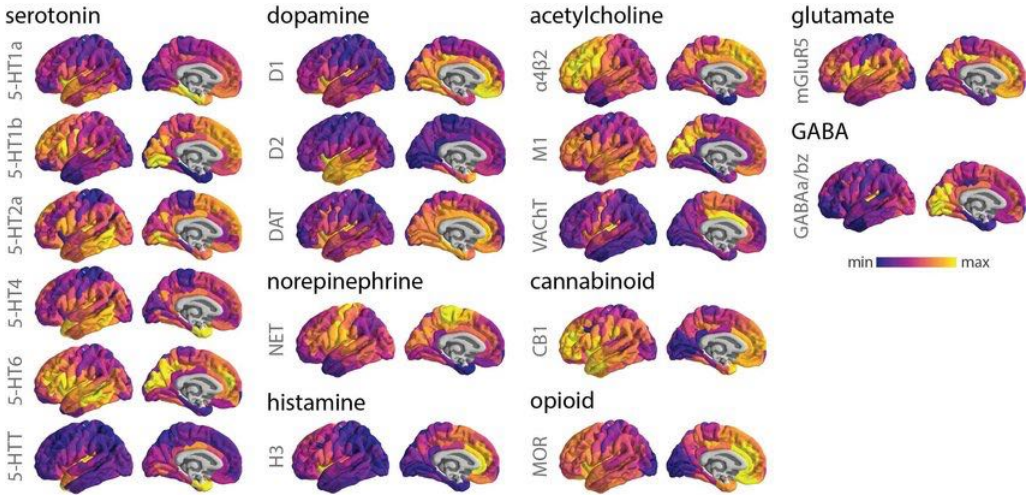


**Figure 2.14:** PET tracer images were collated and averaged to produce mean receptor distribution maps of 19 different neurotransmitter receptors and transporters across 9 different neurotransmitter systems and a combined total of over 1 200 healthy participants [59].

In this thesis, maps of the N-methyl-D-aspartate receptor (NMDAR), the brain protein synthesis rate (rCPS) [60], the group 1 metabotropic glutamate receptor 5 (mGluR5) and the GABA-A receptor were used.
In particular:

- the NMDA receptor is an ion channel receptor present at most excitatory synapses, where it responds to the neurotransmitter glutamate (the main excitatory neurotransmitter in the Central Nervous System);
- mGluR5 is a glutamate receptor and has been implicated in the neuropathology of various disorders, including autism, fragile X syndrome, attention deficit/hyperactivity disorder and schizophrenia;
- The GABA-A receptor (ionotropic receptor) is one of two receptors for GABA ($\gamma$-aminobutyric acid) that are present in the nervous system. GABA is the main inhibitory transmitter in the CNS and has many opposite ef-

fects to those of glutamate, some of which involve GABAergic inhibition of glutamate function.

The correspondence of metabolic PET connectivity graph metrics (both time-series and subject-series connectivity matrices were sparsified with a threshold at the $80^{th}$ percentile) with neurochemical architecture (neuroreceptor map templates) was assessed by means of Pearson correlation.

In addition, for each MC matrix (both time-series and subject-series connectivity matrices), hub nodes were identified. In this case, in order to have a credible statistic, approximately 20 hubs were taken into account; this was done by taking the top 35% (instead of 20% as described before) of both degree and eigenvector centrality distributions. In order to assess the presence of statistically significant differences in receptor density between hub and non-hub nodes, the Wilcoxon ranksum statistical test was applied to the two groups.

### 2.2.8 Estimation of metabolic connectivity at voxel level

The voxel dynamics of GM, WM and CSF were interpolated with a uniform 5 s step grid. However, also in this case, the dynamics of the voxels for the first few minutes are very noisy and different pre-processing approaches were tested:

- moving average filter with window of 5, on the first 20 min;
- moving average filter with window of 11, on the first 20 min;
- average 6 to 6 on 5 s frames, 3 to 3 on 20 s frames, 2 to 2 on 60 s frames;
- linear polynomial fit on the first 20 min;
- quadratic polynomial fit over the first 20 min;
- average 6 to 6 on 5 s frames;
- average 3 to 3 on 5s frames.

For all these approaches, the five standardisations set out above were tested, and for the first three, both a global normalisation (i.e. normalising on all voxels considered, thus grey, white and cerebrospinal fluid voxels) and a normalisation on grey matter voxels only were attempted.

Independent component analysis (ICA) was used to extract voxel-level metabolic

connectivity information from dynamic PET data, via the Group ICA of the fMRI Toolbox (GIFT). This is a MATLAB toolbox that implements several algorithms for independent component analysis and blind source separation of group (and single-subject) functional MRI data. The idea is therefore to adapt this toolbox, generally used for fMRI data, to PET data, as previously attempted [36, 39].

However, before applying ICA, a preliminary step was carried out in order to understand which pre-processing method could give the most satisfactory results: k-means clustering was applied to the voxel dynamics (obtained with the different combinations of data denoising and normalisation).
Distance metrics play a very important role in the clustering process, and were attempted here:

- Euclidean distance squared: each centroid is the average of the points in that cluster.

$$d(x, c) = (x - c)(x - c') \tag{2.20}$$

  where $x$ is an observation and $c$ is a centroid.

- Cosine: one minus the cosine of the included angle between points (treated as vectors). Each centroid is the mean of the points in that cluster, after normalizing those points to unit Euclidean length.

$$d(x, c) = 1 - \frac{xc'}{\sqrt{(xx')(cc')}} \tag{2.21}$$

- Correlation: one minus the sample correlation between points (treated as sequences of values). Each centroid is the component-wise mean of the points in that cluster, after centering and normalizing those points to zero mean and unit standard deviation.

$$d(x, c) = 1 - \frac{(x - \vec{x})(c - \vec{c})}{\sqrt{(x - \vec{x})(x - \vec{x})'}\sqrt{(c - \vec{c})(c - \vec{c})}} \tag{2.22}$$

  where:
  $\vec{x} = \frac{1}{p}(\sum_{j=1}^{p} x_j)\vec{1_p}$

  $\vec{c} = \frac{1}{p}(\sum_{j=1}^{p} c_j)\vec{1_p}$

  $\vec{1_p}$ is a row vector of $p$ ones

The number of clusters was set at 10 and the number of replications (i.e. number of times to repeat clustering using new initial cluster centroid positions) at 200.

Following this preliminary step, it was proceeded with the ICA to be applied to the PET 4D dynamics.
For the application of ICA, several parameters had to be choosen, in particular: repetition time (TR) in seconds, number of independent components, ICA algorithm, type of data pre-processing, type of group ICA, type of back reconstruction, stability analysis type and z-score conversion.
In particular:

- TR=5 s, i.e. equal to the interpolation step;
- Number of independent components: 10, 15 and 20 were tested;
- ICA algorithm: the toolbox offers the possibility of testing number of estimation algorithms (Infomax, FastICA, EBM, SDD ICA, RADICAL, Amuse, EVD, COMBI, ERBM, Sparse-EBM, JADE, SIMBEC, ERICA, OPAC, Semi-blind Infomax, Constained ICA);
- Data pre-processing type: it is possible to choose between removing mean per timepoint, removing mean per voxel, intensity normalisation and variance normalisation;
- Group ICA type: temporal and spatial, here spatial ICA is performed;
- Back reconstruction type: GICA (choosen), spatial-temporal regression, regular (GICA2) and GICA3;
- Stability snalysis type: the options are regular, MST and ICASSO, the latter is the one chosen.

### Independent component analysis

ICA is a statistical technique whose aim is to separate a multivariate signal into its additive sub-components, then recover the underlying sources from an observed mixture of these sources [61].
The assumption is of linear mixture and statistically independent, non-Gaussian sources.

The observed signal in a given voxel is described as the sum of the contribu-

tions of all independent sources in the dataset.
Assuming $M$ zero mean sources $s_1, s_2, ..., s_M$, N linear combinations of these sources are observed. The j-th observed variable can be written as:

$$x_j = a_{j1}s_1 + a_{j2}s_2 + ... + a_{ji}s_i \qquad \text{with} \qquad \text{i=1,...,M} \qquad \text{j=1,...,N} \tag{2.23}$$

that in matrix format:

$$X = AS \tag{2.24}$$

where $X$ is the mixiture (observed data), $A$ is the unknown square mixing matrix ($N \times M$) which has to be estimated and $S$ represents the unknown source signals to be recovered. This is representing the generative linear instantaneous noise-free mixing ICA model.
The aim is to estimate an unmixing matrix $W$, so that $C = WX$ is an approximation of the true sources $S$. $W$ can be defined as a weight matrix which allows to project the original space $X$ into a new space that characterized the sources $S$.
A pre-processing procedures is generally performed in order to reduce the complexity of the problem. The first step is called *centering*, that aims in subtracting the mean value of $X$, $m = E[X]$, since it doesn't bring any useful information on the signal variance. As a consequence $X$ is a zero mean variable and $C$ as well. The mean values will be reintroduced once the mixing matrix $A$ has been computed, by adding to the estimate of $C$ its mean value given by $A^{-1}m$.
The second important step is the *whitening* or *sphering*. The aim is to whiten the observed variables, obtaining uncorrelated data with unity variances, this allows narrow the search of $A$ to orthogonal matrices.
Then, a $V$ matrix has to be identified, so that:

$$Z = VX \qquad \text{with} \qquad E[ZZ^T] = 1 = I \tag{2.25}$$

Define P as a symmetric and square matrix:

$$P = E[XX^T] = 1 = I \tag{2.26}$$

and

$$V = P^{-\frac{1}{2}} \tag{2.27}$$

and substituting:

$$E[ZZ^T] = I = E[VXX^TV^T] = P^{-\frac{1}{2}}PP^{-\frac{1}{2}} \tag{2.28}$$

After that the result is:

$$Z = VX = VAS = \widetilde{A}S \tag{2.29}$$

Where $\widetilde{A} = VA$ is the new mixing matrix and it is orthogonal ($\widetilde{A}\widetilde{A^T} = I$). Once $\widetilde{A}$ is estimated, the sources can be computed as $S = \widetilde{A^T}Z$. In particular the i-th independent source/component is computed as: $s_i = (\widetilde{a_i})^T z$.
Considering the equation 2.29, this is a linear combination of independent components and this sum is "more gaussian" than original components (sources). In fact under the hypotesis of non-gaussianity of sources, thanks to Central Limit Theory, the mixture given by the linear combination of sources will have a probability distribution surely more gaussian than that of sources. For this reason $\widetilde{A}$ has to be chosen in order to maximize the non-gaussianity of $S = \widetilde{A}Z$.
To measure the non-gaussianity, it is possible to use several indices, such as Kurtosis index, mutual information and negentropy.
The first one measures the dispersion of a statistical distribution around its mean value, and for a general aleatory variable $y$ is classically defined by:

$$Kurt(y) = E[y^4] - 3(E[y^2])^2 \tag{2.30}$$

This is null for gaussian variables, so $Kurt(y)$ has to be maximized.
Regarding the negentropy, this is based on entropy variation, in order to be null for gaussian variables and not negative in the other cases:

$$J(y) = H(y_{gauss}) - H(y) \tag{2.31}$$

where $H(\cdot)$ is the entropy and $y_{gauss}$ is a gaussian variable. Also in this case the aim is to maximize $J(y)$. This is the index used in many algorithm, such as FastICA.
Another index is the mutual information which measures the grade of statistic dependence between random variables and has to be minimized:

$$I(y_1, ..., y_M) = \sum_i H(y_i) - H(\mathbf{y}) \tag{2.32}$$

where **y** is a joint variable. It is a non-negative equation and it is null in case of independent variables because the second term overlaps with the first one. Therefore the mutual information has to be minimize in order to maximize the non-gaussianity of sources.

It is possible to carry out a spatial ICA (sICA) when it is assumed that sources are statistically independent in space, or temporal ICA (tICA) in which sources are assumed to be statistically independent in time, see fig. 2.15.

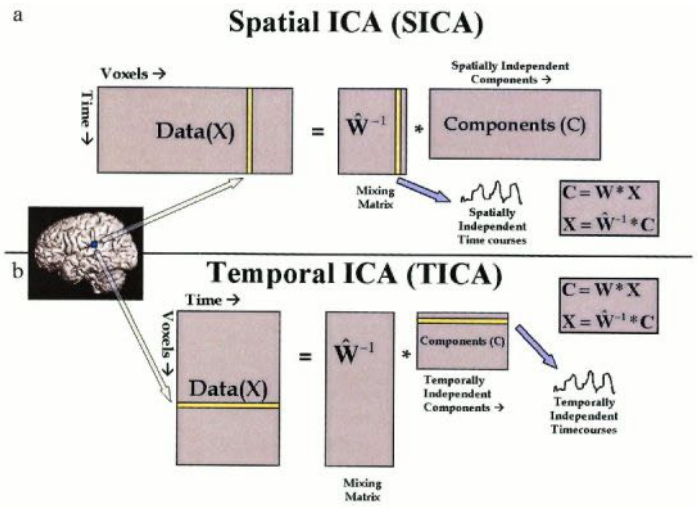


**Figure 2.15:** In the case of spatial ICA, the algorithm attempts to find spatially independent components with associated time courses. In the case of temporal ICA, the algorithm attempts to find temporally independent time courses with associated spatial maps [62].

The sICA decomposition can be described as $C = \widehat{W}X$, where $X$ is a $N \times N_V$ matrix, with $N$ is the number of time points, $N_V$ the number of voxels. $C$ is a $M \times N_V$ matrix, that contains the $M$ independent components. $\widehat{W}$ is the $M \times N$ estimated unmixing matrix found using ICA. The starting data can then be written as $X = \widehat{W^{-1}}C$, where the spatially independent components are located in the rows of $C$ and the associated spatially independent time courses are in the columns of $\widehat{W^{-1}}$ [62].

In the tICA the dimensions of $X$ original data matrix are reversed so that the rows of $C$ represent the temporally independent timecourses and the associated temporally independent maps are in the columns of $\widehat{W^{-1}}$.

### ICASSO

One problem with ICA algorithms is that they are stochastic, so the results can have slight changes in different runs of the algorithm. The algorithms in fact use the basic principle of starting from an initial point and then finding a local minimum of the cost function. As a consequence, depending on the initial point, the algorithm will find different local minima, so it is reasonable to run the estimation algorithm many times, using different initial points and evaluating which components are found in almost every run: this has been implemented in ICASSO.
It is a software package developed by Himberg et al. [63] with the goal of studying ICA reliability analysis. The independent components are estimated after running the chosen ICA algorithm several times and visualizing their clustering in the signal space. Each estimated independent component is a point in the signal space. If an independent component is reliable, ideally each run of the algorithm should produce a point in signal space very close to the actual component. Thus, reliable independent components correspond to clusters that are small and well separated from the rest of the estimates, while unreliable components correspond to points that do not belong to any cluster.
The steps of ICASSO are as follows:

1. Selection of the parameters of the estimation algorithm. If FastICA was selected for example, the orthogonalization approach (symmetric or deflationary) and nonlinearity will be chosen.

2. This algorithm is iterated a number of times. At each iteration the data is resampled by bootstrapping and/or the algorithm starts from a new random initial condition.

3. The estimated components are clustered according to their similarities to each other. Agglomerative clustering with the average linkage criterion is selected by default.

4. The clustering result is displayed as a 2D graph (2D Canonical Correlation Analysis, CCA, projection) from which it is possible to analyze how the estimates are concentrated in the clusters providing information on the quality of the estimate. In particular, if the cluster is compact and tight it emerges that the component estimate is similar despite randomization.

To direct the user's attention to clusters that seem most compact and interesting, a cluster quality index $I_q$ is generated in the third step, reflecting the compactness and isolation of a cluster. It is calculated as the difference between the average intra-cluster similarities and the average inter-cluster similarities:

$$I_q(C_m) = \frac{1}{(|C_m|)^2} \sum_{i,j \in C_m} \sigma_{ij} - \frac{1}{|C_m|\,|C_{-m}|} \sum_{i \in C_m} \sum_{j \in C_{-m}} \sigma_{ij}\sigma_{ij} \tag{2.33}$$

where $C$ represents the indices set of all the estimated components, $C_m$ and $C_{-m}$ are respectively the set of indices belonging and not belonging to the m-th cluster and $|C_m|$ is size of the m-th cluster.

# Chapter 3

# Results

## 3.1 Estimation of metabolic connectivity matrices at parcel level: parcellation with Hammers atlas

Once the parcellation with Hammers anatomical atlas has been executed, a count of the voxels in each parcel was performed.
Parcels of very small size (few voxels per region) or from WM and CSF areas were removed and not considered in the subsequent analysis. These are: Brainstem, Corpus Callosum, Substantia Nigra (right and left), Frontal Horn (right and left), Temporal Horn (right and left), see table 3.1.

Therefore, for each of the 71 subjects a matrix $X \in R^{p \times T}$ is obtained, where $p$

**Table 3.1:** Parcels to remove, with voxels count

| Parcels | voxel count (pre-segm.) | voxel count (post-segm.) |
|---|---|---|
| Brainstem | 290 | 214 |
| Corpus Callosum | 145 | 119 |
| Substantia Nigra (right) | 1 | 1 |
| Substantia Nigra (left) | 2 | 1 |
| Frontal Horn (right) | 116 | 76 |
| Frontal Horn (left) | 118 | 84 |
| Temporal Horn (right) | 38 | 35 |
| Temporal Horn (left) | 38 | 32 |

is the number of parcels (74, equals to 84 Hammers parcels from which the 9 described above are removed) and T is the size of the new time grid.
The TACs of the 74 parcels considered, for a representative subject, are shown in the figure 3.1.

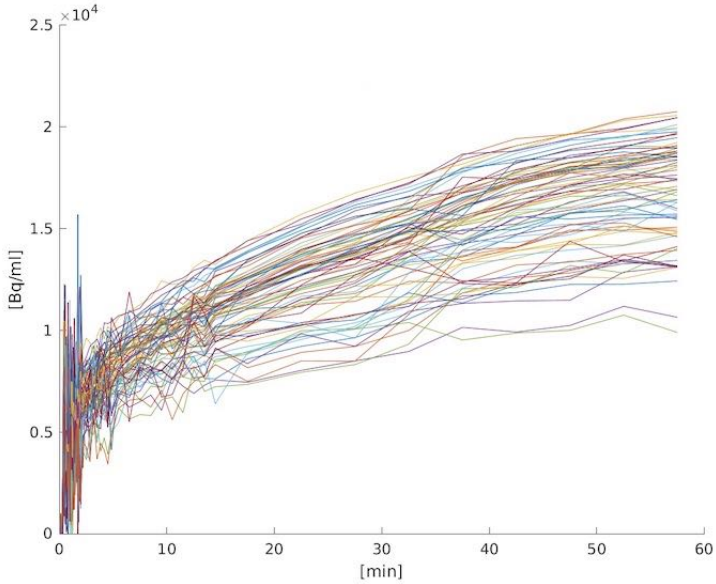


**Figure 3.1:** Time Activity Curves of the 74 parcels for a representative subject (parcellation with Hammers Anatomical Atlas).

### 3.1.1 Data denoising

Among the approaches tested for the data denoising it was chosen to proceed with the moving average filter with a window size of 5 and the 3 by 3 average of the first 24 frames, see fig. 3.2. In order to choose the best approach, the TAC of a region (e.g. Anterior temporal lobe, medial part) obtained with the two data denosing methodologies was compared with the original one (without any processing), see fig. 3.3. It can be observed that in both cases there is a noise reduction in the initial part of the curve but the moving average filter results in an excessive lowering of the beginning, whereas the 3 by 3 average better respects the statistics of the process by maintaining a more physiological trend. It was therefore decided to proceed with this methodology.

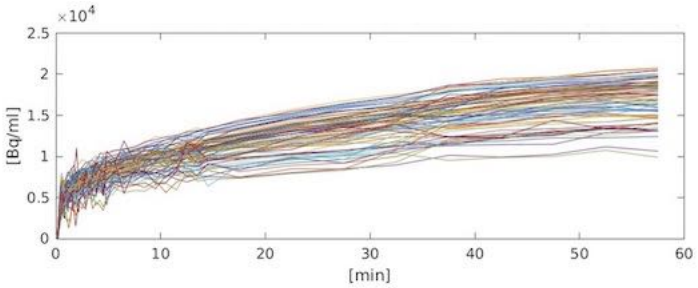


**(a)** *TACs pre-processed with a moving average filter with a window size of 5 on the first 24 frames*

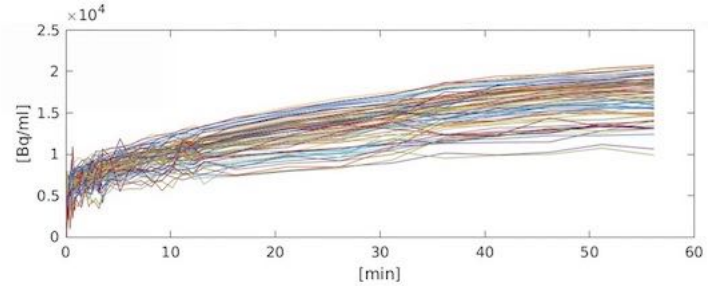


**(b)** *TACs pre-processed with 3 by 3 average of the first 24 frames*

**Figure 3.2:** TACs of the 74 parcels, pre-processed in two possible way. The first figure (a) is the case of moving average filter with window size of 5 (first 24 frames). The second figure (b) is the case of 3 by 3 average (first 24 frames)

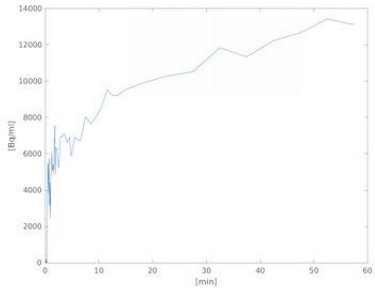

**(a)** *TAC of Anterior temporal lobe, medial part, without any processing*

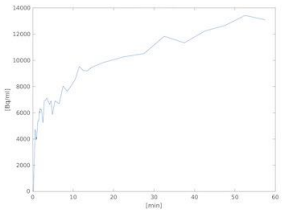

**(b)** *TAC of Anterior temporal lobe, medial part, pre-processed with a moving average filter with a window size of 5 on the first 24 frames*

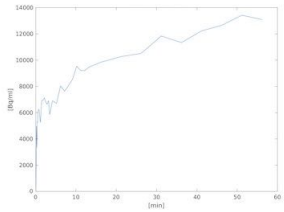

**(c)** *TAC of Anterior temporal lobe, medial part, pre-processed with 3 by 3 average of the first 24 frames*

**Figure 3.3:** TAC of Anterior temporal lobe, medial part. (a) Without any pre-processing. (b) Moving average filter. (c) 3 by 3 average of the first 24 frames.

### 3.1.2 Similarity-based approach

The average time-series connectivity matrices across subjects for each metric (Pearson's correlation, fig. 3.4; Cosine Similarity, fig. 3.5; Gaussian Kernel, fig. 3.6; Euclidean Similarity, fig. 3.7) and normalisation are reported below, considering the full TAC. Since there is no gold standard, non-trivial differences in MC networks emerge with the different standardisation methods.

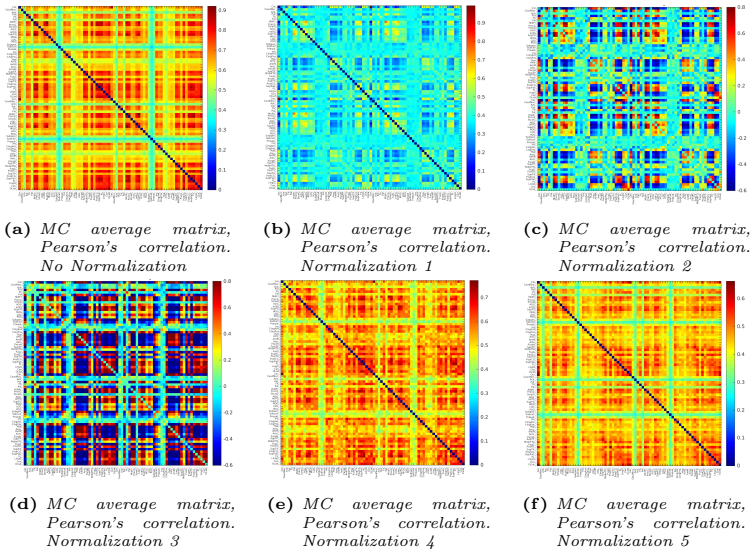

**(a)** *MC average matrix, Pearson's correlation. No Normalization*

**(b)** *MC average matrix, Pearson's correlation. Normalization 1*

**(c)** *MC average matrix, Pearson's correlation. Normalization 2*

**(d)** *MC average matrix, Pearson's correlation. Normalization 3*

**(e)** *MC average matrix, Pearson's correlation. Normalization 4*

**(f)** *MC average matrix, Pearson's correlation. Normalization 5*

**Figure 3.4:** Time-series connectivity average matrices (full TAC), Pearson's correlation.

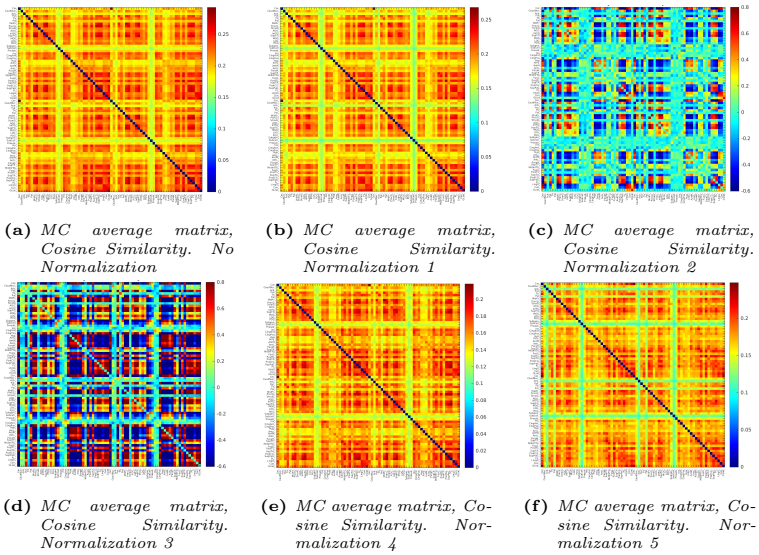

**(a)** *MC average matrix, Cosine Similarity. No Normalization*

**(b)** *MC average matrix, Cosine Similarity. Normalization 1*

**(c)** *MC average matrix, Cosine Similarity. Normalization 2*

**(d)** *MC average matrix, Cosine Similarity. Normalization 3*

**(e)** *MC average matrix, Cosine Similarity. Normalization 4*

**(f)** *MC average matrix, Cosine Similarity. Normalization 5*

**Figure 3.5:** Time-series connectivity average matrices (full TAC), Cosine Similarity.

For the matrices shown here, the order of the labels is such that first the left and then the right hemisphere is reported, and in each first the subcortical regions,

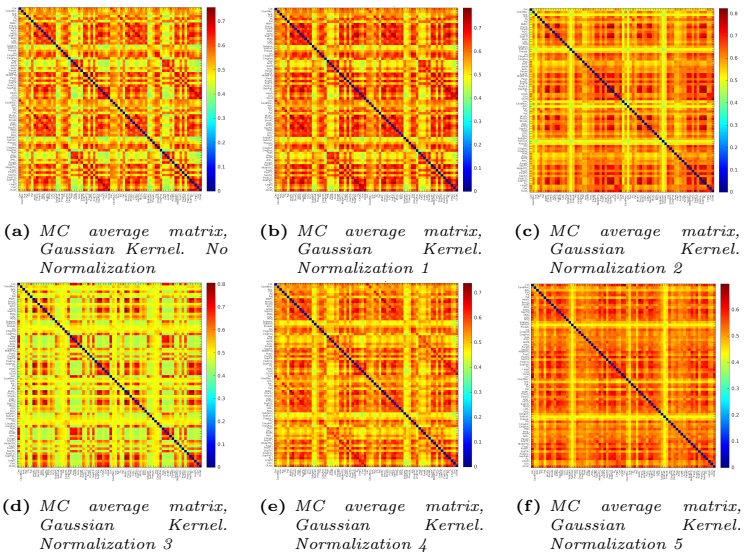

**(a)** *MC average matrix, Gaussian Kernel. No Normalization*

**(b)** *MC average matrix, Gaussian Kernel. Normalization 1*

**(c)** *MC average matrix, Gaussian Kernel. Normalization 2*

**(d)** *MC average matrix, Gaussian Kernel. Normalization 3*

**(e)** *MC average matrix, Gaussian Kernel. Normalization 4*

**(f)** *MC average matrix, Gaussian Kernel. Normalization 5*

**Figure 3.6:** Time-series connectivity average matrices (full TAC), Gaussian Kernel.

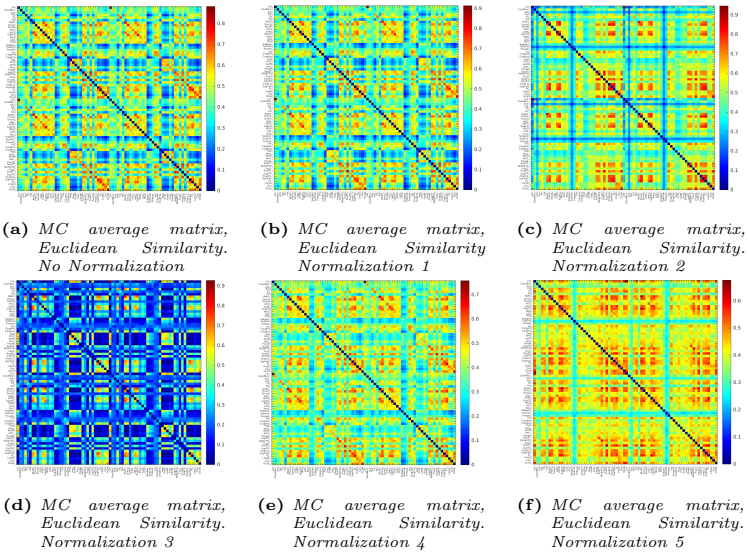

**(a)** *MC average matrix, Euclidean Similarity. No Normalization*

**(b)** *MC average matrix, Euclidean Similarity Normalization 1*

**(c)** *MC average matrix, Euclidean Similarity. Normalization 2*

**(d)** *MC average matrix, Euclidean Similarity. Normalization 3*

**(e)** *MC average matrix, Euclidean Similarity. Normalization 4*

**(f)** *MC average matrix, Euclidean Similarity. Normalization 5*

**Figure 3.7:** Time-series connectivity average matrices (full TAC), Euclidean Similarity.

then Frontal Lobe, Temporal Lobe, Parietal Lobe, Occipital Lobe, Insula and Cingulate Gyri.

A Fisher's Z-transformation is applied, as the metrices result in very squashed upward values, with a subsequent rescaling between [0;1], for the following cases:

- Gaussian kernel (for each standardisation);
- Euclidean Distance (for each normalisation);
- Pearson correlation (for the non-standardised case, normalisation 1, 4 and

5);

- Cosine similarity (for the non-standardised case, normalisation 1, 4 and 5).

Evaluating all possible combinations of metrics and standardisation, it was found that, through the use of Euclidean similarity as a metric and even without the application of any kind of normalisation (see fig. 3.8), it is possible to reveal a Network structure, i.e. with interhemispheric homotopic connections (right hemisphere - left hemisphere) that are clearly distinguishable, as it is expected from studies of brain connectivity. The matrix is then shown in sparsified form, thus applying a threshold at the $80^{th}$ percentile, keeping 20% of the connections.

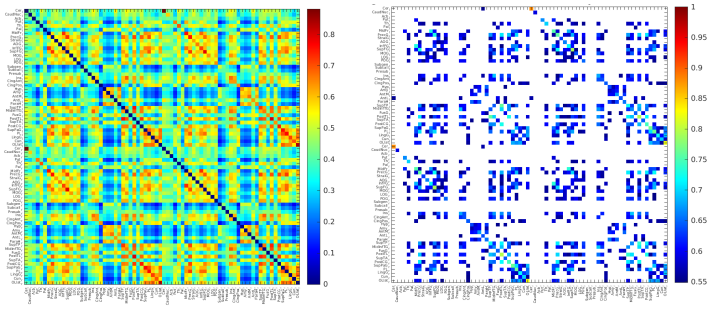

**(a)** *MC average matrix obtained by Euclidean similarity metric (non-normalised case and with Fisher's Z-transformation).*

**(b)** *MC average sparse matrix obtained by Euclidean similarity metric (non-normalised case and with Fisher's Z-transformation).*

**Figure 3.8:** MC average matrix, Euclidean Similarity, non-normalized. (a) Full average matrix. (b) Sparse average matrix.

Once the most suitable estimation approaches had been identified, metabolic connectivity matrices were obtained not only by considering the full TAC of each parcel, as reported above, but by taking into account: the first 10 minutes (see fig. 3.9), the first 20 minutes (see fig. 3.10) and the last 20 minutes (see fig. 3.11).

It was then decided to keep the case of the first 10 minutes of the TAC as more representative of the initial portion of the curve instead of the first 20 minutes.

The metabolic connectivity time-series matrices obtained by considering the time series of compartment 1 (see fig. 3.12) and the time series of compartment 2 are then reported (see fig. 3.13).

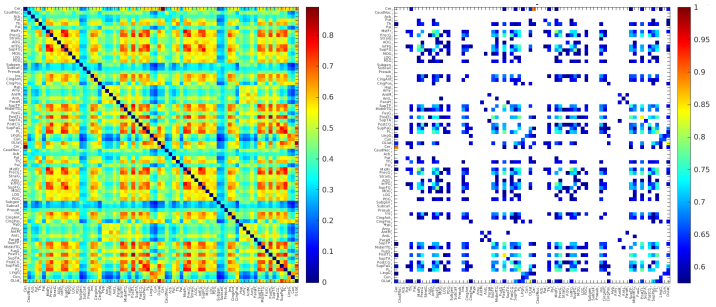

**(a)** *MC average full matrix, first 10 minutes of the TAC (Euclidean Similarity, non-normalized)*

**(b)** *MC average sparse matrix, first 10 minutes of the TAC (Euclidean Similarity, non-normalized)*

**Figure 3.9:** MC average matrix, first 10 minutes of the TAC (Euclidean Similarity, non-normalized)

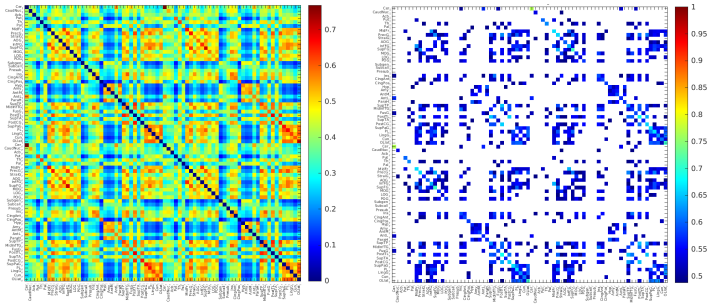

**(a)** *MC average full matrix, first 20 minutes of the TAC (Euclidean Similarity, non-normalized)*

**(b)** *MC average sparse matrix, first 20 minutes of the TAC (Euclidean Similarity, non-normalized)*

**Figure 3.10:** MC average matrix, first 20 minutes of the TAC (Euclidean Similarity, non-normalized)

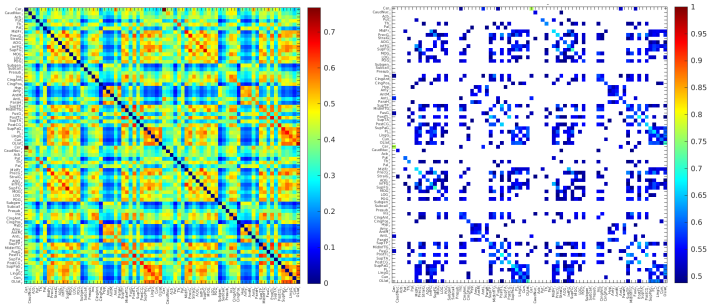

**(a)** *MC average full matrix, last 20 minutes of the TAC (Euclidean Similarity, non-normalized)*

**(b)** *MC average sparse matrix, last 20 minutes of the TAC (Euclidean Similarity, non-normalized)*

**Figure 3.11:** MC average matrix, last 20 minutes of the TAC (Euclidean Similarity, non-normalized)

### 3.1.3 MC subject-series

The subject-series connectivity matrices of $K_1$, $k_3$, $K_i$ and $SUVR$ are reported in fig. 3.14.

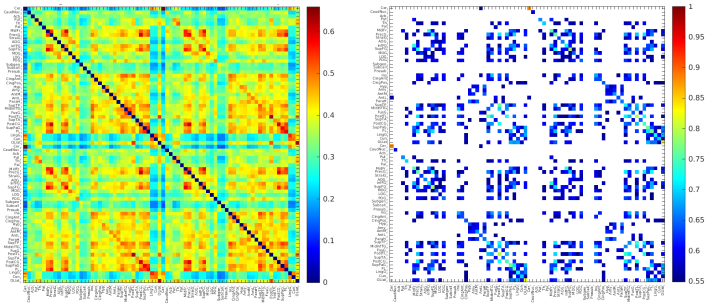

**(a)** *MC average full matrix, Compartment 1 (Euclidean Similarity, non-normalized)*

**(b)** *MC average sparse matrix, Compartment 1 (Euclidean Similarity, non-normalized)*

**Figure 3.12:** MC average matrix, Compartment 1 (Euclidean Similarity, non-normalized)

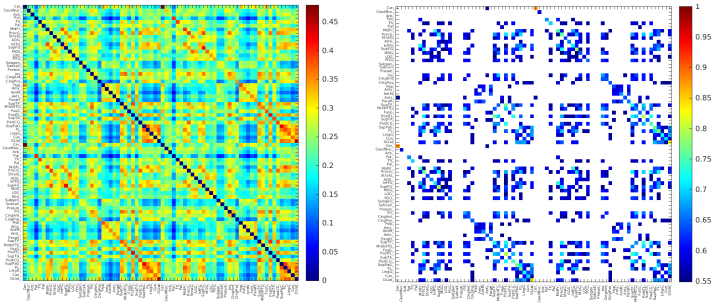

**(a)** *MC average full matrix, Compartment 2 (Euclidean Similarity, non-normalized)*

**(b)** *MC average sparse matrix, Compartment 2 (Euclidean Similarity, non-normalized)*

**Figure 3.13:** MC average matrix, Compartment 2 (Euclidean Similarity, non-normalized)

### 3.1.4 Across-subject and across-method reproducibility

In order to assess the reproducibility between the various metrics and normalisations, Dice's pairwise similarity coefficients were calculated by binarising the average metabolic connectivity matrices obtained from the full TAC, with a threshold at the $80^{th}$ percentile, see fig. 3.15.
Maximum similarity can be found between Euclidean Similarity and Gaussian Kernel metrics, the choice of one or the other is therefore almost equivalent.

To assess the across-subject reproducibility of the metrics and normalisations, the full matrices of the coefficients of variation (CV) are reported together with *median* $CV\% \pm MAD$ (MC obtained considering the full TAC).

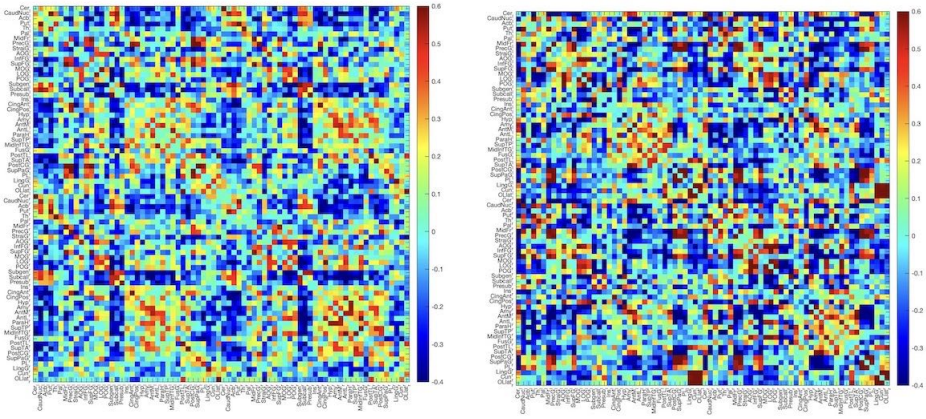

**(a)** *MC matrix of* $K_1$ **(b)** *MC matrix of* $k_3$

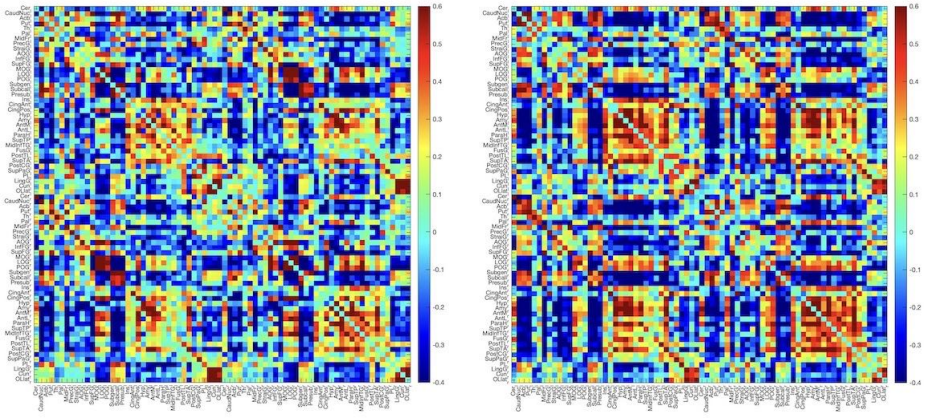

**(c)** *MC matrix of* $K_i$ **(d)** *MC matrix of SUVR*

**Figure 3.14:** MC matrices subject-series, obtained via Pearson's correlation across-subject.

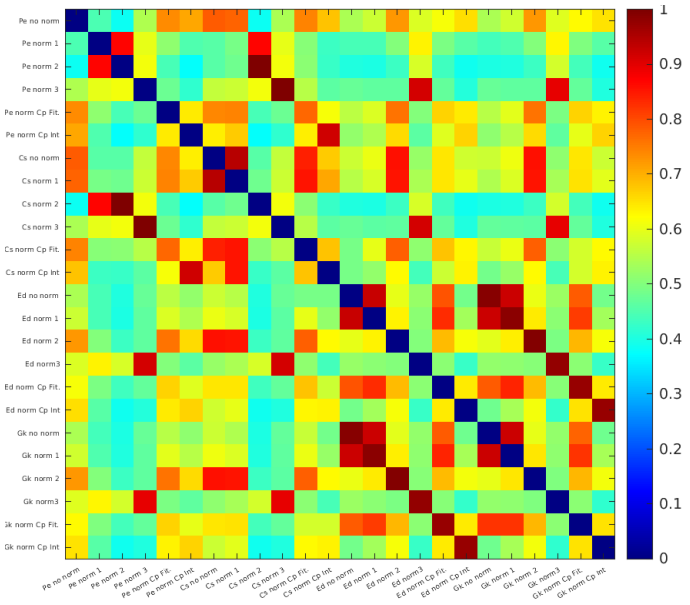


**Figure 3.15:** Across-metrics and normalizations reproducibility (full TAC).

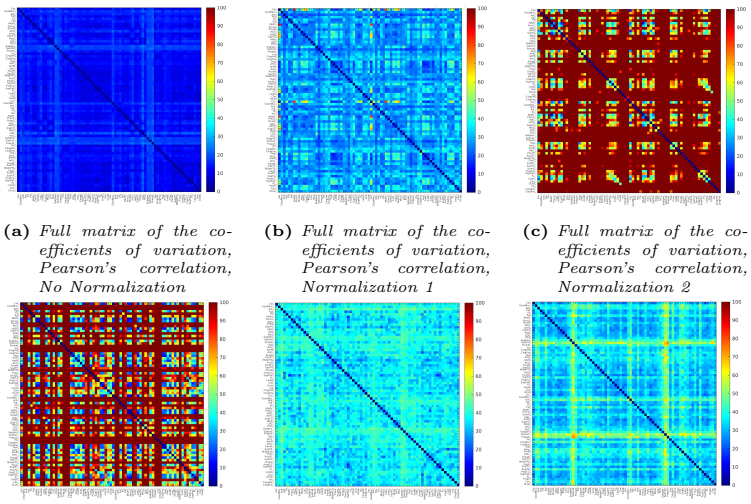

**(a)** *Full matrix of the coefficients of variation, Pearson's correlation, No Normalization*

**(b)** *Full matrix of the coefficients of variation, Pearson's correlation, Normalization 1*

**(c)** *Full matrix of the coefficients of variation, Pearson's correlation, Normalization 2*

**(d)** *Full matrix of the coefficients of variation, Pearson's correlation, Normalization 3*

**(e)** *Full matrix of the coefficients of variation, Pearson's correlation, Normalization 4*

**(f)** *Full matrix of the coefficients of variation, Pearson's correlation, Normalization 5*

**Figure 3.16:** Full matrices of the coefficients of variation (the scale is set from 0 to 100%), Pearson's correlation.

**Table 3.2:** $median CV\% \pm MAD$ (Pearson's correlation)

| Normalization | $median\ CV\% \pm MAD$ |
|---|---|
| No Normalization | $12,6 \pm 2,7$ |
| Normalization 1 | $32,7 \pm 5,4$ |
| Normalization 2 | $194,6 \pm 1620,2$ |
| Normalization 3 | $109,2 \pm 986,5$ |
| Normalization 4 | $45,8 \pm 4,4$ |
| Normalization 5 | $65,7 \pm 8,9$ |

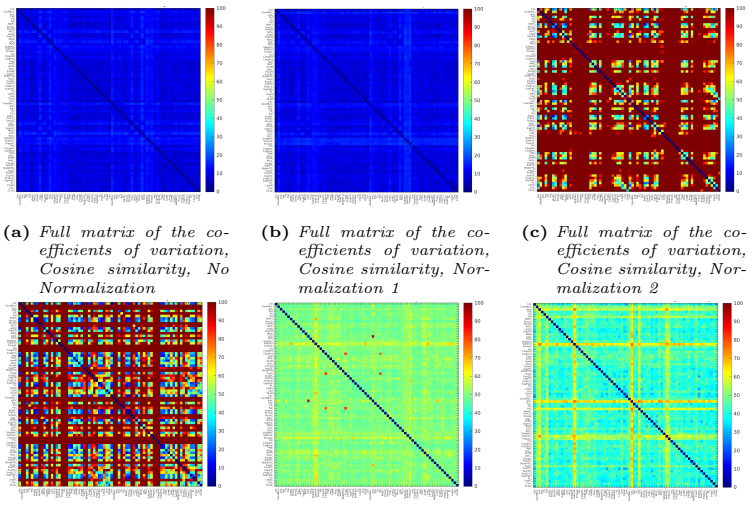

**(a)** *Full matrix of the coefficients of variation, Cosine similarity, No Normalization*

**(b)** *Full matrix of the coefficients of variation, Cosine similarity, Normalization 1*

**(c)** *Full matrix of the coefficients of variation, Cosine similarity, Normalization 2*

**(d)** *Full matrix of the coefficients of variation, Cosine similarity, Normalization 3*

**(e)** *Full matrix of the coefficients of variation, Cosine similarity, Normalization 4*

**(f)** *Full matrix of the coefficients of variation, Cosine similarity, Normalization 5*

**Figure 3.17:** Full matrices of the coefficients of variation (the scale is set from 0 to 100%), Cosine similarity.

**Table 3.3:** $medianCV\% \pm MAD$ (Cosine Similarity)

| Normalization | $median\ CV\% \pm MAD$ |
|---|---|
| No Normalization | $10,2 \pm 1,9$ |
| Normalization 1 | $14,1 \pm 2,8$ |
| Normalization 2 | $194,6 \pm 1620,2$ |
| Normalization 3 | $109,2 \pm 986,5$ |
| Normalization 4 | $49,2 \pm 2,6$ |
| Normalization 5 | $73,7 \pm 9,3$ |

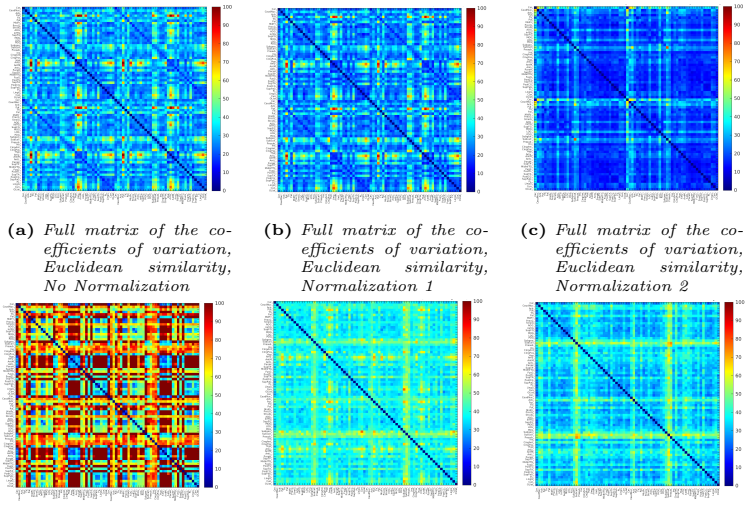

**(a)** *Full matrix of the coefficients of variation, Euclidean similarity, No Normalization*

**(b)** *Full matrix of the coefficients of variation, Euclidean similarity, Normalization 1*

**(c)** *Full matrix of the coefficients of variation, Euclidean similarity, Normalization 2*

**(d)** *Full matrix of the coefficients of variation, Euclidean similarity, Normalization 3*

**(e)** *Full matrix of the coefficients of variation, Euclidean similarity, Normalization 4*

**(f)** *Full matrix of the coefficients of variation, Euclidean similarity, Normalization 5*

**Figure 3.18:** Full matrices of the coefficients of variation (the scale is set from 0 to 100%), Euclidean similarity.

**Table 3.4:** $medianCV\% \pm MAD$ (Euclidean Similarity)

| Normalization | $median\ CV\% \pm MAD$ |
|---|---|
| No Normalization | $8,3 \pm 28,9$ |
| Normalization 1 | $7,5 \pm 26,8$ |
| Normalization 2 | $5,9 \pm 19,8$ |
| Normalization 3 | $37,3 \pm 68,9$ |
| Normalization 4 | $6,3 \pm 47,7$ |
| Normalization 5 | $8,1 \pm 41,3$ |

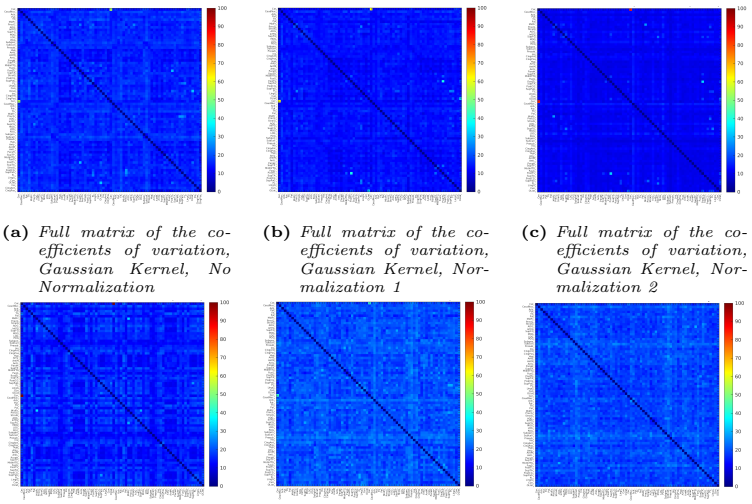

**(a)** *Full matrix of the coefficients of variation, Gaussian Kernel, No Normalization*

**(b)** *Full matrix of the coefficients of variation, Gaussian Kernel, Normalization 1*

**(c)** *Full matrix of the coefficients of variation, Gaussian Kernel, Normalization 2*

**(d)** *Full matrix of the coefficients of variation, Gaussian Kernel, Normalization 3*

**(e)** *Full matrix of the coefficients of variation, Gaussian Kernel, Normalization 4*

**(f)** *Full matrix of the coefficients of variation, Gaussian Kernel, Normalization 5*

**Figure 3.19:** Full matrices of the coefficients of variation (the scale is set from 0 to 100%), Gaussian Kernel.

**Table 3.5:** $median CV\% \pm MAD$ (Gaussian Kernel)

| Normalization | $median\ CV\% \pm MAD$ |
|---|---|
| No Normalization | $1,7 \pm 14,7$ |
| Normalization 1 | $1,4 \pm 15,1$ |
| Normalization 2 | $1,1 \pm 9,9$ |
| Normalization 3 | $19,9 \pm 88,6$ |
| Normalization 4 | $3,0 \pm 22,5$ |
| Normalization 5 | $2,6 \pm 23,9$ |

The analysis of the coefficients of variation also confirms the choice of the Euclidean Similarity metric to determine the metabolic connectivity matrices. In fact, it can be observed that the highest inter-subject reproducibility, and thus the lowest $median\ CV\% \pm MAD$, are for the Gaussian Kernel and Euclidean Distance metrics.

Therefore, the full matrices of the coefficients of variation of the MC matrices considering the first 10 minutes of the TAC, the last 20 minutes, the time series of compartment 1 and compartment 2, for the not normalised Euclidean Similarity case only, are reported in the figure 3.20. Also indicating the corresponding $median\ CV\% \pm MAD$ value.

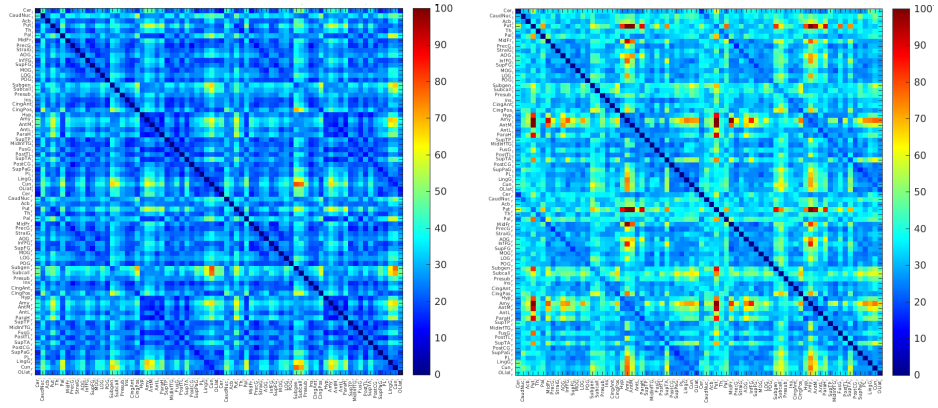

**(a)** *Full matrix of the coefficients of variation, Euclidean similarity, No Normalization, first 10 minutes.*

**(b)** *Full matrix of the coefficients of variation, Euclidean similarity, No Normalization, last 20 minutes.*

**(c)** *Full matrix of the coefficients of variation, Euclidean similarity, No Normalization, compartment 1*

**(d)** *Full matrix of the coefficients of variation, Euclidean similarity, No Normalization, compartment 2*

**Figure 3.20:** Full matrices of the coefficients of variation (the scale is set from 0 to 100%), by means of Euclidean similarity metrics and not normalised case.

**Table 3.6:** $medianCV\% \pm MAD$ (Euclidean Similarity, first 10 minutes)

| Normalization | $median\ CV\% \pm MAD$ |
|---|---|
| No Normalization | $26,4 \pm 7,1$ |
| Normalization 1 | $25,5 \pm 6,8$ |
| Normalization 2 | $19,2 \pm 6,3$ |
| Normalization 3 | $51,6 \pm 18,7$ |
| Normalization 4 | $39,3 \pm 5,0$ |
| Normalization 5 | $33,7 \pm 6,5$ |

**Table 3.7:** $median CV\% \pm MAD$ (Euclidean Similarity, last 20 minutes)

| Normalization | $median\ CV\% \pm MAD$ |
|---|---|
| No Normalization | $32,1 \pm 8,3$ |
| Normalization 1 | $32,1 \pm 8,3$ |
| Normalization 2 | $30,1 \pm 6,4$ |
| Normalization 3 | $53,0 \pm 12,2$ |
| Normalization 4 | $32,5 \pm 8,1$ |
| Normalization 5 | $32,5 \pm 8,0$ |

**Table 3.8:** $median CV\% \pm MAD$ (Euclidean Similarity, compartment 1)

| Normalization | $median\ CV\% \pm MAD$ |
|---|---|
| No Normalization | $38,9 \pm 7,9$ |
| Normalization 1 | $38,8 \pm 7,9$ |
| Normalization 2 | $36,6 \pm 5,6$ |
| Normalization 3 | $104,2 \pm 24,1$ |
| Normalization 4 | $42,3 \pm 7,5$ |
| Normalization 5 | $36,7 \pm 7,6$ |

**Table 3.9:** $median CV\% \pm MAD$ (Euclidean Similarity, compartment 2)

| Normalization | $median\ CV\% \pm MAD$ |
|---|---|
| No Normalization | $47,7 \pm 9,4$ |
| Normalization 1 | $45,9 \pm 9,3$ |
| Normalization 2 | $31,8 \pm 11,1$ |
| Normalization 3 | $102,0 \pm 72,8$ |
| Normalization 4 | $47,5 \pm 8,8$ |
| Normalization 5 | $46,4 \pm 8,8$ |

In order to assess the relationship between the different portions of the TAC (first 10 minutes, first 20 minutes, last 20 minutes), and with the time series of compartment 1 and compartment 2, the values of the Pearson's correlation coefficients is evaluated between all possible pairs of average MC time-series matrices obtained using the Euclidean similarity metrics, see fig. 3.21. These matrices were considered following an $80^{th}$ percentile sparsification.

After their binarisation, it was also possible to calculate Dice's pairwise similarity coefficient between all possible pairs of matrices.

In figure 3.22 we highlight the correlations considering only the non-normalised case of Euclidean Similarity, since this is the option chosen for the time-series metabolic connectivity matrices.

What is evident is that:

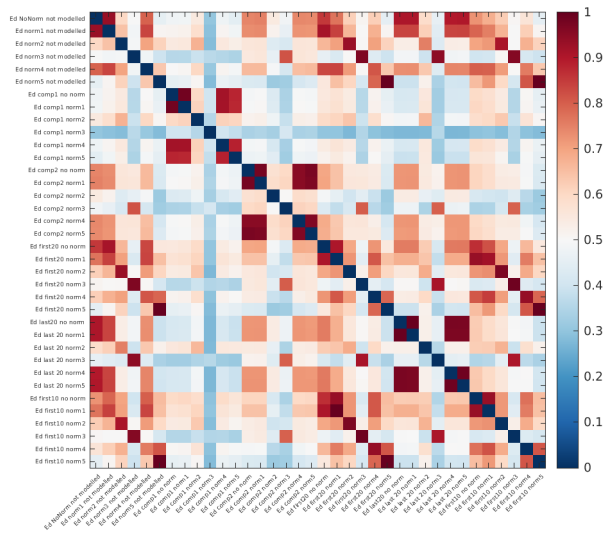

**Figure 3.21:** Pearson's correlation coefficients evaluated between all possible pairs of MC time-series matrices

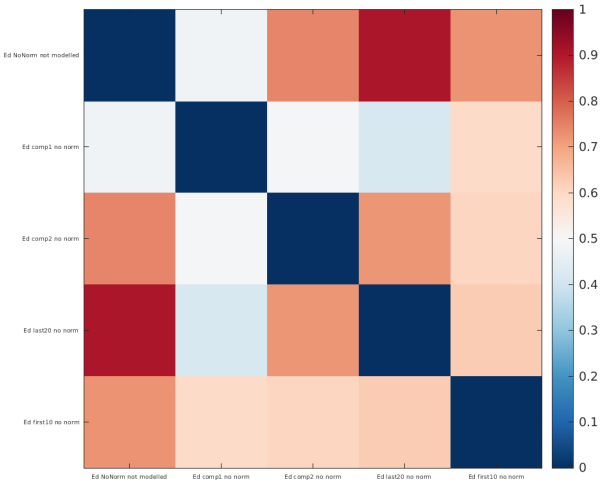


**Figure 3.22:** Pearson's correlation coefficients evaluated between the non-normalised case of Euclidean Similarity

- MC from full TAC is strongly correlated (correlation values around 0.9) with MC from the last 20 minutes of TAC and strongly-moderately correlated (values around 0.7) with MC from compartment 2 and from the first 10 minutes of TAC.

- MC from compartment 2 turns out to be strongly-moderately correlated (values around 0.7) also with MC from the last 20 minutes.

- MC from compartment 1 appears to be uncorrelated with all other metabolic connectivity matrices.

### 3.1.5 MC subject-series vs MC time-series

Matrices reporting the Pearson's correlation coefficients between the average MC time-series and subject-series matrices (see fig. 3.23), as well as Dice's coefficient of pairwise similarity (see fig. 3.24), are shown below.

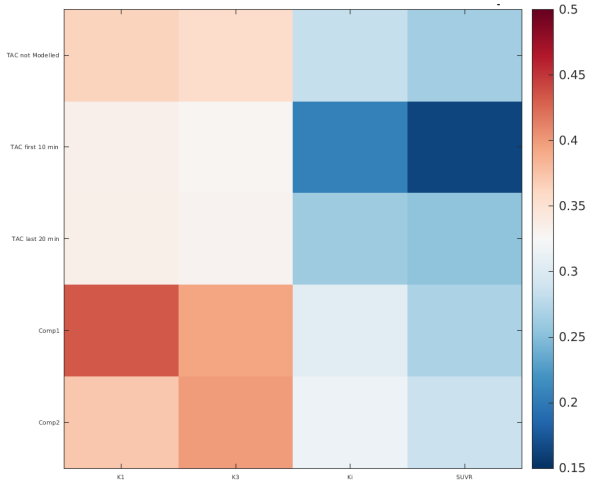


**Figure 3.23:** Pearson's correlation coefficients evaluated between MC time-series matrices and MC subject-series matrices. The correlation was performed between the entries of the vectorised matrices.

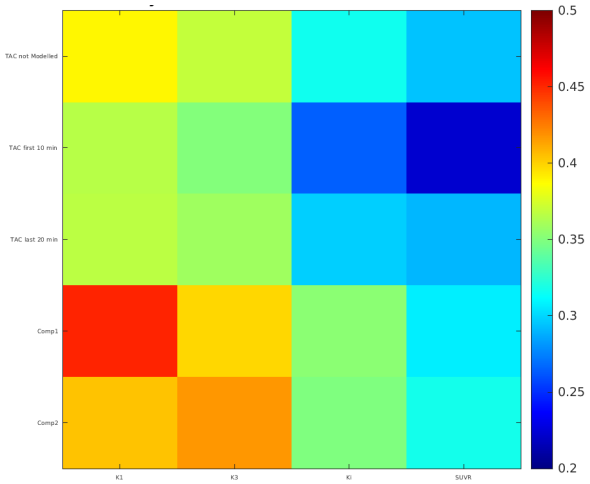


**Figure 3.24:** Dice's coefficient of pairwise similarity evaluated between all possible pairs of MC time-series matrices

What is evident is that:

- the strongest relationship (correlation values around 0.4) is between the matrix of $K_1$ and the matrix of compartment 1.
- Correlations around 0.4 also emerged between the matrix of compartment 2 and the matrix of $k_3$.

- $SUVR$ and $K_i$ are found to be uncorrelated with all other time-series matrices.

## 3.2 Graph theory metrics and hubs

The distribution, for each parcel, of degree and eigenvector centrality are reported on the Hammers atlas template, evaluated on the different metabolic connectivity average matrices: full TAC (fig. 3.25), first 10 minutes (fig. 3.26), last 20 minutes (fig. 3.27), compartment 1 (fig. 3.28) and compartment 2 (fig. 3.29). The colour scale used is "Hot", i.e. with increasing values from dark to light.

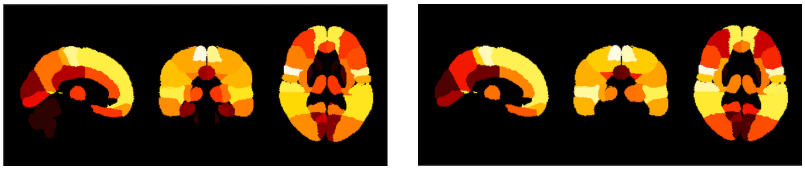

**(a)** *Degree distribution for each parcel (full TAC)]*

**(b)** *Eigenvector centrality distribution for each parcel (full TAC)*

**Figure 3.25:** Degree (a) and eigenvector centrality (b) distribution (full TAC)

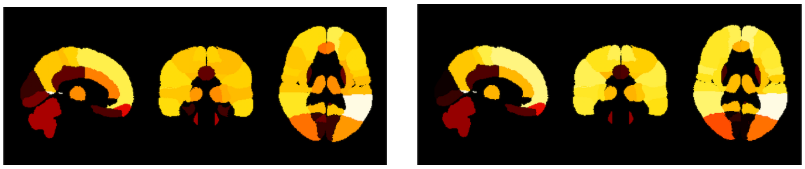

**(a)** *Degree distribution for each parcel (first 10 minutes TAC)]*

**(b)** *Eigenvector centrality distribution for each parcel (first 10 minutes TAC)*

**Figure 3.26:** Degree (a) and eigenvector centrality (b) distribution (first 10 minutes TAC)

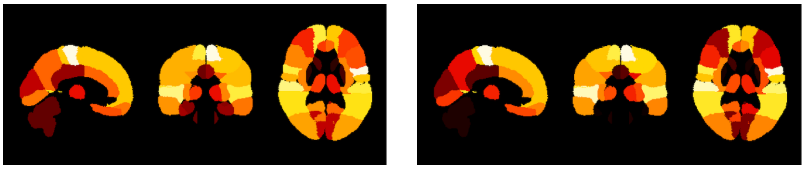

**(a)** *Degree distribution for each parcel (last 20 minutes TAC)]*

**(b)** *Eigenvector centrality distribution for each parcel (last 20 minutes TAC)*

**Figure 3.27:** Degree (a) and eigenvector centrality (b) distribution (last 20 minutes TAC)

What emerges is (considering the degree distribution, being consistent for eigenvector centrality):

- the distribution of the full TAC is particularly similar to that of the last 20 minutes, i.e. with high values for the temporal and occipital lobes.

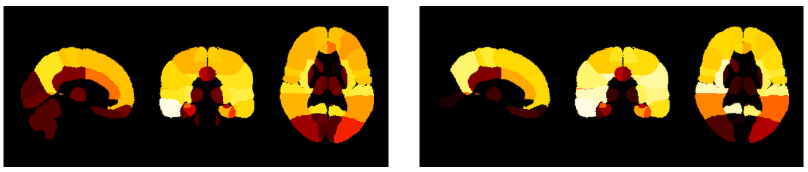

**(a)** *Degree distribution for each parcel (compartment 1)]*

**(b)** *Eigenvector centrality distribution for each parcel (compartment 1)*

**Figure 3.28:** Degree (a) and eigenvector centrality (b) distribution (compartment 1)

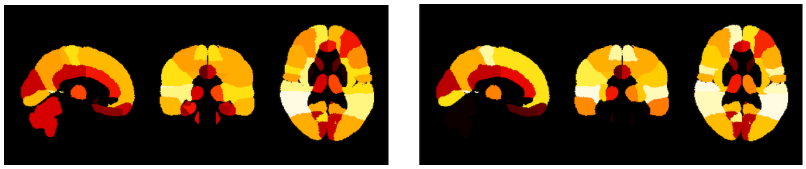

**(a)** *Degree distribution for each parcel (compartment 2)]*

**(b)** *Eigenvector centrality distribution for each parcel (compartment 2)*

**Figure 3.29:** Degree (a) and eigenvector centrality (b) distribution (compartment 2)

- The first 10 minutes have a strong distribution in the temporal and frontal lobes.
- The distribution of compartment 1 is strong in the frontal and parietal lobes.
- The distribution of compartment 2 is strong in the frontal, parietal and temporal lobes.

After having applied the graph metrics, the methodology to derive the hubs was implemented and these are shown in the figure 3.30. The hubs identified from the study of the metabolic connectivity matrices obtained from the different portions of the TAC and the time series of compartment 1 and 2 are such that there is good overlap, with the exception of compartment 1, which has a more characteristic distribution.
For compartment 1, the hubs are predominantly distributed in the Parietal Lobe. While, as also confirmed by the distribution of degree and eigenvector centrality on the Hammers atlas template, the hub nodes are predominantly in the Frontal Lobe (right and left) and Temporal (right and left) for all other cases.
The figure 3.31 shows the values of the Pearson's correlation coefficients calculated between the graph metrics (only degree is reported, as for strength and eigenvector centrality the results are consistent) of the time-series connectivity matrices, with the average values calculated across the subjects of $K_1$, $k_3$, $K_i$ and $SUVR$, after an appropriate z-score. The figure 3.32 shows the values of the Pearson's correlation coefficients calculated between the graph metrics (only degree

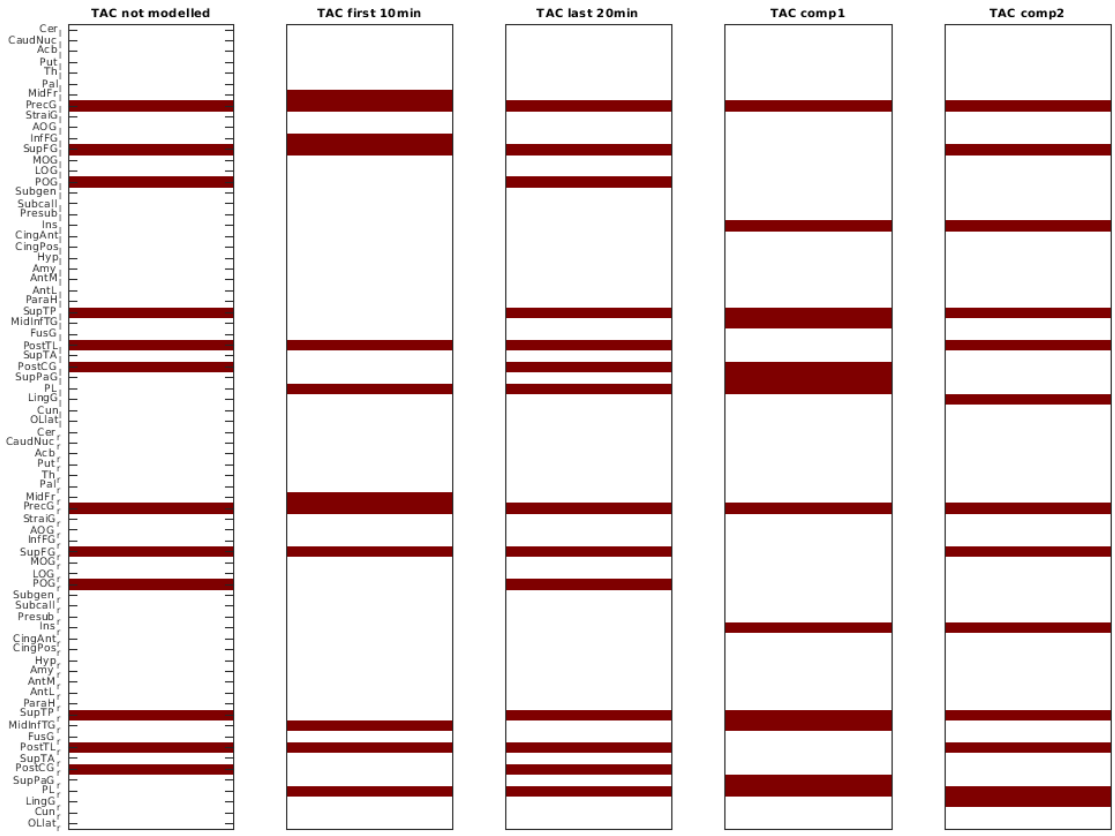


**Figure 3.30:** Identified hubs, as the nodes belonging to the top 20% of both degree and eigenvector centrality distributions, for the cases of *full TAC*, *first 10 minutes*, *last 20 minutes*, *compartment 1* and *compartment 2*.

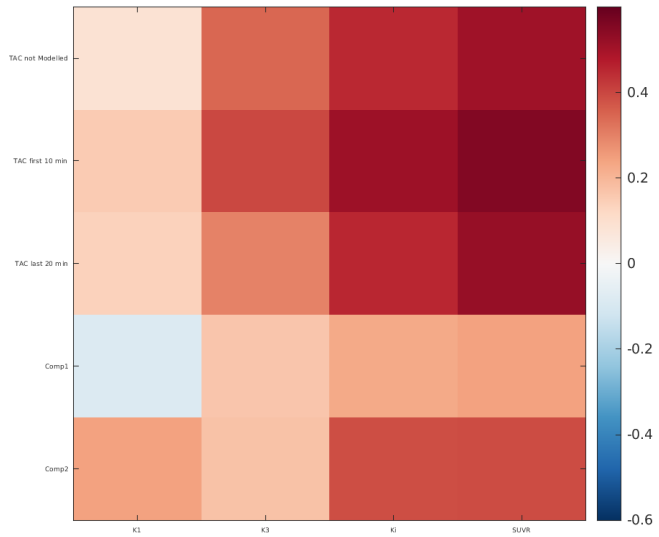


**Figure 3.31:** Correlation coefficients between MC time-series degree and mean parameters.

is reported, as for strength and eigenvector centrality the results are consistent) of the subject-series connectivity matrices, with the average values calculated

across the subjects of $K_1$, $k_3$, $K_i$ and $SUVR$, after an appropriate z-score. What

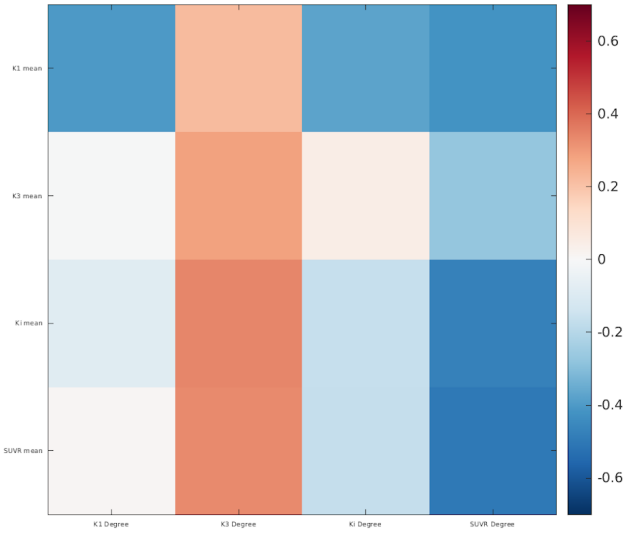


**Figure 3.32:** Correlation coefficients between MC subject-series degree and mean parameters.

is evident from the figures 3.31 and 3.32 is that:

- the degree of the time-series connectivity matrices, for all cases, has positive and high correlation values (around 0.6) with mean $SUVR$ and $K_i$ mainly, but also with mean $k_3$ (values around 0.3).
- In contrast, the degree of the subject-series connectivity matrices correlates much less and negatively with the mean values of the micro/macro parameters.

## 3.3 Enrichment analysis with brain receptor maps

The Pearson correlation coefficients between graph metrics of time-series metabolic connectivity (only degree is reported, as for strength and eigenvector centrality the results are consistent) and the neurochemical architecture are shown in the figure 3.33.
While the Pearson correlation coefficients between graph metrics of subject-series metabolic connectivity (only degree is reported) and the neurochemical architecture are shown in the figure 3.34.
From figure 3.33, emerges that:

- rCPS appears to be strongly correlated (values around 0.7) with the degree of the matrices from full TAC, first 10 minutes, last 20 minutes, time series

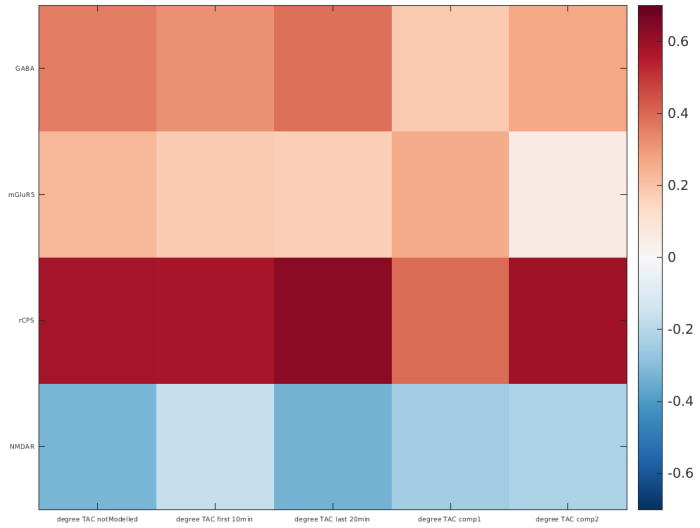


**Figure 3.33:** Pearson correlation coefficients between degree of time-series MC and the neurochemical architecture.

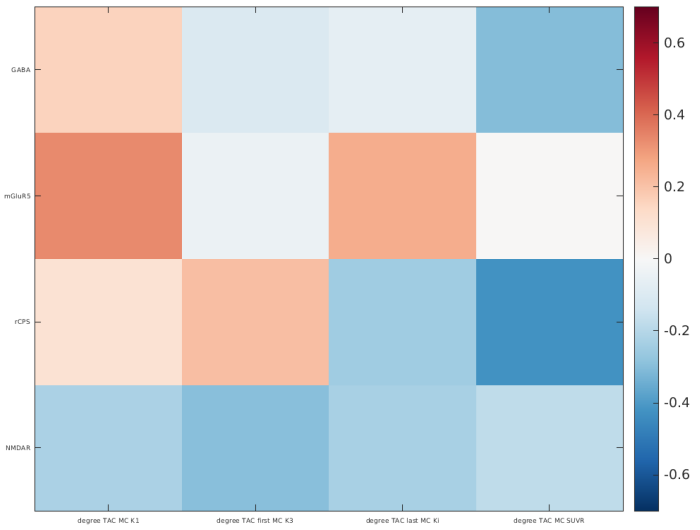


**Figure 3.34:** Pearson correlation coefficients between degree of subject-series MC and the neurochemical architecture.

of compartment 2, while the correlation values are weaker (around 0.4) with the degree of the MC matrix of compartment 1. This confirms the more different trend of compartment 1, compared with the other cases.

- NMDAR appears to be consistently anticorrelated with all cases, although with rather low values (around -0.3).

From figure 3.34, in contrast, no significant correlations emerge between the degree of MC subject-series matrices and neurochemical architecture.

With regard to the study of receptor density, the presence of a statistically significant difference between hub and non-hub nodes of the average time-series connectivity matrices, determined via Wilcoxon ranksum test, was found for the following cases:

- mGLUR5 and compartment 1 time courses: p-value=0,00061 (see fig. 3.35).

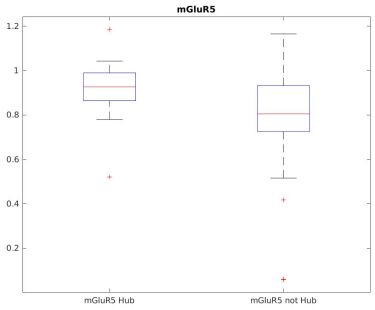


**Figure 3.35:** Hubs vs not-Hubs, compartment 1, case mGLUR5

- mGLUR5 and first 10 minutes: p-value=0,01820.
- rCPS and compartment 1: p-value=0,00195.
- rCPS and compartment 2: p-value=0,000004 (see fig. 3.36).

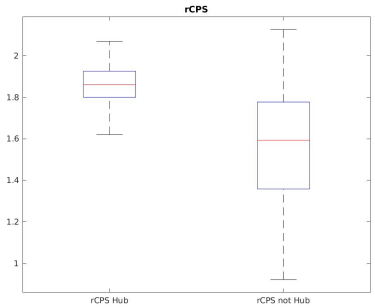


**Figure 3.36:** Hubs vs not-Hubs, compartment 2, case rCPS

- rCPS and first 10 minutes: p-value=0,00090 (see fig. 3.37).
- rCPS and last 20 minutes: p-value=0,00713.
- rCPS and full TAC: p-value=0,02579.
- GABA-A and compartment 1: p-value=0,00905.
- GABA-A and compartment 2: p-value=0,00099 (see fig. 3.38).

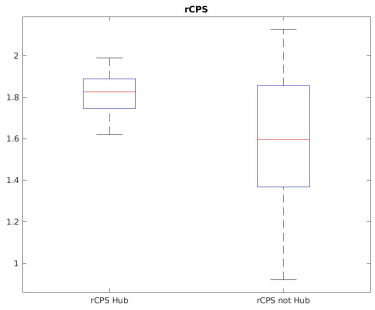


**Figure 3.37:** Hubs vs not-Hubs, first 10 minutes, case rCPS

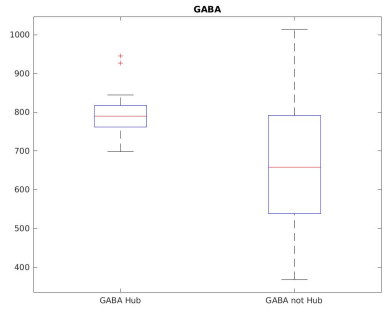


**Figure 3.38:** Hubs vs not-Hubs, compartment 2, case GABA-A

MC hubs are enriched in rCPS, mGluR5 is rich in first compartment and first 10-min hubs, and GABA is rich in first and second compartment hubs.

As for the case of subject-series connectivity matrices:

- rCPS and $K_1$: p-value=0,04658.
- mGLUR5 and $K_3$: p-value=0,00660.
- NMDAR and $SUVR$: p-value=0,00174 (see fig. 3.39).

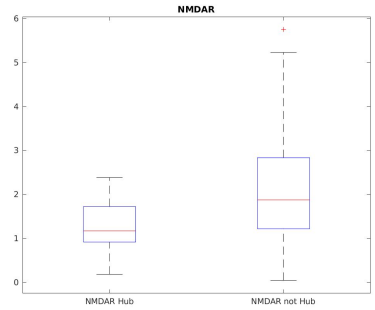


**Figure 3.39:** Hubs vs not-Hubs, $SUVR$, case NMDAR

- NMDAR and $K_i$: p-value=0,00166 (see fig. 3.40).

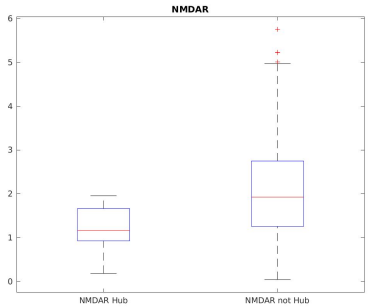


**Figure 3.40:** Hubs vs not-Hubs, $K_i$, case NMDAR

- GABA-A and $SUVR$: p-value=0,03593.

## 3.4 Estimation of metabolic connectivity matrices at parcel level: parcellation with Schaefer atlas

In this case, the number of voxels per parcel is sufficiently high and for this reason none of the regions were removed from the analysis. Results will be reported for Schaefer's 200 parcels, 7 networks case only.
The data-denoising approach as well as the chosen similarity metric were consistent with the Hammers case, i.e. 3 by 3 average on the first 24 frames and Euclidean Similarity non-normalised case. Below, see fig. 3.41, the metabolic connectivity average matrices of the full TAC, first 10 minutes, first 20 minutes, last 20 minutes, compartment 1 and compartment 2 are shown.
The subject-series connectivity matrices are shown in the figure 3.42.
As in the Hammers case, even with the parcellation using Schaefer, both 200 and 100, at 7 and 17 networks, the study of the coefficients of variation confirmed the choice of Euclidean Similarity as the metric to determine the metabolic connectivity matrices, providing in fact low values of $median\ CV\% \pm MAD$. The table 3.10 shows the $median\ CV\% \pm MAD$ for the different CV matrices obtained by parcelling via Schaefer 200 with 7 networks, for the non-normalised Euclidean similarity case.
With regard to the correlations obtained between the different MC time-series matrices (full TAC, first 10 minutes, first 20 minutes, last 20 minutes, compartment 1 and compartment 2), the results (see fig. 3.43) obtained by Schaefer parcellation reproduce what emerged from Hammers parcellation:

- MC from full TAC is strongly correlated (correlation values around 0.9) with

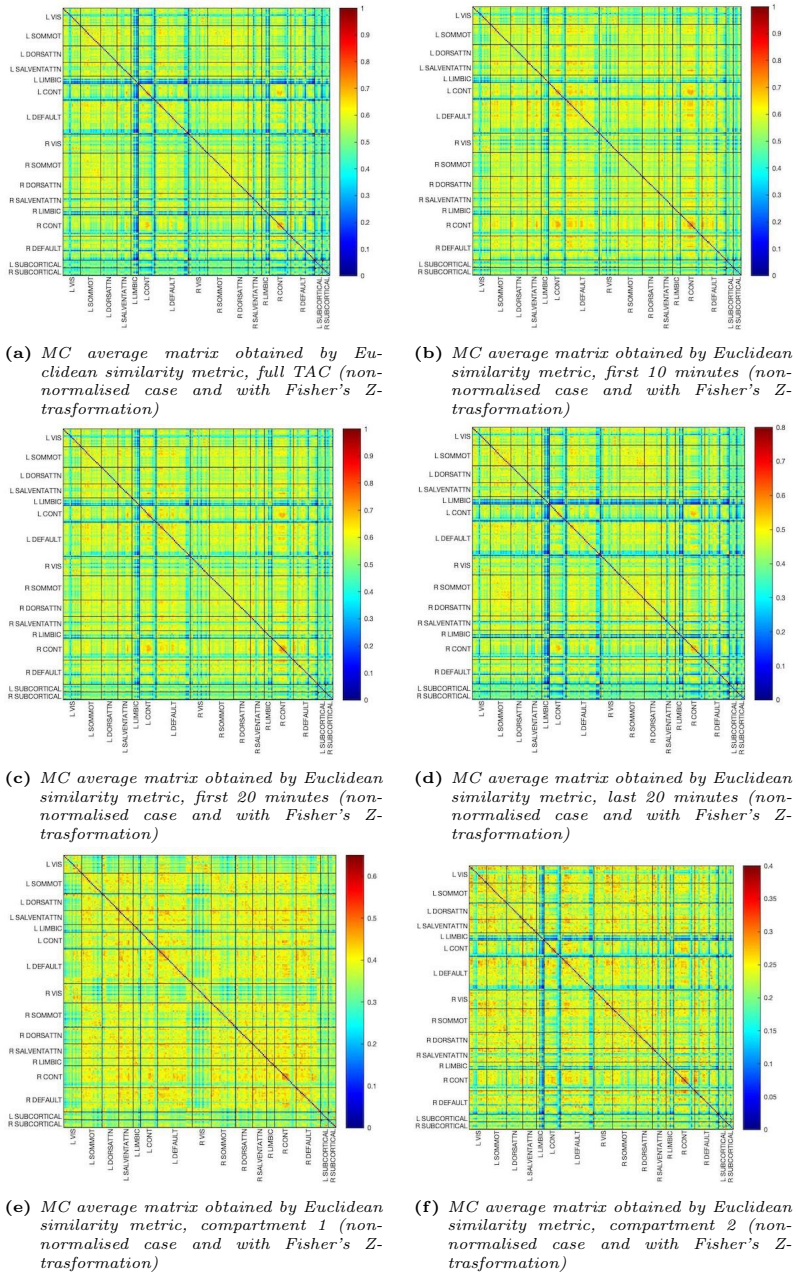

**(a)** *MC average matrix obtained by Euclidean similarity metric, full TAC (non-normalised case and with Fisher's Z-trasformation)*

**(b)** *MC average matrix obtained by Euclidean similarity metric, first 10 minutes (non-normalised case and with Fisher's Z-trasformation)*

**(c)** *MC average matrix obtained by Euclidean similarity metric, first 20 minutes (non-normalised case and with Fisher's Z-trasformation)*

**(d)** *MC average matrix obtained by Euclidean similarity metric, last 20 minutes (non-normalised case and with Fisher's Z-trasformation)*

**(e)** *MC average matrix obtained by Euclidean similarity metric, compartment 1 (non-normalised case and with Fisher's Z-trasformation)*

**(f)** *MC average matrix obtained by Euclidean similarity metric, compartment 2 (non-normalised case and with Fisher's Z-trasformation)*

**Figure 3.41:** MC average matrix obtained by Euclidean similarity metric, (non-normalised case and with Fisher's Z-trasformation).

MC from the last 20 minutes of TAC, strongly-moderately correlated (values around 0.8) with MC from the first 10 minutes of TAC and moderately correlated (values around 0.6) with MC from compartment 2.

- MC from compartment 2 turns out to be moderately correlated (values around 0.6) also with MC from the last 20 minutes.

- MC from compartment 1 appears to be uncorrelated with all other metabolic

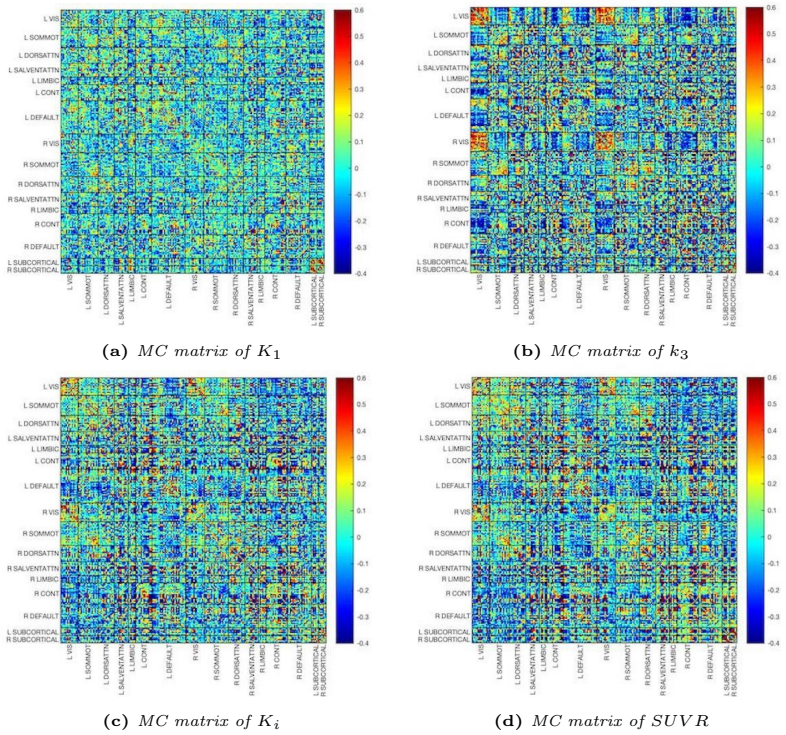

**(a)** *MC matrix of* $K_1$ **(b)** *MC matrix of* $k_3$

**(c)** *MC matrix of* $K_i$ **(d)** *MC matrix of* $SUVR$

**Figure 3.42:** MC matrices subject-series, obtained via Pearson's correlation across-subject.

**Table 3.10:** $median CV\% \pm MAD$ Schaefer 200 with 7 networks (non-normalised Euclidean similarity case)

| Type | $median\ CV\% \pm MAD$ |
|---|---|
| Full TAC | $25,3 \pm 5,4$ |
| First 10 minutes | $21,3 \pm 5,1$ |
| First 20 minutes | $23,5 \pm 5,5$ |
| Last 10 minutes | $29,3 \pm 5,5$ |
| Compartment 1 | $33,7 \pm 4,9$ |
| Compartment 2 | $39,7 \pm 6,6$ |

connectivity matrices.

With regard to the correlations between the mean time-series metabolic connectivity matrices and the subject-series matrices, see fig. 3.44, the results qualitatively reproduce for the most part what was found in the Hammers case, but with barely significant correlation values:

- the strongest relationship (correlation values around 0.35) is between the matrix of $k_3$ and the matrix of compartment 1, followed by a correlation of around 0.3 also between compartment 1 and both $K_1$ and $K_i$.
- $SUVR$ is totally uncorrelated with the MC time-series matrices.

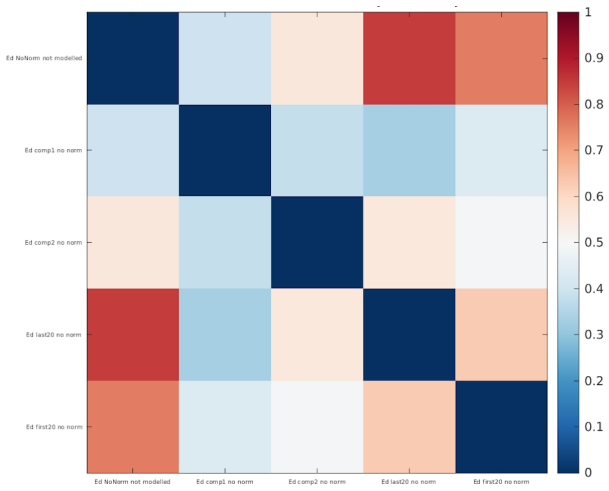


**Figure 3.43:** Pearson's correlation coefficients evaluated between the non-normalised case of Euclidean Similarity (Schaefer 200, 7 networks)

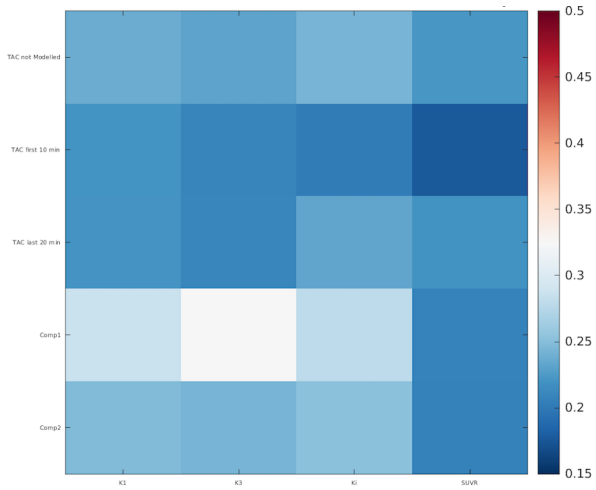


**Figure 3.44:** Pearson's correlation coefficients evaluated between MC time-series matrices and MC subject-series matrices (Schaefer 200, 7 networks). The correlation was performed between the entries of the vectorised matrices.

The degree distribution for each parcel is reported on the three-dimensional template of the Schaefer functional atlas, for the full TAC case (see fig. 3.45), first 10 minutes (see fig. 3.46), last 20 minutes (see fig. 3.47), compartment 1 (see fig. 3.48) and compartment 2 (see fig. 3.49).
What emerges is:

- The last 20 minutes and the full TAC have a similar pattern, with a strong distribution in the temporal and parietal lobe.
- The first 10 minutes have a strong distribution in the temporal and frontal lobes.

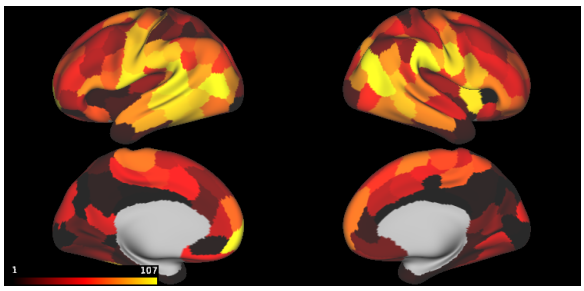


**Figure 3.45:** Degree distribution full TAC (Schaefer 200, 7 networks).

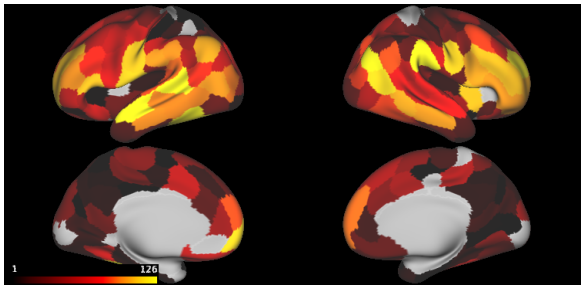


**Figure 3.46:** Degree distribution first 10 minutes (Schaefer 200, 7 networks).

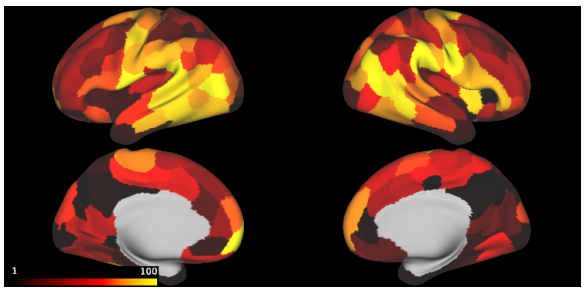


**Figure 3.47:** Degree distribution last 20 minutes (Schaefer 200, 7 network).

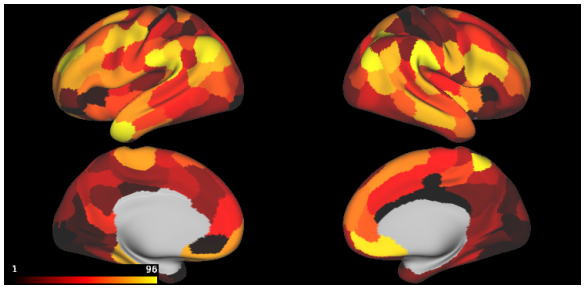


**Figure 3.48:** Degree distribution compartment 1 (Schaefer 200, 7 networks).

- Compartment 1 has a strong anterior distribution and in the temporal lobes, with lower cingulate cortex and medial part.
- Compartment 2 has very low Precuneus, and the highest part is in the temporal and parietal lobes.
- It is interesting to observe the difference between medial and lateral, with

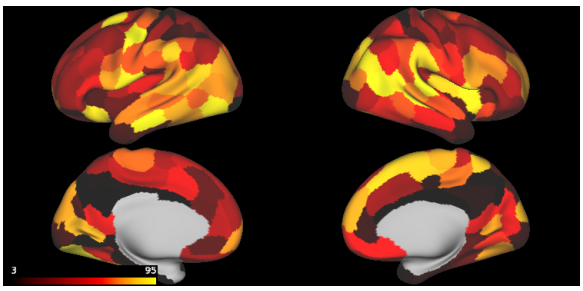


**Figure 3.49:** Degree distribution compartment 2 (Schaefer 200, 7 networks).

lower degree values observed in the medial view.

The results are consistent with what has already been observed for the degree distribution in the Hammers case.

The correlations between the graph metrics evaluated on the time-series connectivity matrices with the average value calculated across subjects of K1, k3, Ki and SUVR, is shown in the figure 3.50 (the metric is the degree and the Schaefer is the 200 at 7 networks). Qualitatively, the results are comparable to the Hammers case, but with less significant correlation values: the degree of the time series connectivity matrices, for all cases, has positive correlation values (around 0.3) with the mean $SUVR$, $K_i$ and $k_3$.
As for the subject-series case, the results are shown in the figure 3.51. Similarly to the Hammers case, the degree of subject-series connectivity matrices correlates much less and negatively with the average values of the micro/macro parameters.

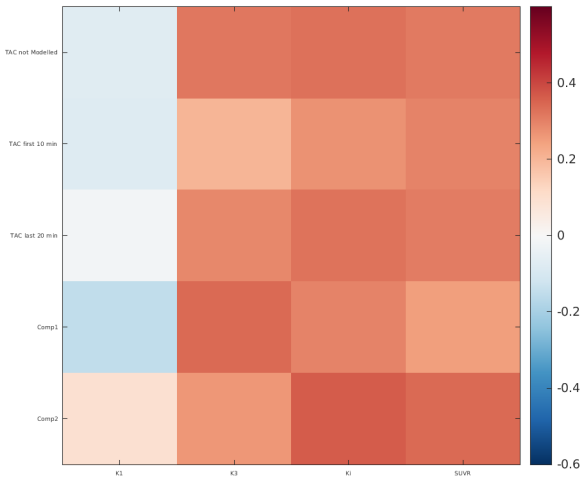


**Figure 3.50:** Correlation coefficients between MC time-series degree and mean parameters (Schaefer 200, 7 networks)

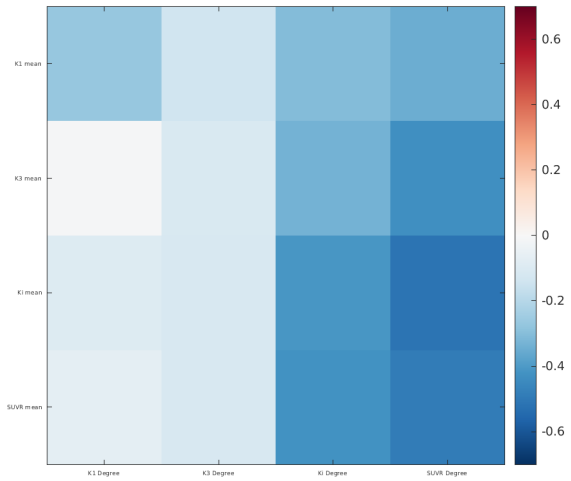


**Figure 3.51:** Correlation coefficients between MC subject-series degree and mean parameters (Schaefer 200, 7 networks)

With regard to the enrichment analysis with brain receptor maps, the Pearson's correlation coefficients between the graph metrics (only the degree is shown) of time-series connectivity and neurochemical archiectecture are reported in the figure 3.52, while for the case of subject-series connectivity matrices in fig. 3.53.

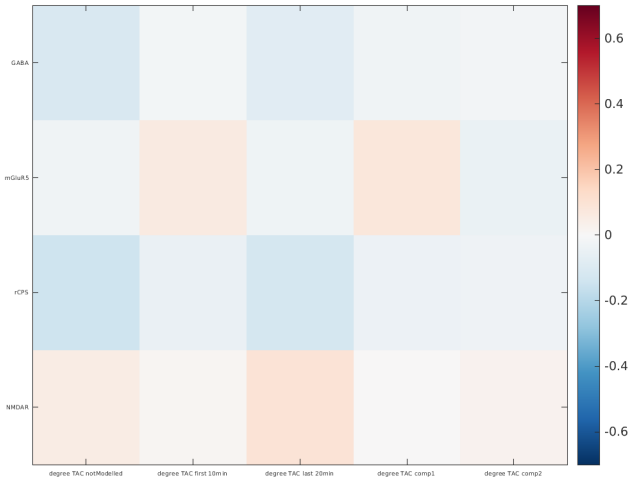


**Figure 3.52:** Pearson correlation coefficients between degree time-series MC (Schaefer 200, 7 networks) and the neurochemical architecture.

What emerges is the lack of significant correlations between the degree of the MC time-series matrices and the neurochemical architecture (contrary to previous findings in the Hammers case) and similar for the subject-series matrices.
In fact, even with regard to receptor density studies, for the time-series case, no significant differences were found between hub and non-hub nodes when applying the Wilcoxon ranksum test.
With regard to the subject-series case, significant differences emerged in the fol-

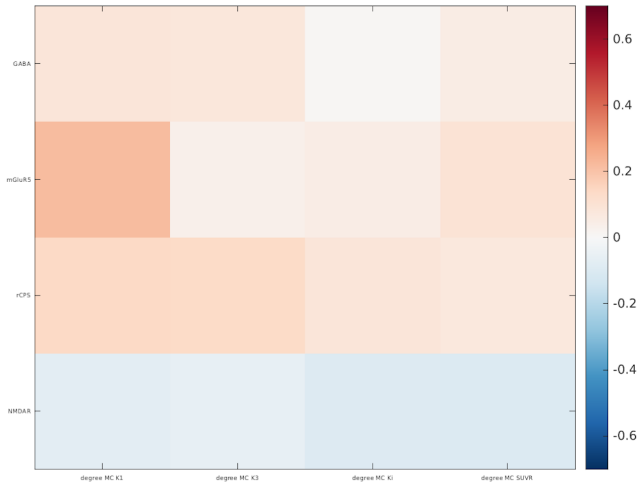


**Figure 3.53:** Pearson correlation coefficients between degree subject-series MC (Schaefer 200, 7 networks) and the neurochemical architecture.

lowing cases:

- NMDAR and $K_i$: p-value=0,02463.
- NMDAR and $SUVR$: p-value=0,02675.
- mGluR5 and $K_1$: p-value=0,00272.

## 3.5 Estimation of metabolic connectivity at voxel level

The dynamic of the voxels is reported in the figure 3.54.
Among the data denoising approaches tested, the most promising result, as also in the case of MC at parcel level, was obtained by averaging 3 by 3 the first 24 frames. The outcome of applying k-means clustering to voxel dynamics, following data denoising using this approach, with global normalisation 1 and squared Euclidean distance as a metric, is reported below (fig. 3.55).
Once the pre-processing was defined, ICA was applied with the GIFT toolbox to the PET 4D dynamics. The analysis performed on a single subject (3 by 3 average of the first 24 frames and normalisation 1) is shown below. Figure 3.56 shows the parameters set for the execution of ICA, figure 3.57 the stability indices ($I_q$) for ICA estimate-cluster and figure 3.58 the results of the Canonical Correlation analysis.
Finally, figure 3.59 shows the components extracted from ICA.
The results, however, are not satisfactory: the spatial maps of the components

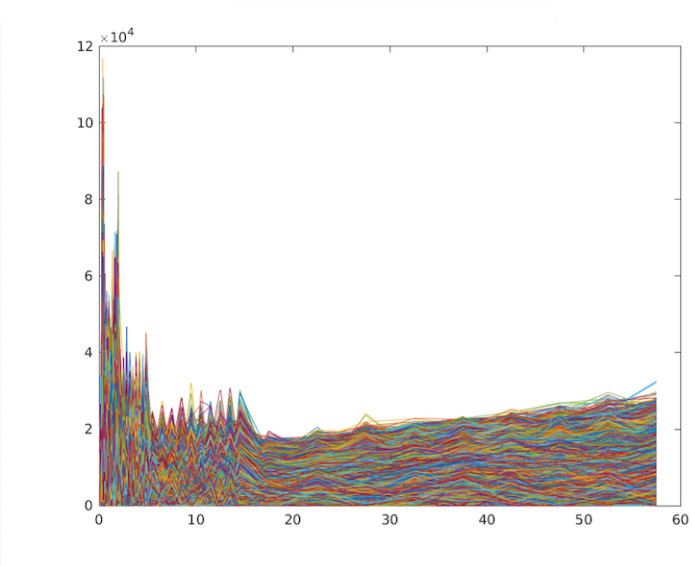


**Figure 3.54:** Voxels dynamic (GM, WM, CSF) interpolated with a uniform 5 s step grid.

are unable to highlight any structure, but only extract noise. The stability indices are also around values of 0.6-0.8, with only one component (the first one) having a stability index of 1. This implies that one component is identified (gray matter or white matter) and the remaining of the revealed components are noise. Even in the 2D CCA projection, the clusters are not distinct, but some turn out to be connected, again showing unpromising results.

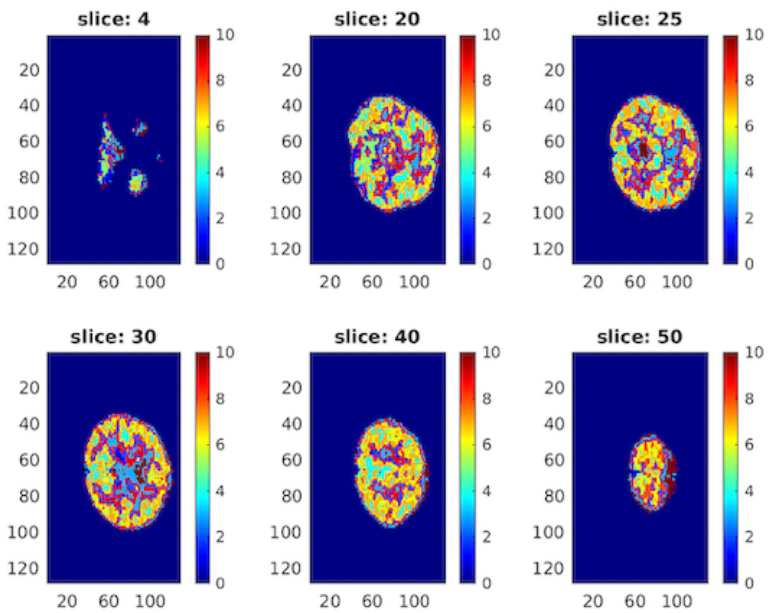


**(a)** *Clustering k-means on voxel dynamics following data denosing with 3 by 3 averaging on the first 24 frames, global normalisation 1 and squared Euclidea distance as a metric. The number of centroids was set to 10 and the replicates to 200.*

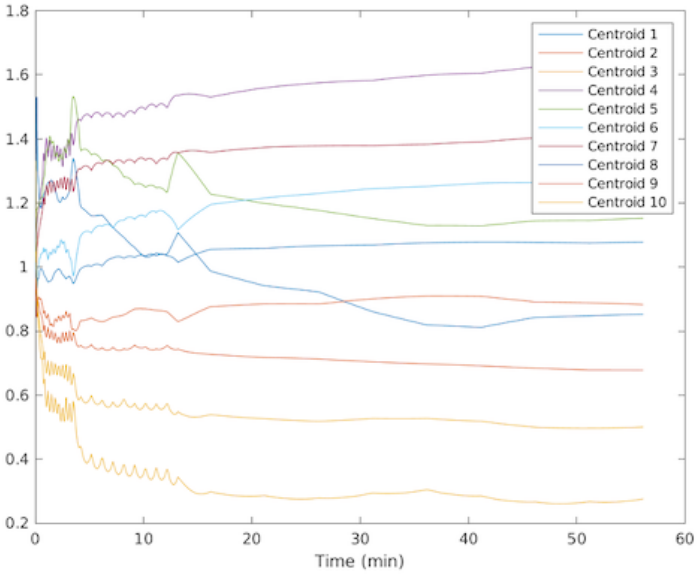


**(b)** *Trend over time of the 10 highlighted centroids.*

**Figure 3.55:** Application of k-means clustering to voxel dynamics, averaged 3 by 3 of the first 24 frames and global normalisation 1.

**Group ICA Parameters**

| |
|---|
| ..... |
| Number of Subjects : 1 |
| Number of Sessions : 1 |
| TR in seconds (Mean, Standard deviation): (5, 0) |
| Number of Independent Components : 10 |
| ICA Algorithm : Fast ICA |
| Number Of Scans/Timepoints (Mean, Standard deviation): (702, 0) |
| Mask File : r_GWLS_segmentation_noSkull |
| Data Pre-processing Type : Remove Mean Per Voxel |
| PCA Type : Standard |
| Group PCA Type : Subject Specific |
| Group ICA Type : Spatial |
| Back Reconstruction Type : GICA |
| Scaling Components : No Scaling |
| Stability analysis type : ICASSO |
| Group analysis mode: Parallel |
| Anatomical file: /nfsd/biopetmri4_tesi/ValliniGiulia_2021/DATA_HR+_WASHU/PROCESSED/108004/PET/Pre_processing_ICA/melodic_movemean11_gray/Melodic_output_norm1_movemean11_gray/mean.nii |
| Slice Plane: Axial |
| Image values: Positive and negative |
| Convert to Z-scores: no |
| Threshold: 1 |
| ..... |

**Figure 3.56:** ICA parameters choosen in the toolbox GIFT

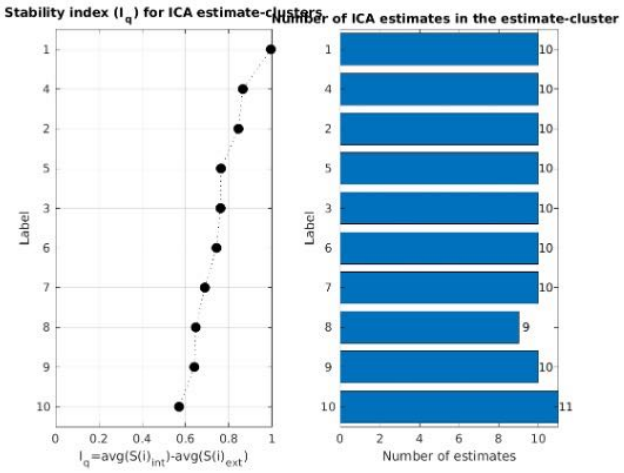


**Figure 3.57:** Stability index ($I_q$) for ICA estimate-cluster

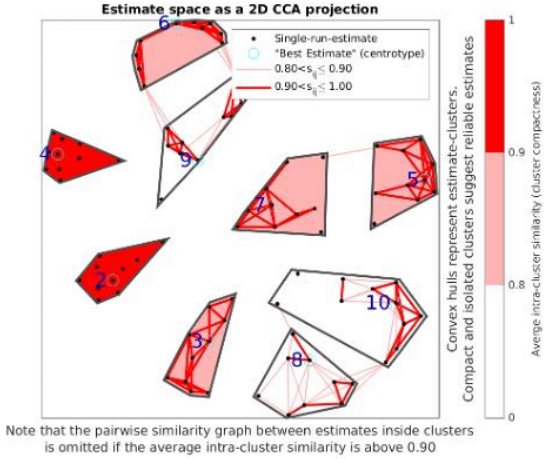


**Figure 3.58:** Estimate space as a 2D CCA projection

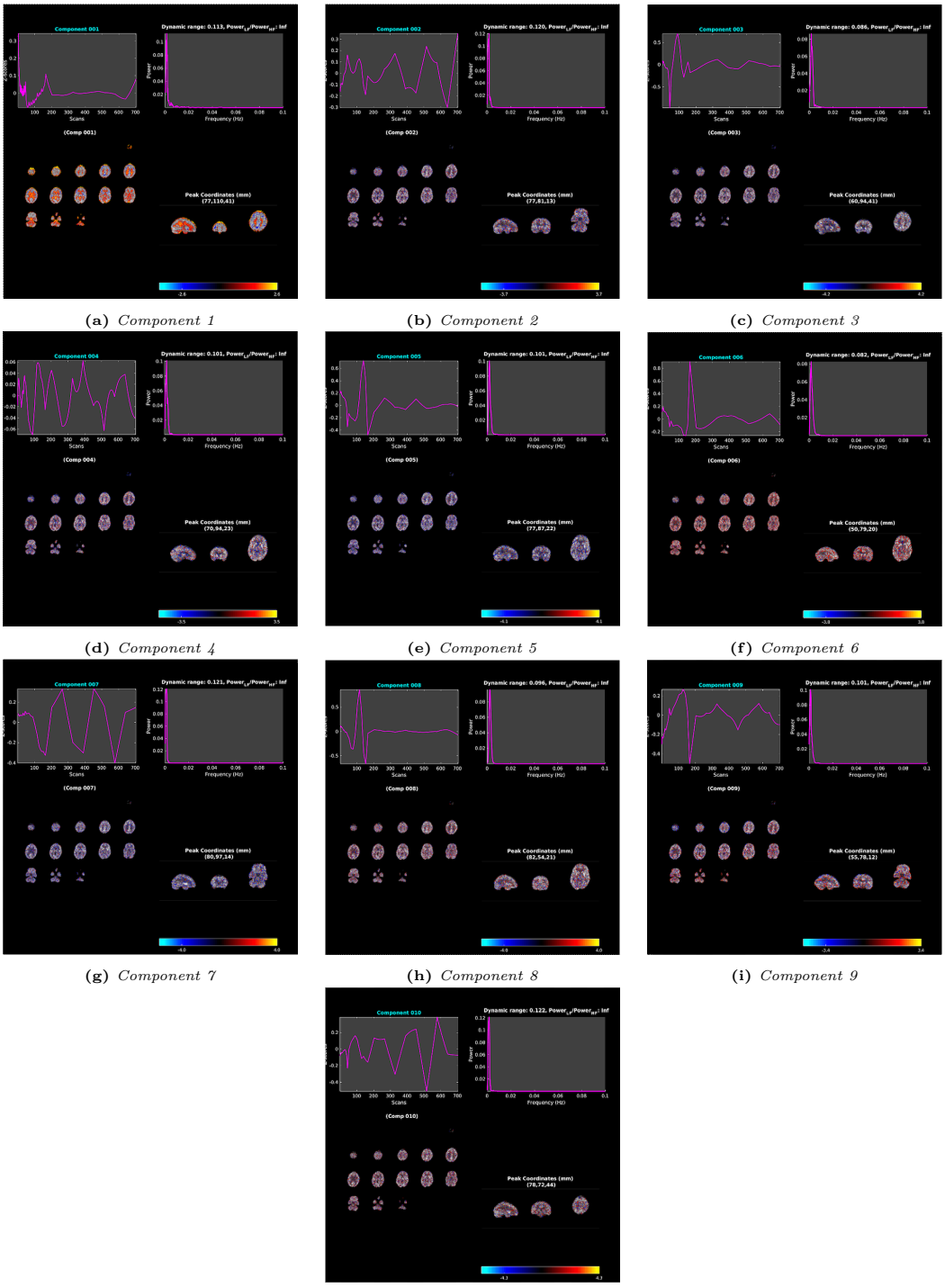


**(a)** *Component 1* **(b)** *Component 2* **(c)** *Component 3*

**(d)** *Component 4* **(e)** *Component 5* **(f)** *Component 6*

**(g)** *Component 7* **(h)** *Component 8* **(i)** *Component 9*

**(j)** *Component 10*

**Figure 3.59:** Components extracted from ICA

# Chapter 4

# Discussion

## 4.1 Estimation of metabolic connectivity matrices at parcel level: parcellation with Hammers atlas

The aim of this first part was to derive metabolic connectivity from dynamic [$^{18}$F]FDG PET at the individual subject level, with a focus on network characterisation and data standardisation, thus providing an appropriate mathematical method to extract "time series" connectivity maps from dynamic PET data.
The main problems we had to adress were the high level of noise in the available dataset and the multicollinearity of the time activity curves.
The first problem was solved by testing different data-denoising approaches, evaluating their effects on the TACs in terms of noise reduction and making sure the denoised signal still maintained a physiological time course which respected the count statics. From this analysis it emerged that the best results could be obtained by applying a 3 by 3 average over the first 24 frames.
In order to solve the multicollinearity problem, different metrics (Pearson's correlation, Euclidean Similarity, Gaussian Kernel and Cosine Similarity) and 5 different types of normalisation (6 also considering the non-normalised case) were tested. It can be seen from the carpet plots of the TACs that these normalisations highlight different characteristics of the signal:

- normalisations 1 (the most typically empoyed in the literature, Tomasi et al. (2017), Amend et al. (2019) and Ionescu et al. (2021)) and 2 emphasise

the signal fluctuations around the metabolic baseline or global signal;

- normalisation 3 emphasises the fluctuations of the signal with respect to itself;
- normalisation 4 leads to greater denoising of the initial part, thereby emphasising the tails and their separation;
- normalisation 5 performs the opposite of normalisation 4, thus emphasising mainly the initial part of the curve.

Once the MC matrices have been obtained, each symmetrical matrix can be imagined as organised into 4 blocks:

- upper left block: connectivity between the left hemisphere regions (LH);
- lower right block: connectivity between the right hemisphere regions (RH);
- lower left block and upper right block, as the connections between LH and RH.

In particular, considering the MC matrices obtained via Euclidean Similarity, on visual inspection, the left hemisphere-right hemisphere structure with homotopic interhemispheric connections, assessed by brain connectivity studies, is evident in most normalisation methods. In particular, they are most evident in the non-standardised case, in normalisation 1 and normalisation 4, and are represented by means of secondary diagonals. The matrices obtained through standardisation 3, on the other hand, show a pronounced block-diagonal structure with strong connectivity within each sub-network. In fact, since there is no gold standard, non-trivial differences in MC networks emerge with the different standardisation methods.
It is interesting to note that through the Euclidean Similarity metric (and similarly for the Gaussian Kernel) it is possible to identify a Network structure and in particular the homotopic interhemispheric connections even without adopting any type of normalisation. Therefore, choosing one of these metrics would solve the question of finding the most suitable normalisation, overcoming the problem encountered in the studies of Amend et al. (2019), Li et al. (2020), Tomasi et al. (2017) and Ionescu et al. (2021). While adopting a normalization reduces the multicollinearity between TACs, and allow to perform MC via correlations between PET signal fluctuations (similarly to what happens for fMRI FC), removing the positive trend (global signal) in PET TACs might lead to a significant

loss of information.
Homotopic interhemispheric connections are indeed supported by brain connectivity studies in the literature. In fact, how the left and right hemispheres are integrated is a crucial issue in neuroscience. For the two hemispheres, integration refers to the interaction between specialised regions, which enables long-range interhemispheric synchronisation and information flow. Various neuroimaging techniques have been applied to study functional integration between the two cerebral hemispheres. For example, Horwitz et al. (1984) used precisely PET-acquired regional metabolic rates to characterise functional integration between different brain regions. This study showed that all regions were significantly correlated with their contralateral parts. Other studies (Duffy et al, 1996), on the other hand, used electroencephalogram (EEG) recordings in the resting state, revealing synchronised electrical activity between the right and left hemispheres [64]. Resting-state fMRI has also been crucial in revealing patterns of spontaneous synchronised activity between homotopic regions of the right and left hemisphere [65]. Therefore, the metabolic connectivity results obtained in this study using the Euclidean Similarity metric with the non-normalised case are extremely promising, finding physiological support.

Also confirming the choice of Euclidean Similarity as a metric is the study of the coefficients of variation, relevant for assessing the inter-subject variability of the obtained connectivity matrices. In fact, evaluating the full CV matrices for the metric in question, the values are very low, and in particular for the non-normalised full TAC case, a $median\ CV\% \pm MAD$ of $8.3 \pm 28.9$ was obtained, therefore implies high reproducibility between subjects.

Interesting results emerged from the study of the correlations between the obtained time-series connectivity matrices: full TAC, first 10 minutes of the TAC, last 20 minutes, time series of compartment 1 and time series of compartment 2. It can be inferred that:

- the strong correlation between the MC matrices of the full TAC and the last 20 minutes is related to the fact that the Euclidean similarity metric is based on the distance between the curves, which is greater in the final portion of the TAC. For this reason, the final portion drives the values of the metric. Therefore, the last 20 minutes of the TAC provide the most information on the full TAC in terms of metabolic connectivity.

- The medium-strong correlations between the MC from compartment 2 and both MC from full TAC and from the last 20 minutes of the TAC suggest that from these two it is possible to derive information regarding the time course of the concentration of the tracer phosphorylated by the hexokinase enzyme (time series of compartment 2). Thus, the application of compartmental modelling could be avoided.

- Nevertheless, it is not possible, from the simple study of portions of the TAC, to derive information regarding the time course of the free tracer concentration in the tissue (time series of compartment 1), so compartmental modelling would be necessary in this case, as the MC from compartment 1 does not correlate with any of the other matrices obtained.

With regard to the subject-series connectivity matrices obtained from $K_1$, $k_3$, $K_i$ and $SUVR$, what emerges is that a different parameter corresponds to a different network. In the literature, the study of metabolic connectivity is generally based on $SUVR$, but it is also useful to evaluate what emerges from the micro-parameters, in particular, while the networks that is highlighted from $SUVR$, $K_i$ and $K_1$ are more similar, with highly connected regions in the Temporal lobe, what emerges from $k_3$ is more peculiar, with highly connected regions in the Parietal and Frontal lobes.

Assessing the relationships between the subject-series and time-series connectivity matrices, it can be deduced that:

- the absence of correlation between the MC matrix from the SUVR with all time-series matrices casts doubt on its significance and validity for metabolic connectivity studies. The results of this research would open up new perspectives for metabolic connectivity studies, opposing what has been done so far in the literature, as MC is generally studied as an across-subject correlation from SUVR values.

- The positive correlation between MC from compartment 1 and MC from $K_1$ and $k_3$ is consistent with the structure of Sokoloff's model, as is the positive correlation between compartment 2 and $k_3$.

In particular, what emerges is the difference between what is revealed by time-series matrices versus subject-series matrices. This result is somewhat analogous to Simpson's paradox [66], according to which a relationship observed at the level

of the population is reversed at the level of the individuals that constitute it [67]. What has in fact been found in this thesis is a substantial difference between the connectivity matrix obtained from the SUVR as a covariation of metabolic information across subjects, a matrix generally referred to in the literature and obtained at the group level, and the time-series connectivity matrices obtained as a relationship between the time series of each region thus at the level of the individual (within subject).
Simpson's paradox is a special case of the "ecological fallacy" [68] and the related concept of "ergodicity" [67]. Ergodic processes occur when a group-level result is generalisable to the individuals in the sample. Actually, ergodic processes are rather rare, because two strict criteria must be fulfilled:

1. the process must be homogeneous across individuals in a sample;

2. the statistical parameters describing the process must be constant or stationary over time.

Brain connectivity as measured by neuroimaging data does not meet the criteria of ergodicity and therefore results at the group level are not generalisable to individuals within the group [69]. In fact, as the study by Fisher et al. (2018) shows, non-ergodicity is a threat to human subjects research because the full extent of the problem is not known and it is not being adequately studied; furthermore, he argues that scientists need to demonstrate consistency between individual and group variability before generalising results across levels of analysis.
Due to the technical limitations of the PET imaging method, existing studies on resting-state metabolic connectivity have been limited to examining group-level covariance rather than within-subject correlation of FDG-PET time series. Researchers have attempted to draw rather strong conclusions based on these findings, including attempts to use metabolic covariance as a biomarker of disease [27].
By definition, a biomarker must be individually estimable (FDA-NIH 2019). Our results suggest that metabolic covariance cannot be used to predict within-subject connectivity. Although subject-series connectivity matrix analyses may be useful in other contexts, future attempts to explore metabolic connectivity as a biomarker of disease should use time-series connectivity as the only statistically valid approach.

## 4.2 Graph theory metrics and hubs

Network science or "graph theory" can be used to elucidate key organizational features of the brain's connectome architecture and to make predictions about the role of network elements and network attributes in brain function. Brain networks can be described mathematically as graphs, which essentially comprise sets of nodes (parcels) and edges (their interconnections). The extraction of brain networks from human imaging data and the many opportunities of graph-based approaches have been the subject of several recent reviews. One interesting aspect is that graph theory offers a wide range of objective data-based measures to characterise the topology of networks. An important subset of these measures identifies network elements (nodes or edges) that are likely to have a strong influence on the communication and integration of information and thus on the overall network function. In network science, nodes that are positioned to make a strong contribution to the overall network function are generally referred to as network hubs. Hubs can be identified using many different graph measures, the simplest one used to identify hubs being the node degree. However, no single measure is necessary and sufficient to define network hubs, which is why it is often advantageous to identify hubs by aggregating different graph measures. In the present study, it was decided to derive hubs as the nodes belonging to the top 20% of both degree and eigenvector centrality distributions.

The identified hubs are mostly located in the Parietal lobe with regard to Compartment 1, which has a more characteristic pattern, and in the Frontal and Temporal lobe with regard to all the remaining cases.

The study of the hubs of metabolic connectivity from time-series matrices has never been addressed before in the literature, however, the results obtained here are confirmed in the study conducted by Jamadar et al. (2021) on functional-PET, in which the analysis of the degree of connectivity matrices is further investigated, highlighting the higher degree regions as those in the Temporal, Frontal and Parietal lobes [70].

Therefore, these results indicate that the hub regions identified in this study are indeed physiologically significant and illustrate the potential application of the proposed method, as hub regions are generally altered in various brain disorders, such as Alzheimer's disease and schizophrenia [71]. Therefore, the potential of hub regions as imaging markers for diagnosis and patient stratification is an interesting topic for future research.

The match between the graph metrics of the time-series connectivity matrices and the average maps of $K_1$, $k_3$, $K_i$ and $SUVR$ again confirms the more singular trend of compartment 1, which is not correlated with any mean map. While the strongest positive correlation is between the average $SUVR$ map, as a local measure of metabolism, and the degree of full TAC, first 10 minutes and last 20 minutes. These strong and positive correlations between the average SUVR map and the graph metrics of the time-series connectivity matrices can be interpreted from a physiological point of view: regions with high degree (the same goes for in strength and eigenvector centrality), thus which can be considered brain hubs, are associated with high metabolic demand.
This suggests that informational nodes within the brain are highly metabolic, and reflects to some extent the relationship that has been derived with rCPS and set out below.
This pattern is not consistent when considering the correlation between average maps and graph metrics of subject-series connectivity matrices. In this case, in fact, the $SUVR$, $K_i$ and $K_1$ networks have negative correlations with the mean maps. In particular, the $SUVR$ network is the most strongly negatively correlated, which would mean that even the higher the $SUVR$ of a node, the less that node covaries with the others across subjects, i.e. that node has low variability across subjects, and is always high in all of them, so it covaries weakly with other regions.

## 4.3 Enrichment analysis with brain receptor maps

A direct physiological interpretation of hubness measures is still missing, and investigating, through the development of appropriate mathematical and statistical approaches, how molecularly rich these hubs are in terms of receptor and transporter density will help provide insights for targeted pharmacological and neurostimulation interventions.
Neurotransmitters are chemical agents that transmit messages across synapses, and are the key molecules of neural signalling. While neurotransmitters carry the message, neurotransmitter receptors act as ears covering the cell membrane, determining the response of the postsynaptic neuron. Neurotransmitter receptors effectively mediate the transfer and propagation of electrical impulses, modulating excitability, the firing rate of the cell, modifying neural states and ultimately

shaping communication at the network level.
What emerged from the evaluation of the correlation of the time-series connectivity graph metrics with the neurochemical architecture is a strong positive correlation between the rate of protein synthesis and the metrics of all matrices. One possible reason for the strong associations between rCPS and MC graph metrics (time-series) may be that protein synthesis is directly associated with a high metabolic rate, or vice versa. As shown by previous results on the relationships between graph metrics and the mean SUVR map, it is precisely regions of high degree (analogue in strength and eigenvector centrality) that are associated with high metabolic demand. Free leucine (L-[1-$^{11}$C]leucine PET is used to measure protein synthesis in vivo in the brain) is in fact one of the main amino acid donors for glutamate synthesis in the brain [72]. Since an increase in metabolic load would be associated with glutamate production, it follows that an increase in metabolic load in the regions would be similarly associated with measures of protein turnover, which explains the similarity of the relationship between rCPS and the mean SUVR map with metabolic connectivity graph metrics. To confirm this, a study by Wilcoxon ranksum test of the presence of significant differences between hub and non-hub nodes in terms of receptor density highlights that hub nodes are clearly enriched in rCPS.
These relationships are thus confirmed from a physiological point of view, in contrast to the findings of correlations between the graph metrics of the MC subject-series matrices and the neurochemical architecture. In this case, in fact, no significant correlations emerged.

## 4.4 Estimation of metabolic connectivity matrices at parcel level: parcellation with Schaefer atlas

After having conducted the complete study using parcellation with the Hammers anatomical atlas, it was decided to repeat the analysis by parcellation with the Schaefer functional atlas, both at 100 and 200 parcels, with both 7 and 17 networks. A functional atlas was introduced because the aim was to include metabolic connectivity in studies of connectomics, which already incorporate functional connectivity, structural connectivity and effective connectivity, not by keeping it separate, but by opting to integrate it, so a study with a functional atlas was a necessary test to be carried out.
By testing the various metrics (Pearson's correlation, Cosine similarity, Euclidean

similarity and Gaussian Kernel) and normalisations, what emerged confirmed the results of the Hammers case, i.e. from visual inspection and analysis of the coefficients of variation, Euclidean similarity was chosen with the non-normalised case as the metric to derive the metabolic connectivity matrices. For the full TAC case in fact the $median\ CV \pm MAD$ is $25,3 \pm 5,4$ confirming the high inter-subject reproducibility of the MC matrices obtained at individual level.

Proceeding with the subsequent analyses, the correlation studies between the obtained time-series connectivity matrices reflect the findings of the Hammers studies:

- the strong correlation between the MC matrices of the full TAC and the last 20 minutes is related to the fact that the Euclidean similarity metric is based on the distance between the curves, which is greater in the final portion of the TAC. For this reason, the final portion drives the values of the metric.
- The medium-strong correlations between the MC from compartment 2 and both MC from full TAC and from the last 20 minutes of the TAC suggest that from these two it is possible to derive information regarding the time course of the concentration of the tracer phosphorylated by the hexokinase enzyme (time series of compartment 2).
- Nevertheless, the MC from compartment 1 does not correlate with any of the other matrices obtained.

Subsequently, the correlation between subject-series and time-series connectivity matrices was assessed. The pattern of correlations mostly reflects what was evident in the Hammers case, but with lower correlation values. The strongest positive correlations are between the matrix of compartment 1 and both matrices of $K_1$ and $k_3$. In particular, also in this case it is significant to note that the $SUVR$ subject-series matrix is uncorrelated from the remaining MC time-series matrices.
Thus, as in the Hammers case, the difference between what is revealed by time-series matrices and subject-series matrices emerges, and therefore the previous discussion regarding Simpson's Paradox can be extended.

The next step involves the application of graph metrics to metabolic connectivity matrices. The degree distribution replicates what was observed for the

Hammers case, i.e. in general stronger in the Frontal, Parietal and Temporal areas, but with the difference of lower values in the medial than in the lateral region.

Also with regard to the evaluation of the correlation between the calculated average across-subject maps of $SUVR$, $K_1$, $K_i$ and $k_3$, with the time-series connectivity graph metrics, what emerges is qualitatively the same as in the Hammer case, but with lower correlation values. Thus, the average $SUVR$ map correlates positively with the MC time-series degree metrics, confirming also in the Schaefer case how high degree regions (same for strength and centrality of the eigenvectors), which can thus be considered brain hubs, are associated with high metabolic demand.
Similarly to the Hammers case, even with Schaefer parcellation, the absence of correlation, or negative correlations between mean maps and MC subject-series graph metrics emerges.
However, the correlations that resulted in both cases, are particularly low and not significant, this is probably due to the very detailed parcellation associated with the atlas used (100 and 200 parcels) from which an increase in noise is derived, and the PET data in question probably cannot support such a fine parcellation.

The effect of such fine parcellation for the data in question, which is already very noisy, can be detected when evaluating the correlation of time-series and subject-series connectivity graph metrics with the neurochemical architecture. In fact, what is evident is the total absence of correlation. Another factor that may then affect the correlation result with the graph metrics is the characteristic and ubiquitous property of brain maps: spatial autocorrelation (SA) [73]. Due to SA, brain feature values in spatially close regions tend to be more similar than values in spatially distant regions. Therefore, the latter is a factor that will have to be appropriately evaluated in future developments of this project.

## 4.5 Estimation of metabolic connectivity at voxel level

After estimating metabolic connectivity matrices at the parcel level, an attempt was made to assess MC at the voxel level by means of independent component analysis using the GIFT toolbox. This type of analysis had already been tried previously, recalling the studies of Wehrl et al. (2013) with the result of extracting

7 networks showing similarities to those described in the fMRI literature, using this technique. However, the areas found in ICA PET are smaller than the regions assigned in fc-fMRI. In contrast, the study by Tomasi et al. (2017) showed only two anticorrelated components: the first component incorporates cerebellum, pons, medial temporal cortex regions and anterior thalamus, while the second component includes cortical regions.
Finally, the study by Ionescu et al. (2021), in which the ICA readout of [$^{18}$F]FDG data broadly mirrors what has been reported in previous rat studies (Wehrl et al., 2013), but many components indicate a focal, unilateral signal. The use of a different number of components may help to address this problem; however, one of the main reasons for this observation is the low signal-to-noise ratio that "traditional PET data" have at the voxel level [39]. Indeed, what is already stated by the authors is that voxel-wise approaches such as ICA are probably less suitable for the analysis of [$^{18}$F]FDG connectivity than FC.
What emerges from the spatial maps of the components from our analysis is the inability to highlight any structure. This is in agreement with what was reported above from Ionescu's study, hence the need to use pairwise correlation approaches to derive MC, with nodes large enough to avoid noisy signals. In fact, the data under investigation is particularly noisy, which is also due to the low-quality scanner used (Siemens ECAT HR+ 962 PET scanner), compared to the certainly higher-performance scanner used in Wherl's study (Siemens Inveon). In addition to this, the promising results obtained at the parcel level use a distance-based metric, which was therefore found to be the optimal metric to deal with PET data, however none of the algorithms proposed in GIFT to perform ICA are distance-based, so the difficulty in extracting structures may also be related to finding the most appropriate algorithm, possibly modifying those already present. Even this can be the focus of future studies and investigations.

# Chapter 5

# Conclusion

The aim of this thesis is to develop a mathematical method to perform metabolic connectivity from dynamic PET data, using [$^{18}$F]FDG as a tracer. This in order to introduce metabolic connectivity into connectomics studies, which already incorporate functional connectivity, structural connectivity and effective connectivity, but lack metabolic information and enrichment through receptor studies. Hence, this would lay the foundation for the introduction of a new biomarker to decode brain disorders in order to prevent them and investigate them by means of targeted approaches.

Four possible metrics (Pearson's correlation, Cosine similarity, Euclidean similarity, Gaussian Kerne,) were proposed and tested on both the non-normalised TAC and the normalised TAC with 5 different standardisations showing different signal features. The Euclidean similarity metric with the non-normalised case was selected, among other combinations, both for its high inter-subject reproducibility and because it shows consistent identification of interhemispheric and homotopic connections, as expected from brain connectivity studies. The advantage of this metric is its ability to highlight a network structure even without adopting any kind of normalisation: while adopting a normalization reduces the multicollinearity between TACs, and allow to perform MC via correlations between PET signal fluctuaztions (similarly to what happens for fMRI FC), removing the positive trend (global signal) in PET TACs might lead to a significan loss of information.

The study then proceeded to evaluate possible correlations between the time-series metabolic connectivity matrices (full TAC, last 20 minutes, first 10 minutes, time series of compartment 1 and compartment 2) and subject-series (SUVR, K1, k3, Ki). This revealed an absence of correlation between the time-series matrices

and the SUVR subject-series matrices, highlighting the strong difference between this new approach of obtaining matrices at the subject level, compared to the standard approach of across-subject covariation of metabolic information.
Calling into question the physiological interpretation and therefore the applicability of the subject-series matrices are also the correlation studies between graph metrics of time-series and subject-series matrices with both average maps of micro/macroparameters ($SUVR$, $K_1$, $k_3$, $K_i$) and the neurochemical architecture. The strong and positive correlation between the graph metrics of MC time-series and both the average map of $SUVR$ and the rate of protein synthesis is consistent with what is expected from a physiological point of view and is not found instead considering the graph metrics of subject-series MC.
The Schaefer parcellation partly confirmed what emerged with the Hammers case, but the lower correlation values that tend to be obtained are probably related to the very fine parcellation that is introduced in this case (100 or 200 parcels), which leads to an increase in noise in an already very noisy dataset and is therefore not suitable for this PET data. In future studies, the level of autocorrelation of the receptor maps that may affect the relationships that emerge will also have to be assessed.
Finally, the analysis at the voxel level did not give satisfactory results, probably because of the low signal-to-noise ratio at the voxel level and the algorithm of estimation of the components which, not being based on distance as the Euclidean similarity, is not able to extract significant structures, therefore in future studies such algorithms should be adapted to the PET data accordingly.

# Appendix A

# Materials

**Table A.1:** Dataset information

| *Subject ID* | *Age* | *Sex* | *Time Grid* |
|---|---|---|---|
| 108295 | 52 | Male | 24x5s 9x20s 10x60s 9x300s |
| 108293 | 42 | Male | 24x5s 9x20s 10x60s 9x300s |
| 108291 | 55 | Male | 24x5s 9x20s 10x60s 9x300s |
| 108289 | 46 | Male | 24x5s 9x20s 10x60s 9x300s |
| 108285 | 35 | Female | 24x5s 9x20s 10x60s 9x300s |
| 108283 | 39 | Male | 24x5s 9x20s 10x60s 9x300s |
| 108281 | 49 | Male | 24x5s 9x20s 10x60s 9x300s |
| 108280 | 53 | Female | 24x5s 9x20s 10x60s 9x300s |
| 108279 | 40 | Female | 24x5s 9x20s 10x60s 9x300s |
| 108263 | 59 | Female | 24x5s 9x20s 10x60s 9x300s |
| 108262 | 65 | Male | 24x5s 9x20s 10x60s 9x300s |
| 108261 | 71 | Male | 24x5s 9x20s 10x60s 9x300s |
| 108251 | 61 | Female | 24x5s 9x20s 10x60s 9x300s |
| 108249 | 58 | Male | 24x5s 9x20s 10x60s 9x300s |
| 108248 | 59 | Female | 24x5s 9x20s 10x60s 9x300s |
| 108245 | 28 | Female | 24x5s 9x20s 10x60s 9x300s |
| 108244 | 56 | Male | 24x5s 9x20s 10x60s 9x300s |
| 108241 | 62 | Male | 24x5s 9x20s 10x60s 9x300s |
| 108239 | 85 | Male | 23x5s 9x20s 10x60s 9x300s |
| 108238 | 71 | Female | 24x5s 9x20s 10x60s 9x300s |
| 108237 | 62 | Male | 24x5s 9x20s 10x60s 9x300s |
| 108236 | 66 | Male | 24x5s 9x20s 10x60s 9x300s |

| | | | |
|---|---|---|---|
| 108235 | 56 | Male | 24x5s 9x20s 10x60s 9x300s |
| 108234 | 66 | Female | 22x5s 9x20s 10x60s 9x300s |
| 108232 | 25 | Female | 24x5s 9x20s 10x60s 9x300s |
| 108231 | 25 | Male | 24x5s 9x20s 10x60s 9x300s |
| 108230 | 77 | Female | 24x5s 9x20s 10x60s 9x300s |
| 108229 | 27 | Female | 24x5s 9x20s 10x60s 9x300s |
| 108228 | 58 | Female | 24x5s 9x20s 10x60s 9x300s |
| 108227 | 25 | Male | 24x5s 9x20s 10x60s 9x300s |
| 108226 | 28 | Male | 24x5s 9x20s 10x60s 9x300s |
| 108225 | 28 | Female | 24x5s 9x20s 10x60s 9x300s |
| 108224 | 58 | Male | 24x5s 9x20s 10x60s 9x300s |
| 108223 | 54 | Male | 24x5s 9x20s 10x60s 9x300s |
| 108222 | 68 | Male | 24x5s 9x20s 10x60s 9x300s |
| 108214 | 63 | Female | 24x5s 9x20s 10x60s 9x300s |
| 108208 | 75 | Female | 23x5s 9x20s 10x60s 9x300s |
| 108206 | 68 | Female | 24x5s 9x20s 10x60s 9x300s |
| 108205 | 66 | Female | 24x5s 9x20s 10x60s 9x300s |
| 108202 | 69 | Female | 24x5s 9x20s 10x60s 9x300s |
| 108200 | 68 | Female | 24x5s 9x20s 10x60s 9x300s |
| 108199 | 70 | Female | 24x5s 9x20s 10x60s 9x300s |
| 108194 | 70 | Female | 24x5s 9x20s 10x60s 9x300s |
| 108191 | 72 | Male | 24x5s 9x20s 10x60s 9x300s |
| 108189 | 68 | Female | 24x5s 9x20s 10x60s 9x300s |
| 108187 | 70 | Female | 24x5s 9x20s 10x60s 9x300s |
| 108185 | 71 | Female | 24x5s 9x20s 10x60s 9x300s |
| 108183 | 82 | Female | 24x5s 9x20s 10x60s 9x300s |
| 108182 | 70 | Female | 24x5s 9x20s 10x60s 9x300s |
| 108181 | 76 | Male | 24x5s 9x20s 10x60s 9x300s |
| 108179 | 72 | Female | 24x5s 9x20s 10x60s 9x300s |
| 108176 | 50 | Male | 24x5s 9x20s 10x60s 9x300s |
| 108174 | 56 | Female | 24x5s 9x20s 10x60s 9x300s |
| 108172 | 49 | Female | 24x5s 9x20s 10x60s 9x300s |
| 108170 | 76 | Male | 24x5s 9x20s 10x60s 9x300s |
| 108169 | 40 | Male | 24x5s 9x20s 10x60s 9x300s |
| 108050 | 35 | Female | 24x5s 9x20s 10x60s 9x300s |
| 108049 | 39 | Male | 24x5s 9x20s 10x60s 9x300s |

| | | | |
|---|---|---|---|
| 108046 | 56 | Male | 24x5s 9x20s 10x60s 9x300s |
| 108045 | 42 | Female | 24x5s 9x20s 10x60s 9x300s |
| 108044 | 67 | Female | 24x5s 9x20s 10x60s 9x300s |
| 108040 | 44 | Female | 23x5s 9x20s 10x60s 9x300s |
| 108038 | 68 | Female | 24x5s 9x20s 10x60s 9x300s |
| 108036 | 50 | Female | 24x5s 9x20s 10x60s 9x300s |
| 108029 | 46 | Female | 24x5s 9x20s 10x60s 9x300s |
| 108026 | 70 | Female | 24x5s 9x20s 10x60s 9x300s |
| 108016 | 55 | Female | 24x5s 9x20s 10x60s 9x300s |
| 108013 | 65 | Male | 24x5s 9x20s 10x60s 9x300s |
| 108007 | 38 | Male | 24x5s 9x20s 10x60s 9x300s |
| 108004 | 55 | Male | 24x5s 9x20s 10x60s 9x300s |

# Appendix B

# Labels Atlases

**Table B.1:** Labels of the 83 regions reported by the Hammers atlas.

| ***Number in Atlas*** | ***Name of Structure*** |
|---|---|
| | *Temporal Lobe* |
| 1; 2 | Hippocampus |
| 3; 4 | Amygdala |
| 5; 6 | Anterior temporal lobe, medial part |
| 7; 8 | Anterior temporal lobe, lateral part |
| 9; 10 | Parahippocampal and ambient gyri |
| 11; 12 | Superior temporal gyrus, posterior part |
| 13; 14 | Middle and inferior temporal gyrus |
| 15; 16 | Fusiform gyrus |
| 30; 31 | Posterior temporal lobe |
| 82; 83 | Superior temporal gyrus, anterior part |
| | *Posterior Fossa* |
| 17; 18 | Cerebellum |
| 19 | Brainstem |
| | *Insula and Cingulate gyri* |
| 20; 21 | Insula |
| 24; 25 | Cingulate gyrus (gyrus cinguli), anterior part |
| 26; 27 | Cingulate gyurs (gyrus cinguli), posterior part |
| | *Frontal Lobe* |
| 28; 29 | Middle frontal gyrus |
| 50; 51 | Precentral gyrus |
| 52; 53 | Straight gyrus |

| | |
|---|---|
| 54; 55 | Anterior orbital gyrus |
| 56; 57 | Inferior frontal gyrus |
| 58; 59 | Superior frontal gyrus |
| 68; 69 | Medial orbital gyrus |
| 70; 71 | Lateral orbital gyrus |
| 72; 73 | Posterior orbital gyrus |
| 76; 77 | Subgenual frontal cortex |
| 78; 79 | Subcallosal area |
| 80; 81 | Pre-subgenual frontal cortex |
| | *Occipital Lobe* |
| 64; 65 | Lingual gyrus |
| 66; 67 | Cuneus |
| 22; 23 | Lateral remainder of occipital lobe |
| | *Parietal Lobe* |
| 60; 61 | Postcentral gyrus |
| 62; 63 | Superior parietal gyrus |
| 32; 33 | Inferio-lateral remainder of parietal lobe |
| | *Central Structures* |
| 34; 35 | Caudate nucleus |
| 36; 37 | Nucleus accumbens |
| 38; 39 | Putamen |
| 40; 41 | Thalamus |
| 42; 43 | Pallidum |
| 44 | Corpus callosum |
| 74; 75 | Substantia nigra |
| | *Ventricles* |
| 45; 46 | Lateral ventricle (excluding temporal horn) |
| 47; 48 | Lateral ventricle, temporal horn |
| 49 | Third ventricle |

# References


[1] A. M. J. Paans, "Positron emission tomography."

[2] A. Bertoldo, G. Rizzo, and M. Veronese, "Deriving physiological information from pet images: From suv to compartmental modelling," 2014.

[3] E. Carson and C. Cobelli, "Modelling methodology for physiology and medicine," 2014.

[4] D. E. Kuhl, E. J. Metter, W. H. Riege, and M. E. Phelps, "Effects of human aging on patterns of local cerebral glucose utilization determined by the [$^{18}$f] fluorodeoxyglucose method," 1982.

[5] S. Sokoloff, M. Reivich, C. Kennedy, M. H. D. Rosiers, C. S. Patlak, K. D. Pettigrew, O. Sakurada, and M. Shinohara, "The [$^{14}$c]deoxyglucose method for the measurement of local cerebral glucose utilization: Theory, procedure, and normal values in the conscious and anesthetized albino rat!," *Journal of Neurochemistry*, vol. 28, pp. 897–916, 1977.

[6] E. Rapisarda, L. Presotto, E. D. Bernardi, M. C. Gilardi, and V. Bettinardi, "Optimized bayes variational regularization prior for 3d pet images.," *Computerized medical imaging and graphics : the official journal of the Computerized Medical Imaging Society*, vol. 38, pp. 445–57, 9 2014.

[7] Y. Xia, J. Wang, S. Eberl, M. Fulham, and D. D. Feng, "Brain tissue segmentation in pet-ct images using probabilistic atlas and variational bayes inference.," *Annual International Conference of the IEEE Engineering in Medicine and Biology Society. IEEE Engineering in Medicine and Biology Society. Annual International Conference*, vol. 2011, pp. 7969–72, 2011.

[8] M. Castellaro, G. Rizzo, M. Tonietto, M. Veronese, F. E. Turkheimer, M. A. Chappell, and A. Bertoldo, "A variational bayesian inference method for parametric imaging of pet data.," *NeuroImage*, vol. 150, pp. 136–149, 2017.

[9] H. Attias, "A variational baysian framework for graphical models," in *Advances in Neural Information Processing Systems* (S. Solla, T. Leen, and K. Müller, eds.), vol. 12, MIT Press, 1999.

[10] M. J. Beal, "Variational algorithms for approximate bayesian inference," 2003.

[11] B. Horwitz, "The elusive concept of brain connectivity," *NeuroImage*, vol. 19, pp. 466–470, 2003.

[12] C. J. Price and K. J. Friston, "Degeneracy and cognitive anatomy," 2002.

[13] K. J. Friston, L. Harrison, and W. Penny, "Dynamic causal modelling," *NeuroImage*, vol. 19, pp. 1273–1302, 8 2003.

[14] J. R. Absher and D. F. Benson, "Disconnection syndromes: An overview of geschwind's contributions," *Neurology*, vol. 43, pp. 862–867, 1993.

[15] K. E. Stephan, "On the role of general system theory for functional neuroimaging," 2004.

[16] K. Friston, "Functional integration and inference in the brain," 2002.

[17] W. D. Penny, K. J. Friston, J. T. Ashburner, S. J. Kiebel, and T. E. Nichols, *Statistical Parametric Mapping: The Analysis of Functional Brain Images*. 2007.

[18] E. R. Kandel, J. Schwartz, and T. M. Jessell, *Principi di neuroscienze*. 2nd edition ed., 1994.

[19] O. Sporns, "Brain connectivity," *Scholarpedia*, vol. 2, p. 4695, 2007.

[20] S. Mori, *Introduction to Diffusion Tensor Imaging*. 2007.

[21] Ü. Aydin, J. Vorwerk, P. Küpper, M. Heers, H. Kugel, A. Galka, L. Hamid, J. Wellmer, C. Kellinghaus, S. Rampp, and C. H. Wolters, "Combining eeg and meg for the reconstruction of epileptic activity using a calibrated realistic volume conductor model," *PLoS ONE*, vol. 9, 3 2014.

[22] K. J. Friston, C. D. Frith, P. F. Liddle, and R. S. Frackowiak, "Functional connectivity: The principal-component analysis of large (pet) data sets," *Journal of Cerebral Blood Flow and Metabolism*, vol. 13, pp. 5–14, 1993.

[23] C. Frith, K. J. Friston, C. D. Frith, and R. S. J. Frackowiak, "Time-dependent changes in effective connectivity measured with pet."

[24] S. Ogawa, T. M. Lee, A. R. Kay, and D. W. Tank, "Brain magnetic resonance imaging with contrast dependent on blood oxygenation (cerebral blood flow/brain metabolism/oxygenation)," 1990.

[25] K. A. Macko, C. D. Jarvis, C. Kennedy, M. Miyaoka, M. Shinohara, L. Sokoloff, and M. Mishkin, "Mapping the primate visual system with [2-$^{14}$c]deoxyglucose," 1982.

[26] B. Horwitz, R. Duara, and S. I. Rapoport, "Intercorrelations of glucose metabolic rates between brain regions: Application to healthy males in a state of reduced sensory input."

[27] I. Yakushev, A. Drzezga, and C. Habeck, "Metabolic connectivity: Methods and applications," 12 2017.

[28] D. S. Lee, H. Kang, H. Kim, H. Park, J. S. Oh, J. S. Lee, and M. C. Lee, "Metabolic connectivity by interregional correlation analysis using statistical parametric mapping (spm) and fdg brain pet; methodological development and patterns of metabolic connectivity in adults," *European Journal of Nuclear Medicine and Molecular Imaging*, vol. 35, pp. 1681–1691, 9 2008.

[29] X. di and B. B. Biswal, "Metabolic brain covariant networks as revealed by fdg-pet with reference to resting-state fmri networks," *Brain Connectivity*, vol. 2, pp. 275–283, 10 2012.

[30] S. Huang, J. Li, L. Sun, J. Ye, A. Fleisher, T. Wu, K. Chen, and E. Reiman, "Learning brain connectivity of alzheimer's disease by sparse inverse covariance estimation," *NeuroImage*, vol. 50, pp. 935–949, 4 2010.

[31] Z. Yao, Y. Zhang, L. Lin, Y. Zhou, C. Xu, and T. Jiang, "Abnormal cortical networks in mild cognitive impairment and alzheimer's disease," *PLoS Computational Biology*, vol. 6, 11 2010.

[32] S. M. Smith, K. L. Miller, G. Salimi-Khorshidi, M. Webster, C. F. Beckmann, T. E. Nichols, J. D. Ramsey, and M. W. Woolrich, "Network modelling methods for fmri," *NeuroImage*, vol. 54, pp. 875–891, 1 2011.

[33] H. F. Wehrl, M. Hossain, K. Lankes, C. C. Liu, I. Bezrukov, P. Martirosian, F. Schick, G. Reischl, and B. J. Pichler, "Simultaneous pet-mri reveals brain function in activated and resting state on metabolic, hemodynamic and multiple temporal scales," *Nature Medicine*, vol. 19, pp. 1184–1189, 9 2013.

[34] E. Jonckers, J. van Audekerke, G. de Visscher, A. van der Linden, and M. Verhoye, "Functional connectivity fmri of the rodent brain: Comparison of functional connectivity networks in rat and mouse," *PLoS ONE*, vol. 6, 2011.

[35] S. Passow, K. Specht, T. C. Adamsen, M. Biermann, N. Brekke, A. R. Craven, L. Ersland, R. Grüner, N. Kleven-Madsen, O. H. Kvernenes, T. Schwarzlmüller, R. A. Olesen, and K. Hugdahl, "Default-mode network functional connectivity is closely related to metabolic activity," *Human Brain Mapping*, vol. 36, pp. 2027–2038, 6 2015.

[36] D. G. Tomasi, E. Shokri-Kojori, C. E. Wiers, S. W. Kim, Ş. B. Demiral, E. A. Cabrera, E. Lindgren, G. Miller, G. J. Wang, and N. D. Volkow, "Dynamic brain glucose metabolism identifies anti-correlated cortical-cerebellar networks at rest," *Journal of Cerebral Blood Flow and Metabolism*, vol. 37, pp. 3659–3670, 12 2017.

[37] M. Amend, T. M. Ionescu, X. Di, B. J. Pichler, B. B. Biswal, and H. F. Wehrl, "Functional resting-state brain connectivity is accompanied by dynamic correlations of application-dependent [$^{18}$f]fdg pet-tracer fluctuations," *NeuroImage*, vol. 196, pp. 161–172, 8 2019.

[38] W. K. Schiffer, M. M. Mirrione, A. Biegon, D. L. Alexoff, V. Patel, and S. L. Dewey, "Serial micropet measures of the metabolic reaction to a microdialysis probe implant," *Journal of Neuroscience Methods*, vol. 155, pp. 272–284, 9 2006.

[39] T. M. Ionescu, M. Amend, R. Hafiz, B. B. Biswal, H. F. Wehrl, K. Herfert, and B. J. Pichler, "Elucidating the complementarity of resting-state networks derived from dynamic [18f]fdg and hemodynamic fluctuations using simultaneous small-animal pet/mri," *NeuroImage*, vol. 236, 8 2021.

[40] T. Volpi, E. Silvestri, M. Corbetta, and A. Bertoldo, "Assessing different approaches to estimate single-subject metabolic connectivity from dynamic [{18}f]fluorodeoxyglucose positron emission tomography data," 2021.

[41] S. D. Jamadar, P. G. Ward, S. Li, F. Sforazzini, J. Baran, Z. Chen, and G. F. Egan, "Simultaneous task-based bold-fmri and [18-f] fdg functional pet for measurement of neuronal metabolism in the human visual cortex," *NeuroImage*, vol. 189, pp. 258–266, 4 2019.

[42] A. Hahn, G. Gryglewski, L. Nics, M. Hienert, L. Rischka, C. Vraka, H. Sigurdardottir, T. Vanicek, G. M. James, R. Seiger, A. Kautzky, L. Silberbauer, W. Wadsak, M. Mitterhauser, M. Hacker, S. Kasper, and R. Lanzenberger, "Quantification of task-specific glucose metabolism with constant infusion of ¡sup¿18¡/sup¿ f-fdg," *Journal of Nuclear Medicine*, vol. 57, pp. 1933–1940, 12 2016.

[43] S. Li, S. D. Jamadar, P. G. Ward, M. Premaratne, G. F. Egan, and Z. Chen, "Analysis of continuous infusion functional pet (fpet) in the human brain," *NeuroImage*, vol. 213, p. 116720, 2020.

[44] N. J. Tustison, B. B. Avants, P. A. Cook, Y. Zheng, A. Egan, P. A. Yushkevich, and J. C. Gee, "N4itk: Improved n3 bias correction," *IEEE Transactions on Medical Imaging*, vol. 29, no. 6, pp. 1310–1320, 2010.

[45] P. Kalavathi and V. B. Prasath, "Methods on skull stripping of mri head scan images: a review," 6 2016.

[46] "https://www.fil.ion.ucl.ac.uk/spm/."

[47] I. S. J. Matthew Brett and A. M. Owen, "The problem of functional localization in the human brain," vol. 3, 2002.

[48] A. Hammers, R. Allom, M. J. Koepp, S. L. Free, R. Myers, L. Lemieux, T. N. Mitchell, D. J. Brooks, and J. S. Duncan, "Three-dimensional maximum probability atlas of the human brain, with particular reference to the temporal lobe," *Human Brain Mapping*, vol. 19, pp. 224–247, 2003.

[49] "https://www.pmod.com/web/."

[50] A. Schaefer, R. Kong, E. M. Gordon, T. O. Laumann, X.-N. Zuo, A. J. Holmes, S. B. Eickhoff, and B. T. T. Yeo, "Local-global parcellation of the human cerebral cortex from intrinsic functional connectivity mri," *Cerebral Cortex*, vol. 28, pp. 3095–3114, 2018.

[51] B. T. T. Yeo, F. M. Krienen, J. Sepulcre, M. R. Sabuncu, D. Lashkari, M. Hollinshead, J. L. Roffman, J. W. Smoller, L. Zöllei, J. R. Polimeni, B. Fischl, H. Liu, and R. L. Buckner, "The organization of the human cerebral cortex estimated by intrinsic functional connectivity.," *Journal of neurophysiology*, vol. 106, pp. 1125–65, 9 2011.

[52] T. Jerman, F. Pernuš, B. Likar, and Ž. Špiclin, "Enhancement of vascular structures in 3d and 2d angiographic images," *IEEE Transactions on Medical Imaging*, vol. 35, no. 9, pp. 2107–2118, 2016.

[53] D. Peruzzo, A. Bertoldo, F. Zanderigo, and C. Cobelli, "Automatic selection of arterial input function on dynamic contrast-enhanced mr images," *Computer Methods and Programs in Biomedicine*, vol. 104, no. 3, pp. e148–e157, 2011.

[54] M. Tonietto, G. Rizzo, M. Veronese, and A. Bertoldo, "Modelling arterial input functions in positron emission tomography dynamic studies," in *2015 37th Annual International Conference of the IEEE Engineering in Medicine and Biology Society (EMBC)*, pp. 2247–2250, 2015.

[55] K. Chen, D. Bandy, E. Reiman, S.-C. Huang, M. Lawson, D. Feng, L. sheng Yun, and A. Palant, "Noninvasive quantification of the cerebral metabolic rate for glucose using positron emission tomography, 18f-fluoro-2-deoxyglucose, the patlak method, and an image-derived input function," *Journal of Cerebral Blood Flow & Metabolism*, vol. 18, no. 7, pp. 716–723, 1998. PMID: 9663501.

[56] M. Rubinov and O. Sporns, "Weight-conserving characterization of complex functional brain networks," *NeuroImage*, vol. 56, no. 4, pp. 2068–2079, 2011.

[57] M. Rubinov and O. Sporns, "Complex network measures of brain connectivity: uses and interpretations.," *NeuroImage*, vol. 52, pp. 1059–69, 9 2010.

[58] M. Veronese, L. Moro, M. Arcolin, O. Dipasquale, G. Rizzo, P. Expert, W. Khan, P. M. Fisher, C. Svarer, A. Bertoldo, O. Howes, and F. E. Turkheimer, "Covariance statistics and network analysis of brain pet imaging studies," *Scientific Reports*, vol. 9, p. 2496, 12 2019.

[59] J. Y. Hansen, G. Shafiei, R. D. Markello, K. Smart, S. M. L. Cox, Y. Wu, J.-D. Gallezot, É. Aumont, S. Servaes, S. G. Scala, J. M. DuBois, G. Wainstein, G. Bezgin, T. Funck, T. W. Schmitz, R. N. Spreng, J.-P. Soucy, S. Baillet, S. Guimond, J. Hietala, M.-A. Bédard, M. Leyton, E. Kobayashi, P. Rosa-Neto, N. Palomero-Gallagher, J. M. Shine, R. E. Carson, L. Tuominen, A. Dagher, and B. Misic, "Mapping neurotransmitter systems to the structural and functional organization of the human neocortex," *bioRxiv*, 2021.

[60] S. Bishu, K. C. Schmidt, T. Burlin, M. Channing, S. Conant, T. Huang, Z. hua Liu, M. Qin, A. Unterman, Z. Xia, A. Zametkin, P. Herscovitch, and C. B. Smith, "Regional rates of cerebral protein synthesis measured with l-[1-11c]leucine and pet in conscious, young adult men: Normal values, variability, and reproducibility," *Journal of Cerebral Blood Flow & Metabolism*, vol. 28, no. 8, pp. 1502–1513, 2008. PMID: 18493259.

[61] A. Hyvärinen and E. Oja, "Independent component analysis: algorithms and applications," *Neural Networks*, vol. 13, no. 4, pp. 411–430, 2000.

[62] V. D. Calhoun, T. Adali, G. D. Pearlson, and J. J. Pekar, "Spatial and temporal independent component analysis of functional mri data containing a pair of task-related waveforms.," *Human brain mapping*, vol. 13, pp. 43–53, 5 2001.

[63] J. Himberg, A. Hyvärinen, and F. Esposito, "Validating the independent components of neuroimaging time series via clustering and visualization," *NeuroImage*, vol. 22, no. 3, pp. 1214–1222, 2004.

[64] F. H. Duffy, G. B. Mcanulty, and M. S. Albert, "Effects of age upon interhemispheric eeg coherence in normal adults," *Neurobiology of Aging*, vol. 17, pp. 587–599, 7 1996.

[65] R. Salvador, J. Suckling, M. R. Coleman, J. D. Pickard, D. Menon, and E. Bullmore, "Neurophysiological architecture of functional magnetic resonance images of human brain," *Cerebral Cortex*, vol. 15, pp. 1332–2342, 9 2005.

[66] E. H. Simpson, "The interpretation of interaction in contingency tables," *Journal of the Royal Statistical Society: Series B (Methodological)*, vol. 13, pp. 238–241, 7 1951.

[67] R. A. Kievit, W. E. Frankenhuis, L. J. Waldorp, and D. Borsboom, "Simpson's paradox in psychological science: a practical guide," *Frontiers in Psychology*, vol. 4, 2013.

[68] W. Robinson, "Ecological correlations and the behavior of individuals*," *International Journal of Epidemiology*, vol. 38, pp. 337–341, 4 2009.

[69] A. J. Fisher, J. D. Medaglia, and B. F. Jeronimus, "Lack of group-to-individual generalizability is a threat to human subjects research," *Proceedings of the National Academy of Sciences*, vol. 115, 7 2018.

[70] S. D. Jamadar, P. G. D. Ward, E. X. Liang, E. R. Orchard, Z. Chen, and G. F. Egan, "Metabolic and hemodynamic resting-state connectivity of the human brain: A high-temporal resolution simultaneous bold-fmri and fdg-fpet multimodality study," *Cerebral Cortex*, vol. 31, pp. 2855–2867, 5 2021.

[71] M. P. van den Heuvel and O. Sporns, "Network hubs in the human brain," *Trends in Cognitive Sciences*, vol. 17, no. 12, pp. 683–696, 2013. Special Issue: The Connectome.

[72] M. Yudkoff, Y. Daikhin, I. Nissim, O. Horyn, B. Luhovyy, A. Lazarow, and I. Nissim, "Brain amino acid requirements and toxicity: The example of leucine," *The Journal of Nutrition*, vol. 135, pp. 1531S–1538S, 6 2005.

[73] J. B. Burt, M. Helmer, M. Shinn, A. Anticevic, and J. D. Murray, "Generative modeling of brain maps with spatial autocorrelation," *NeuroImage*, vol. 220, p. 117038, 2020.

[74] D. G. Tomasi, C. E. Wiers, E. Shokri-Kojori, A. Zehra, V. Ramirez, C. Freeman, J. Burns, C. K. Liu, P. Manza, S. W. Kim, G. J. Wang, and N. D. Volkow, "Association between reduced brain glucose metabolism and cortical thickness in alcoholics: Evidence of neurotoxicity," *The international journal of neuropsychopharmacology*, vol. 22, pp. 548–559, 9 2019.

[75] J. Tohka, "Partial volume effect modeling for segmentation and tissue classification of brain magnetic resonance images: A review," *World Journal of Radiology*, vol. 6, p. 855, 2014.

[76] X. Feng, A. Deistung, M. G. Dwyer, J. Hagemeier, P. Polak, J. Lebenberg, F. Frouin, R. Zivadinov, J. R. Reichenbach, and F. Schweser, "An improved fsl-first pipeline for subcortical gray matter segmentation to study abnormal brain anatomy using quantitative susceptibility mapping (qsm)," *Magnetic Resonance Imaging*, vol. 39, pp. 110–122, 6 2017.

[77] A. L. Beer, T. Plank, and M. W. Greenlee, "Diffusion tensor imaging shows white matter tracts between human auditory and visual cortex," *Experimental Brain Research*, vol. 213, pp. 299–308, 9 2011.

# Ringraziamenti

Ringrazio la Prof.ssa Alessandra Bertoldo che con la sua disponibilità e il suo sostegno mi ha dato l'opportunità di approfondire un argomento che già molto mi appassionava. La ringrazio per avermi fin da subito coinvolta ed integrata nel team, dandomi la possibilità di partecipare a molteplici iniziative da cui ho potuto apprendere davvero molto.
Grazie per aver sempre creduto nelle mie capacità.

Un ringraziamento speciale al mio correlatore Tommaso Volpi che ha avuto un ruolo fondamentale in questo lavoro: mi ha accompagnata passo a passo nel percorso, insegnandomi e chiarendomi dubbi ed incertezze ogni qualvolta ne ho avuto bisogno. Grazie per gli utili consigli, le conoscenze trasmesse e per avermi sempre incoraggiata facendomi sentire fiera ed orgogliosa di questo progetto.

Ringrazio la mia famiglia, pilastro della mia vita. Grazie perché in questi 5 anni mi avete supportato e sopportato, grazie per il vostro continuo amore e sostegno. Grazie mamma per essere sempre il mio punto di riferimento, per essere stata presente in ogni momento di difficoltà, consigliandomi in tutte le scelte più difficili. Grazie per avermi asciugato le lacrime nei momenti bui, per aver ascoltato sempre tutte le mie paranoie e per avermi insegnato ad affrontare la vita a testa alta, spronandomi a dare sempre il meglio. Grazie papà per aver sempre creduto potessi farcela in tutto, per tutte le parole di sostegno e di incoraggiamento che mi hanno accompagnato prima di ogni esame. Grazie per avermi insegnato ad inseguire i miei sogni e a lottare per raggiungerli, con grinta e tenacia. A volte vorrei avere anche solo metà della tua forza. Grazie a mio fratello Andrea, che ogni giorno con la sua serenità e tranquillità mi insegna a dare il giusto peso alle cose. Grazie per il continuo appoggio e affetto, grazie per essere la spalla su cui so potrò contare sempre. Grazie perché senza di voi non sarei mai

arrivata fino in fondo a questo difficile, lungo e tortuoso cammino. Questa tesi la dedico a voi che siete la mia famiglia, il mio più grande sostegno e la mia guida.

Grazie ai miei compagni di viaggio Anna e Davide, per aver condiviso con me le ansie e le difficoltà di questo percorso, ma anche le soddisfazioni che questo ci ha portato. Grazie per essere state le migliori persone che potessi incontrare, grazie per il supporto e l'aiuto reciproco che sempre ci ha caratterizzato. Rimarrà dentro di me la consapevolezza di aver avuto la fortuna rara di trovare degli amici veri in questi anni a volte bui, a volte meravigliosi. Vi ringrazio per essere stati al mio fianco sempre, senza di voi non sarebbe stato lo stesso.

Grazie ad Elena, Maria, Annachiara, Chiara, Riccardo, Valerio, Nicola, Valentina, Alessia ed Alice, gli amici di sempre. Grazie per tutti i momenti di spensieratezza, per l'appoggio che so poter sempre trovare in voi, per gli sfoghi e i consigli sempre preziosi. Grazie per essere stati complici e partecipi, ognuno a suo modo, in questo percorso. Siete il mio porto sicuro, non potrei essere più grata alla vita di avervi al mio fianco.

Grazie a Veronica, Sofia, Gaia, Eleonora ed Alessia che negli ultimi anni avete condiviso con me tanto. Grazie a Veronica per avermi ascoltato, capito e appoggiato in ogni momento, condividendo con me ansie e paranoie, ma anche la sincerità dei momenti felici che fin da subito hanno caratterizzato la nostra amicizia, sei stata essenziale. Grazie a Sofia per avermi insegnato ogni giorno ad essere forte e a rialzarmi dopo le difficoltà, grazie per essere un'amica sempre sincera e presente, grazie per essere stata "casa". Grazie a Gaia per le nostre chiacchierate, l'appoggio reciproco e la complicità che ci caratterizza, la spensieratezza dei nostri momenti è unica. Grazie ad Alessia ed Eleonora, per essere sempre state così premurose e capaci di ascoltare, siete anime belle.

Grazie a Marco, per avermi supportata, appoggiata, ascoltata e aiutata in questi mesi. Grazie perché un po' alla volta mi stai insegnando ad avere fiducia e consapevolezza delle mie capacità, ad avere la pazienza e la determinazione di raggiungere i miei obiettivi, dando sempre il meglio. Mi stai trasmettendo la serenità che spesso a volte mi manca e di questo te ne sono veramente grata.

Per finire, dedico questa tesi anche a me stessa. La dedico ai sacrifici che pen-

savo di non essere in grado di sostenere, alla tenacia e all'impegno che mi hanno permesso di giungere al termine di questo traguardo così importante. Sono stati tanti i momenti di sconforto, ma oggi più che mai sono grata di non aver mai mollato.

Grazie.